



**THÈSE DE DOCTORAT**  
**DE L'UNIVERSITÉ PSL**

Préparée à Chimie ParisTech

Dans le cadre d'une cotutelle avec Università degli Studi di Trento

**Protocole combiné DFT/MD pour la simulation des  
matériaux moléculaires pour le photovoltaïque organique**

**Combined MD/DFT protocol for the simulation of molecular  
materials for organic solar cells**

Soutenue par

**Michele TURELLI**

Le 05 mars 2021

École doctorale n°388

**Chimie physique et chimie  
analytique de Paris centre**

Spécialité

**Chimie physique**

Composition du jury :

**Dorothee BERTHOMIEU**

Directeur de recherche,  
École Nationale Supérieure de Chimie de Montpellier

*Président*

**Carlo ADAMO**

Professeur,  
École Nationale Supérieure de Chimie de Paris

*Directeur de thèse*

**Gianluca LATTANZI**

Professeur,  
Université de Trente

*Co-directeur de thèse*

**Guido RAOS**

Professeur,  
École Polytechnique de Milan

*Rapporteur*

**Juan-Carlos SANCHO-GARCÍA**

Professeur,  
Université de Alicante

*Rapporteur*

**Matteo CALANDRA BUONAURA**

Professeur,  
Université de Trente

*Examineur*



Chimie Paris

ParisTech



# Contents

<b>1 Organic Photovoltaics</b>	<b>8</b>
1.1 The photovoltaic process . . . . .	8
1.2 Heterojunction design . . . . .	13
1.3 Macroscopic observables and photovoltaic performance . . . . .	15
1.4 The MIM model for organic solar cells . . . . .	18
1.5 The current scenario of photovoltaic materials . . . . .	21
<b>2 Methods</b>	<b>29</b>
2.1 Electronic structure methods for organic materials . . . . .	30
2.2 The Born-Oppenheimer approximation . . . . .	31
2.3 Hartree-Fock method . . . . .	32
2.4 Semiempirical methods . . . . .	34
2.5 Density functional theory . . . . .	36
2.6 Functionals and their classification . . . . .	38
2.7 Time dependent extension . . . . .	40
2.8 Modelling organic materials with DFT . . . . .	42
2.9 Beyond molecular scale: supramolecular organisation . . . . .	45
2.9.1 Classical molecular dynamics . . . . .	47
2.9.2 Simulating the amorphous phase . . . . .	48

2.9.3 Simulation of the ordered phase: a combined Monte Carlo and DFT approach	49
2.10 Coupling length scales: charge transport	52
2.10.1 Marcus theory for charge transfer	54
2.10.2 Kinetic Monte Carlo	59
<b>3 The case of a small-molecule donor</b>	<b>64</b>
3.1 A small push-pull molecule	66
3.2 Computational details	67
3.3 Main results	69
3.4 Conclusions	86
<b>4 A donor-acceptor dyad test-case</b>	<b>88</b>
4.1 The DPP-Ful donor-acceptor dyad	90
4.2 Computational details	91
4.3 Main results	94
4.3.1 Isolated molecules and crystalline polymorphs	95
4.3.2 Amorphous phase	109
4.4 Conclusions	111
<b>5 Conclusions</b>	<b>113</b>



# Introduction

A large part of the literature on organic photovoltaics frames the topic within the current energy crisis and offers this branch of materials science as an example of the effort scientists are making to answer this urgent societal need.

However, it is possible to look at it from a larger and more informative perspective offered by the field of functional materials. Like many other domains, materials science has immensely benefitted from the increased availability of computational resources. These new means have revolutionised the way research is carried out and notably, they have pushed forward the development of theoretical methods, once relegated to the study of rather simple systems with limited practical applications.

These new conditions have prompted a shift in the paradigm from an empirical approach based on an informed trial-and-error methodology to a situation in which a coherent theoretical framework, guiding the interpretation of results, supports the experimental endeavour.

This process has also been encouraged by the continuous refinement of experimental techniques and the development of more sophisticated instruments whose working principles are based on growingly complex physical phenomena. Data generated thanks to these new techniques require a solid knowledge of the underlying phenomenon for them to be correctly extracted and interpreted. In addition, as these experimental data become finer in the time and length resolutions probed, theoretical modelling is required to provide predictions with comparably high resolution. This exchange results in a cycle where experiments become more complex thanks to the aid of theoretical modelling while the theoretical framework expands and fills the remaining gaps.

After a few iterations, this process reaches a point in which modelling is sufficiently advanced to not only support but also direct the experimental search.

This is of particular importance in the field of functional materials. Here, the complexity and diversity of systems under investigation is such that the deployment of theoretical modelling is not only convenient but becomes necessary.

To corroborate this point, a few attempts can be cited that have been made to assess the currently accessible chemical space of organic compounds, that is estimated to be in the range of  $10^{20} - 10^{24}$  molecules<sup>[1][2][3]</sup>. Exploring this enormous landscape is extremely difficult and ineffective when empirical intuition and experimental characterisation are the only probe.

The apparent necessity of theoretical approaches capable of mapping the chemical space, according to the most relevant properties<sup>[4]</sup>, makes their development one of the most important goals in modern day materials science. These approaches also foresee the possibility of a purpose-driven design<sup>[5]</sup> of functional materials to answer very specific technological demands.

The main obstacles to this prospect can be traced back to the considerable gap between the time and length scales theoretical methods are able to explore and the typical scale of technological applications. This difference reflects the scale separation of the fundamental building blocks, atoms and molecules, with the human scale and it is necessary for complexity to emerge.

It is therefore mandatory to combine various levels of theory describing different time and length domains to deal with this scale gap. This combination is justified by the difference in scales at which the many degrees of freedom in a macroscopic system experience their dynamics. Fast degrees of freedom produce an average effect on slower processes and may be effectively treated as parameters in the description of these last. Thus, a combination of various methods may indeed provide a reliable modelling of real systems.

This thesis work is set in this context. It deals with the development and the application of a computational protocol, combining different established levels of theory, able to offer a direct atomistic picture of the small scales responsible for the functional behaviour. The focus is on the class of organic materials exploited to harvest solar energy, collectively referred to as organic photovoltaics<sup>[6][7][8]</sup>.

This work is by no means a first but joins the ranks of an important body of research<sup>[9][10][11][12]</sup> on which it builds. It deals with the complex task of bridging the gap between the accurate

modelling capabilities available at molecular scale and the efficient simulation of macroscopic devices. This complexity makes it so that any given protocol will focus on some particular aspects and will inevitably overlook others. The hope is that, in the future, a new generation of such protocols will enable scientists to explore more efficiently the chemical space and to identify energy harvesting materials with enhanced performances.

The specific focus of the protocol presented is on the atomistic mechanisms underlying the behaviour of photovoltaic systems. The microscopic picture that the protocol aims to provide has two main objectives. First, to foster a deeper understanding of the theory behind and second, to offer a microscopic view of the consequences certain synthetic choices have on important properties like supramolecular ordering<sup>4</sup>.

What is beyond the goals of this protocol is instead the description of the processes taking place at scales much larger than the molecular one. A realm where other emergent mechanisms play a significant role in photovoltaic performance<sup>13</sup>. The description of this range of scales will only be attempted through some extrapolations that will be revealed nonetheless, to be effective in producing numerical predictions in agreement with available experimental data.

In keeping with these premises, this text will be structured as follows. A first chapter will introduce in further detail the scientific background and the open issues in photovoltaic research motivating the need of computational protocols. Ample space will be devoted to the specific properties and functions that photovoltaics materials are required to have. A brief overview of the current picture will be offered, together with a description of the specific challenges that have come up in the quest for materials with enhanced performances.

The second chapter will present the theoretical foundations to the various computational approaches that constitute the protocol. This presentation will offer the main ideas on which the methods are based by giving a concise but self-contained explanation.

Two applications of the protocol to relevant systems will be presented in chapter three and four. The systems investigated were selected on the basis of experimental data indicating that a microscopic picture was missing and its modelling would offer relevant insight that could be extended to similar materials.

Both systems belong to trending research domains within the larger field of organic photo-

voltaics. In particular, in chapter three the protocol will be applied to the study of a small-molecule donor showing important changes in the absorption spectra linked to the material's local morphology. While chapter four will instead be devoted to the study of a molecular donor-acceptor dyad. In this case, empirical data hint at the emergence of long-range ordering within the studied devices and the application of the protocol will be shown to yield a plausible atomistic picture for the ordered structure likely responsible for the reported efficiency.

# Chapter 1

## Organic Photovoltaics

The designation of “functional materials” has risen in opposition to “structural materials”<sup>[14]</sup> to indicate materials that are used to perform a specific function going beyond mechanical support. This distinction has come into being as the progressively accumulated knowledge in chemistry and solid-state physics has been able to inspire uses based on properties associated with electrical, optical, magnetic or chemical responses.

The materials studied in the field of organic photovoltaics naturally belong to this category. Their particular behaviour stems from their semiconductor character. A semiconductor is a material that can either act as an insulator or a conductor depending on the external conditions determined by the environment. Radiation from a light source is one of the possible external stimuli that are able to trigger the conducting behaviour. This fact can be exploited within a device with a specific architecture to convert the power absorbed from radiation to electrical power.

In order to better understand how photovoltaic materials express this behaviour and how they can be exploited in the harvesting of solar energy, it is useful to look in more detail at the general mechanism underpinning the photovoltaic process, as it is understood.

### 1.1 The photovoltaic process

The prototypical solar device can be described as a layer of a photoactive semiconductor, sandwiched between two electrodes (i.e. metal contacts). A general scheme of the photo-

voltaic conversion for this device can be given as follows. The photoactive layer, irradiated by light, absorbs the incoming photons and electronic excited states are produced called “excitons”. These excitons then can either undergo dissociation into free charges or decay via radiative or non-radiative pathways, i.e. via the emission of a photon or via other channels. If conditions within the layer are right, the exciton is dissociated into an electron and a hole, called a “geminate pair” that are free but still feel a reciprocal attraction. These charge carriers then experience a general drift-diffusion dynamics and, if they do not recombine, are collected at the electrodes to produce a current that is called photocurrent.

According to the type of semiconductor, i.e. inorganic or organic, this general process takes on different nuances that result in the vastly different performances recorded for solar devices.

An aspect that all semiconductors share is the presence of extended structures where electrons are delocalised. Delocalisation is a fundamental ingredient to semiconducting behaviour. In silicon, probably the most renowned inorganic semiconductor, electrons are able to delocalise over the lattice produced by the assembly of large numbers of silicon atoms. In this case, delocalisation can be rather extended in space. The interaction between isolated atoms in the lattice results in a new energy level structure, in which these levels proliferate and participate to the formation of so-called “energy bands”. These bands represent the allowed electronic energies within a material.

The band structure is defined by an alternating sequence of allowed energy ranges with forbidden ones, called gaps. In the ground state of the lattice, all valence electrons occupy a band called valence band. Interaction with photons promotes the electrons from an energy level to another. This promotion can happen between a pair of occupied and unoccupied energy levels in the same band or between different bands separated by a gap.

The first band above the valence one is called conduction band and the forbidden gap between these, the band gap, its value is often indicated as  $E_g$ . This last is of paramount importance for the photovoltaic behaviour. Depending on the value of  $E_g$  in fact, materials show different responses to external stimuli such as light and can be consequently classified into insulators, conductors or semiconductors.

A similar picture holds for the band structure of organic semiconductors but with some im-

portant differences. In this kind of materials the large number of aggregated molecules retain, more or less, their isolated geometry and interact with each other via weak Van der Waals forces. The band diagram resulting from this assembly is more structured and fragmented. In this case, valence and conduction bands are rather narrow and centred<sup>[15]</sup> around the energy of the highest occupied molecular orbital (HOMO) and lowest unoccupied molecular orbital (LUMO) of the compound. Delocalisation in this case is ensured by the presence, on the molecular architecture, of  $\pi$ -conjugation. This peculiar orbital arrangement is realised when *p*-type orbitals, not participating in the main bonds between a planar structure of carbon atoms, combine to form a diffuse electronic orbital extended over the approximately planar structure.

Typically, organic  $\pi$ -conjugated structures are much less extended in space than inorganic lattices. Upon absorption, this less pronounced delocalisation results in an excited electron with a rather local character. In this picture, one can say that only a single molecule is excited into a higher energy state. In contrast, for an ideal extended lattice, the entire structure can be thought to be excited when a photon is absorbed. This difference holds for most organic materials with mounting experimental evidence suggesting that a different behaviour emerges in a few systems belonging to well-known molecular families<sup>[16]</sup> that is associated to good photovoltaic performances.

The excited electron is bound more tightly to the molecular structure than in the case of an inorganic lattice and this is due to the weaker intermolecular interactions. This results in solids with a rather small relative dielectric constant  $\epsilon_r \sim 2 - 4$ <sup>[17][18][19]</sup> in which the excited electron “feels” a strong attraction to the positive hole it has left behind upon excitation. This simple fact has extreme consequences on the performances of organic semiconductors in solar cells. The generation of strongly bound excitons means that it is more difficult to separate them and to extract free charges.

To give an idea of the scales, typical binding energies in inorganic materials are in the range of a few meV while organic materials show binding energies a hundred times larger at the very least, and often much higher. Empirical evidence suggests energies ranging from 0.1 to 1.4 eV<sup>[20]</sup>. If one considers the typical energy of thermal fluctuations at ambient temperature (300 K),  $k_B T = 26$  meV, it is rather straightforward to see that inorganic excitons will readily split into free carriers thanks to thermal agitation, while organic ones will be more difficult

to dissociate.

Historically, this is the reason for which research into organic photovoltaics initially stalled<sup>[21]</sup>, after several attempts revealed that the photocurrent typically generated by organic photoactive layers were far below any useful value.

A way to circumvent this problem has been presented by Tang *et al.* in 1986<sup>[22]</sup>. The device described in this seminal work was able to achieve reasonable efficiency thanks to the combination, or *junction*, of two organic materials. The increased intensity of the photocurrent is due to the formation of an interface between the two materials that promotes the splitting of the exciton.

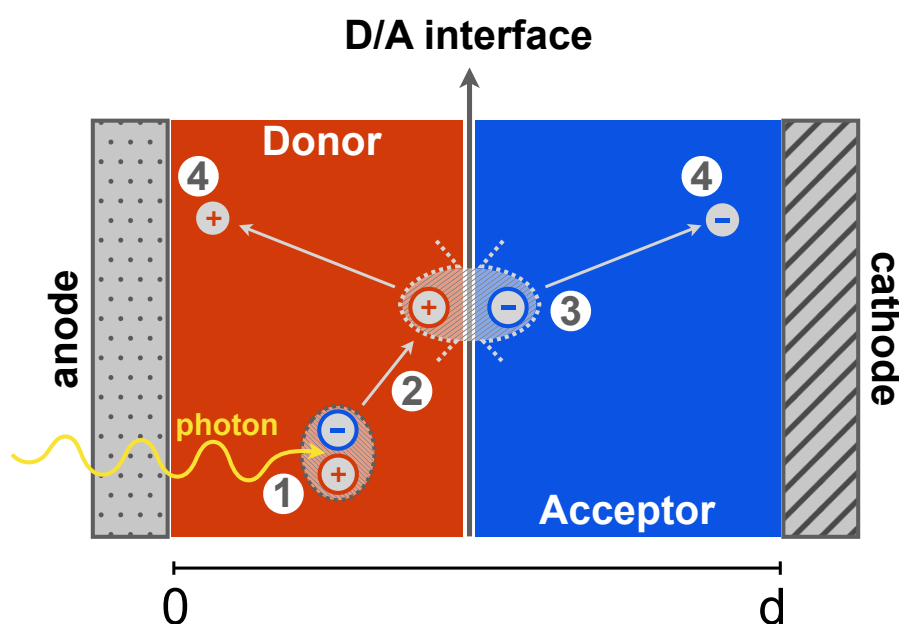


Figure 1.1: Illustration depicting all the 4 steps in which the photovoltaic process may be divided. (1) photon absorption and exciton generation, (2) exciton diffusion and encounter with the interface (3) exciton dissociation (4) charge collection at the electrodes.

To realise this junction, the two semiconductors must have different electron affinities  $EA$ , i.e. LUMO levels. The material with the higher  $EA$  will eagerly accept an electron from the other material, for this reason they are called *acceptor* and *donor* and are the organic equivalent of a  $p$ -doped or  $n$ -doped semiconductor.

Despite not being the first historical example of a junction, Tang device was the first showing a power output large enough to justify further research and it is therefore considered a fundamental milestone in the field.

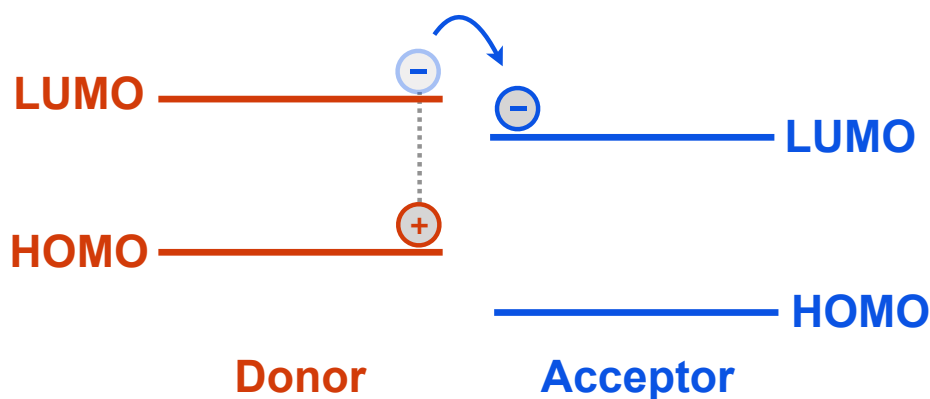


Figure 1.2: Matching of the energy level at the donor acceptor interface that ensure the dissociation of the exciton into free charges. This is valid for both planar and bulk heterojunction. Any neighbouring pair of a donor and an acceptor may perform the exchange according to this scheme.

At the interface, the bound exciton finds the conditions to be separated into free carriers. These conditions correspond to a specific arrangement of the energy levels of the two materials. If an exciton is generated within the donor, it will be promoted from the narrow band of the HOMO to the LUMO band. If it diffuses in the proximity of the interface, a series of rather complex transitions take place between states that are progressively more delocalised. These transitions are able to lower the Coulomb interaction between hole and electron and promote dissociation. The process is favourable from an energetic point of view if the difference between the HOMO level of the first material,  $E_{\text{donor}}^{\text{HOMO}}$ , and the LUMO of the second material,  $E_{\text{acceptor}}^{\text{LUMO}}$ , is lower than the exciton binding energy, as shown in Fig. 1.2. If this condition is verified then the exchanging pair will find a favourable state in which a finally free electron occupies the  $\text{LUMO}_{\text{acceptor}}$  while the free hole occupies the  $\text{HOMO}_{\text{donor}}$ .

Further on more details about the junction of two or more materials are given, as they are essential to understand the current status and the main challenges in the field.

After dissociation, the dynamics of the free charges is governed by the electric field within the material. The potential gradient responsible for this field may have different origins depending on the design. For organic materials, it is usually determined by the choice of the electrodes. Typically, two metals with high (anode) and low (cathode) work function are selected. The work function is the energy required to extract one electron from the metallic solid. High work-function metals have electrons in low-lying energy levels while low work-function metals have electrons in shallower levels and less energy is required to extract them

with respect to the former. By sandwiching the semiconductor between them, the tendency of the system to equilibrate the work functions will generate an in-built field.

This arrangement can be described as a metal-insulator-metal (MIM) junction and will be discussed in more detail in the next section.

The efficiency of charge collection, associated with carrier dynamics, can be measured through charge mobility, a quantity that describes how much a material promotes or hampers the movement of charges.

Often, organic semiconductors report low mobilities for both carriers compared to their inorganic counterparts, e.g. for amorphous silicon  $\mu_e = 1 \text{ cm}^2/\text{V} \cdot \text{s}$ <sup>[23]</sup>, or other materials such as perovskites, e.g.  $\mu_e = 25 \text{ cm}^2/\text{V} \cdot \text{s}$ <sup>[15]</sup>.

In addition, transport of holes and electrons is often unbalanced. In many instances in fact, electrons are transported more effectively than holes and this results in an accumulation of electrons at the cathode that affects the potential within the photoactive layer and leads to a saturation of the photocurrent below the theoretical limit.

The extraction of carriers from the active layer to produce the photocurrent, marks the final step of the charge collection process. Similarly to dissociation, this process relies on the matching between the energy levels of the material and that of the electrodes. The most straightforward matching to adopt is the condition of *ohmic contacts* where the work function of the anode is approximately matched with the donor HOMO, while the cathode work function is matched with the acceptor LUMO.

These steps, summarised in the scheme of Fig. 1.1, constitute the general microscopic description of photovoltaic conversion. Each step naturally participates to the overall efficiency of the whole process and high-performance solar devices should be able to find the optimum between all of them. This optimisation can be promoted by choosing particular designs of the organic active layer that will be presented in the next section.

## 1.2 Heterojunction design

The current landscape of solar technologies based on organic semiconductors cannot be fully appreciated without reviewing the main designs that have been proposed for the mixing of

donor and acceptor materials. As seen before, the mixing is necessary to achieve a sufficient generation of free carriers by enhancing exciton dissociation.

The most simple design that can be proposed is the **bilayer planar heterojunction**, already present in Tang *et al.*<sup>[22]</sup>. As the name suggests, in this basic implementation the active material is composed of two superimposed layers of donor and acceptor and the interface is created in the planar region where the two layers meet, as shown in Fig. 1.3, left.

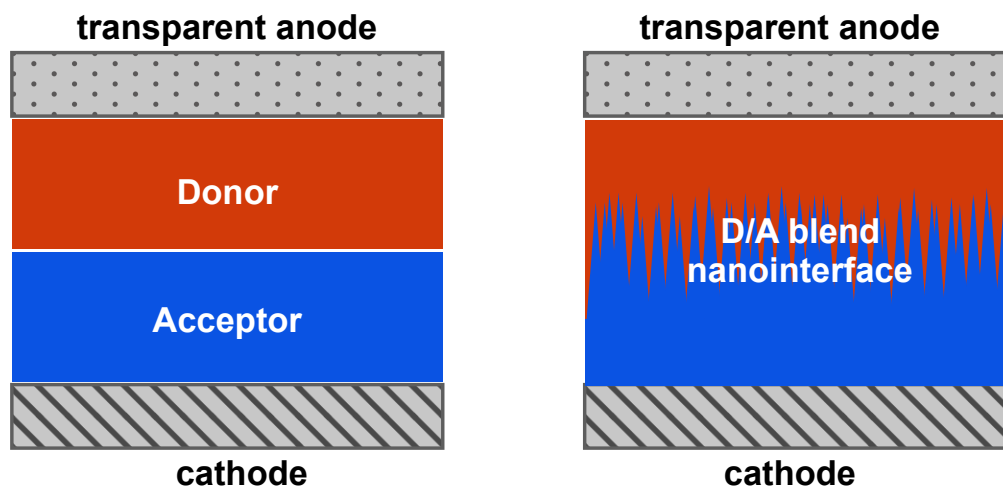


Figure 1.3: Representations of the most common heterojunction devices for donor and acceptor blends. The planar heterojunction (*left*) with layers stacked one upon the other and an ideally planar interface. The bulk heterojunction (*right*) with a structured interface diffuse over the whole volume of the layer.

While the introduction of the interface is successful in promoting exciton dissociation, one important limitation emerges. To be efficiently separated the excitons created in the organic layer need to reach the interface. Given their excited character, excitons have a finite lifetime, dependent on the presence of many possible decay pathways. A finite lifetime means that the exciton can be displaced over a limited range from the absorption site. In molecular materials, the value of this distance rarely goes above few tens of nanometers<sup>[24]</sup>. The obvious solution is therefore to reduce the thickness of the layers to ensure that the majority of excitons reach the interface and are split into free carriers.

However, reducing the thickness of the film has an effect on the efficiency of absorption. Despite organic materials having relatively large molar extinction coefficients<sup>[17]</sup>, i.e. they tend to absorb a large number of photons per unit length of thickness, a tension emerges

between the maximum exciton diffusion length and absorption so that a compromise between the two usually results in devices with unsatisfactory performances.

This bilayer design is currently employed in many experimental devices because it is simple to realise and may serve as a preliminary evaluation of the photovoltaic potential of a given acceptor-donor pair.

A further sophistication and an important milestone in the historical development of organic solar cells, is the **bulk heterojunction**<sup>[25][26][27][28]</sup>. In these devices, donor and acceptor are deposited as films in a single blend. Depending on the interaction between the two components and the deposition technique, that might imply for example, the use of solvents, the layer will feature an interface interspersed within the bulk of the active layer, as shown in Fig. 1.3, right.

An interface structured within the volume, means that the limitation on the thickness can be overcome without losing most of the excitons. An ideally optimised donor-acceptor bulk interface ensures that every exciton is generated within the average diffusion length from the interface and may therefore be split into free carriers. Many of the experimental devices that today report the largest efficiencies in converting solar light are based on this kind of heterojunction<sup>[29]</sup>.

The main difficulties in the implementation of this particular design concern the instability of the interface and the limited control that can be exerted over the morphology, that is, at present, rather limited<sup>[30][31][32]</sup>.

A promising strategy to exert a greater control over the dynamics of self-organisation is the direct engineering of the molecular structure of the blended materials. This process corresponds precisely to the exploration of the chemical space around a given compound and may greatly benefit from the application of different theoretical protocols of the same kind as the one presented in this work.

### 1.3 Macroscopic observables and photovoltaic performance

The description of the photovoltaic process given above, focuses on the microscopic picture. Yet, solar devices operate almost at macroscopic scale and their characterisation involves

measurements on the device performed at this scale.

These measured quantities are the result of the statistical behaviour of charge carriers generated and collected throughout the process and are necessary to determine the efficiency with which this process takes place.

Conventionally, solar cells are tested under standardised conditions of temperature, pressure and illumination<sup>[33]</sup>. The spectrum of irradiation is taken to be the Sun spectrum after being filtered by the atmosphere crossed at around 48.2° of zenith angle, air mass 1.5 (AM1.5)<sup>[34]</sup>.

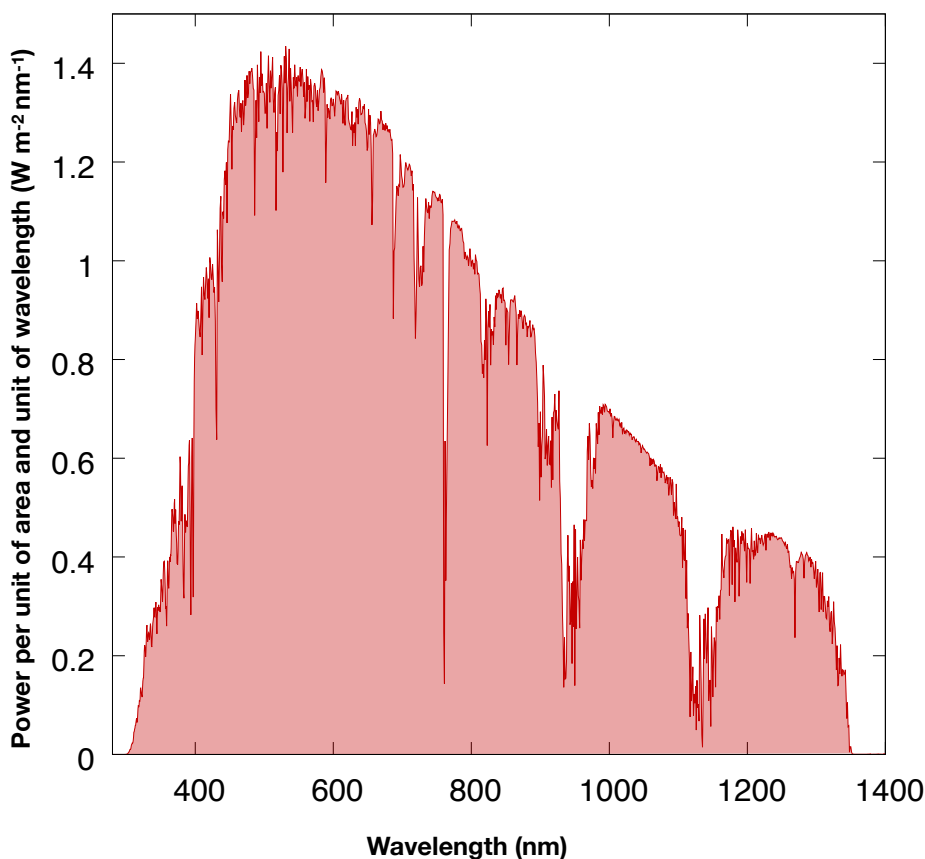


Figure 1.4: Sun spectrum after being filtered by an air mass equivalent to the atmosphere crossed by rays at 48.2° of zenith angle. Conventionally this condition is referred to as “solar spectrum AM 1.5”.

The efficiency of a solar cell is usually expressed through a quantity called “power conversion efficiency”, or *PCE*, that is evaluated by considering the ratio between the output power  $P_{\text{out}}$  with respect to the power of the incoming radiation,  $P_{\text{solar}}$ :

$$PCE_{\%} = \frac{P_{\text{out}}}{P_{\text{solar}}} \cdot 100 \quad (1.1)$$

This efficiency is the product of the efficiencies of all the four steps reviewed before. Microscopic descriptions of the photovoltaic process are able to link this efficiency with the statistical behaviour of carriers in the active layer.

It is possible to define three fundamental quantities, see plot in Fig. 1.5, evaluating the behaviour of the solar cells as an element of a circuit:

- *Short circuit current density*  $J_{sc}$  [ $\text{mA}/\text{cm}^2$ ] defined as the photocurrent generated, under irradiation, when no external voltage is applied at the electrodes, i.e. in an ideal condition where anode and cathode are short circuited. In this situation, the current density results from the extraction of carriers at the electrodes. This quantity directly depends on many molecular quantities like width of band gap, phase separation and the magnitude and relative value of mobility for both carriers.
- *Open circuit voltage*  $V_{oc}$ , is defined as the external voltage at which the current output from the solar device vanishes. In this situation the applied voltage compensates the internal built-in field. A vanishing internal field implies a missing driving force for the carriers generated that will only diffuse in the material and accumulate at the electrodes until an equilibrium is reached with recombination. In the case of ohmic contacts, i.e. the electrodes match the transport levels of the blend, this quantity depends on the energy offset of these levels.
- *Fill factor*  $FF$ , this quantity determines the shape of the relation between applied voltage  $V$  and output current density  $J$ , called  $J$ - $V$  curve<sup>24,35</sup> (see Fig. 1.5). And can be related with the two quantities above as follows

$$FF = \frac{J_{\max} V_{\max}}{J_{sc} V_{oc}} \quad (1.2)$$

where  $J_{\max}$  and  $V_{\max}$  are the output current density and the applied voltage at maximum power output (max). The fill factor encodes a lot of processes at different length scales within the device affecting the overall performance. Its value depends on molecular details as well as on the higher-scale morphology of the active layer. It also provides a measure of how much it is theoretically possible to optimise the cell and enhance its performance.

Empirical models exist that can establish a direct link between these macroscopic circuital quantities and microscopic one like mobility and absorption that may be evaluated through computational methods like the one presented in this work. To clarify the relation between the microscopic picture and these circuital quantities the MIM junction will be presented in more detail in the next section and the different operating regimes will be described.

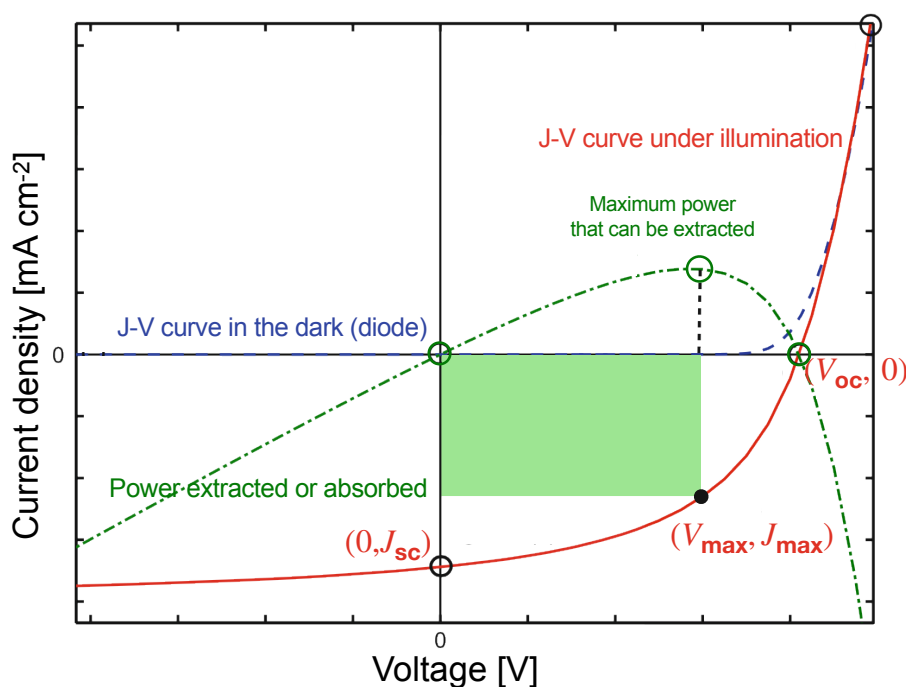


Figure 1.5: Plot of a typical J-V curve, the green rectangle represents the fill factor FF.

## 1.4 The MIM model for organic solar cells

The metal-insulator-metal (MIM) model<sup>[6][24][35]</sup> is often used to describe the operating principle of a cell based on an organic blend. As previously mentioned, the system can be obtained by sandwiching a material between two metal electrodes. In this specific case, the material corresponds to the organic junction of donor and acceptor in planar or bulk design.

The two metal electrodes are chosen to have different work functions  $\phi_W$ . The work function is associated with the energy of the highest level occupied in an electron system at  $T = 0$  K, known as Fermi energy  $E_F$ , the two will be used interchangeably in the following.

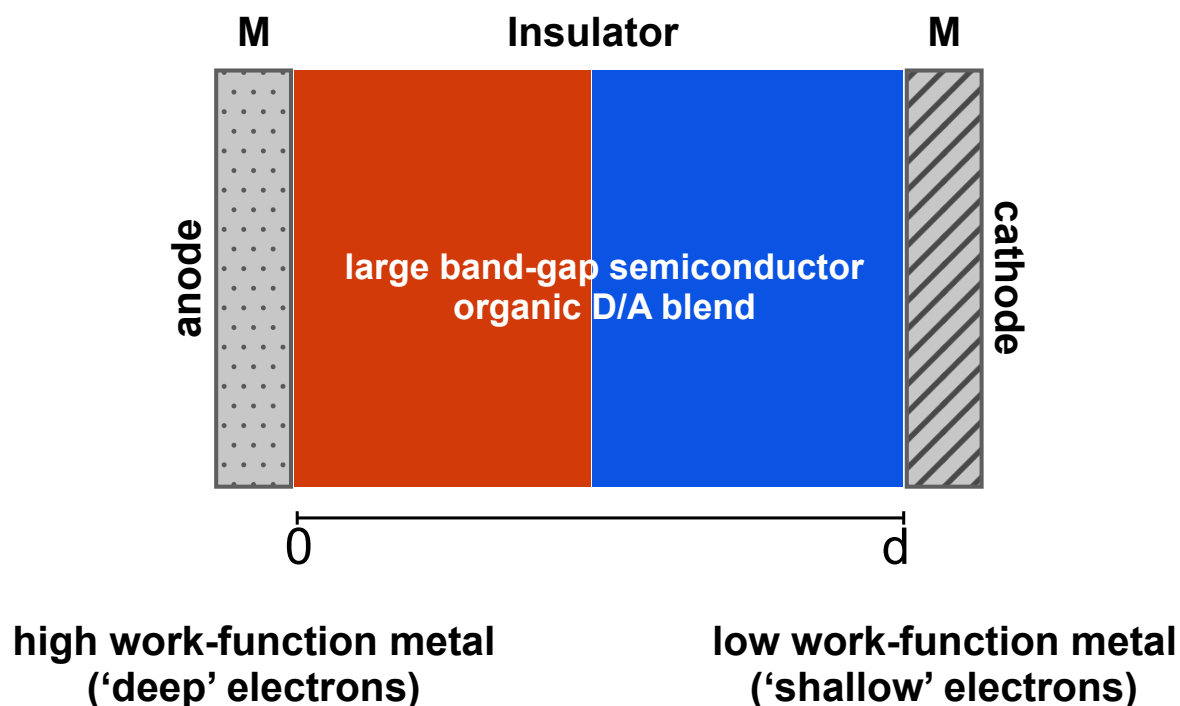


Figure 1.6: Schematic depiction of a MIM junction that best captures the general working principle of an organic solar cell. The left electrode is the anode while the right electrode is the cathode.

To illustrate the functioning of a MIM junction one may consider a system with a high work-function electrode on the left and a low work-function metal on the right, see Fig. 1.6. The two metals are in contact through the organic blend and their work-functions are matched according to ohmic contacts.

The system at equilibrium requires  $E_F$  to be constant throughout the semiconductor layer. This implies the transfer of electrons from the low work-function electrode to the high work-function one, until  $E_F$  is constant. This displacement of charges produces a potential difference inside the material that affects the semiconductor blend. The response of the material is to compensate this potential by redistributing the available free carriers. An excess of positive carriers will be accumulated on the left, close to the high work-function metal, while an excess of electrons will be accumulated on the right.

The final distributions are the result of two competing agents, the potential produced by the electrodes and the tendency of the system to have an homogeneous concentration of carriers within the active layer. It is important to note that the number of available free carriers in a typical organic blend at ambient temperature is very small but those present will respond to

the electric field according to the mechanism described<sup>[17]</sup>.

Starting from this static condition at equilibrium it is useful to consider two external perturbations: irradiation with light and the application of an external bias potential at the electrodes. The latter also includes the case in which the device is used to produce electricity. By inserting a load in fact, a potential difference is applied to the electrodes with the characteristics of a forward bias, i.e. the cathode is at an higher potential than the anode.

Thanks to radiation, the semiconductor blend is able to increase its population of free carriers by generating excitons that are split at the blend interface. The “pumping” performed by radiation allows the system to enter an out-of-equilibrium steady state in which the Fermi energy level of the system splits into two quasi-Fermi levels, one for electrons in the conduction band,  $E_F^e$ , and the other for holes in the valence band,  $E_F^h$ . These correspond to the  $\text{LUMO}_{\text{acceptor}}$  and  $\text{HOMO}_{\text{donor}}$ , respectively. The carriers follow a dynamics similar to the one without illumination and will redistribute according to the internal field caused by the difference in the work-functions  $\Delta\phi_W$ .

When the irradiated system is connected to a circuit and a biasing potential is present, it is possible to distinguish three situations.

When the external bias potential is negative  $V_{\text{bi}} < 0$ , a limited current flows through the circuit due to the fact that there are high injection barriers for electrons on the left (anode) and holes on the right (cathode).

When the biasing potential is positive but less than the open circuit voltage  $V_{\text{oc}}$ ,  $0 < V_{\text{bi}} < V_{\text{oc}}$ ,  $V_{\text{bi}}$  and the built-in one are in competition. Within the irradiated layer, the carriers experience a drift in the direction of the difference between built-in and biasing potential while a diffusion current flows in the opposite direction.

The biasing potential injects holes on the left and electrons on the right, generating a current that is opposite to the direction of the built-in field. However under these conditions, the total photocurrent is still dominated by the built-in field and flows in the opposite direction to the external potential. This current can be exploited to actually extract power from the device.

Finally, when the biasing potential overcomes the built-in field  $V > V_{\text{oc}}$  the sign of the current is reversed and flows in the direction dictated by the external potential. In this condition the MIM device is not generating power anymore and it is simply acting as a photoconductor.

So, the existence of the built-in field and the tension between diffusion and drift currents play a fundamental role in the photovoltaic process and in the emergence of the diode behaviour, i.e. presence of an energetic barrier  $V_{\text{built-in}} = \Delta\phi_{\text{W}}$ .

The model does not explicitly mention the molecular quantities object of this study, except for the molecular orbitals of the blend. However, there is a strong dependence of drift and diffusion currents and carrier distributions on mobility and absorption properties that are crucial to the determination of photovoltaic efficiency.

## 1.5 The current scenario of photovoltaic materials

The sections above should have presented substantial evidence about the many processes concurring to the photovoltaic behaviour. Indeed, the enhancement of PCE is a multidimensional problem implying the co-optimisation of a number of competing properties.

Often, maximising the efficiency of one step may turn out to be detrimental to another. This situation is even more dramatic for organic semiconductors. In this regard, the availability of a large chemical space of possible candidates is good news as it leaves ample room for improvement.

The current status of the field is the result of at least two decades of intense effort that has been able to produce experimental devices with capabilities around the threshold for commercialisation<sup>36</sup>. Much work remains to be done as the transition from experimental to commercial technologies is riddled other difficulties lying outside the scientific domain<sup>37</sup>.

The present picture of the field reveals a series of clear paths that have been laid out to address some of the issues that, if solved, could greatly advance the technology. To fully present this picture it is mandatory to provide a brief overview of the major families of materials that constitute the dominant research currents.

The catalogue of materials that have been studied is incredibly rich. A layered categorisation of this multitude first distinguishes materials based on their usage as acceptors or donors. Among donors, a clear distinction appears between polymers and small molecules while for acceptors the most important classes turn out to be fullerene derivatives with all the others grouped into the broad category of non-fullerene acceptors.

In addition to this categorisation, in recent times, a new class has emerged that escapes the donor/acceptor classification. These materials can be used to overcome the limitations of the bulk heterojunction design and are at the basis of so-called single material organic solar cells (SMOSCs).

This section will present these categories with a focus on the general characteristics that may promote performance enhancement.

## Polymers

Despite not being among the first materials investigated in organic solar devices<sup>[21]</sup>, polymers have soon monopolised the attention of the community. This is due a series of important observations on the excellent conductive properties of doped polyacetylene<sup>[38][39]</sup> and other seminal works reporting fast electron transfer between fullerenes and polymers in organic blends<sup>[40][41]</sup>. These consequential works lead, respectively, to the 2000 Nobel prize in chemistry and to the widespread use of the bulk heterojunction design.

From a theoretical point of view, the conductive behaviour of polymers is not surprising. Many systems in this category present  $\pi$ -conjugated structures whose geometry allows delocalisation over rather extended scales, at least along the backbone.

An archetypical example is polyacetylene (see Fig. 1.7) whose alternating structure of single and double bonds should result in a total delocalisation of outer electrons on the backbone and confer to the material nearly metallic conductivity<sup>[42]</sup>. In reality this situation is not realised because the interactions between molecular vibrations and electrons localise the orbitals that extend over few adjacent monomeric units at most.

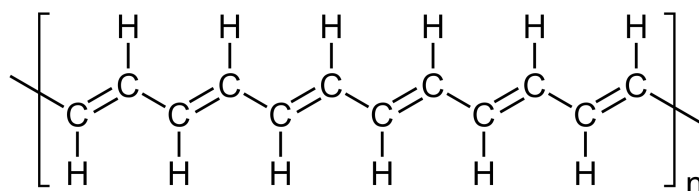


Figure 1.7: Trans polyacetylene monomeric unit with the alternating double-single bond structure in evidence.

More in general, this limit on delocalisation has turned out to be a substantial bottle-neck for

the performance of polymeric materials. Localised electronic orbitals in fact, translate into a low lying HOMO level that requires a large energy to be excited. This produces a sensible widening of the  $E_g$  gap.

Among the implications of a large band gap  $E_g$ , the most important is the reduced absorption of solar photons and thus the reduced value of the maximum photocurrent  $J_{sc}$ . Band gaps for most polymers employed in the literature for photovoltaic conversion are rarely below 1.5 eV<sup>43,44</sup> and very often above 2.0 eV<sup>45</sup>.

Strategies to address the band gap problem in polymers<sup>46</sup> rely heavily on the exploration of the chemical space around the already available compounds via the engineering of the monomeric unit<sup>47</sup>.

In particular, two strategies have given fruitful results throughout the years. The first is based on the synthesis of monomeric units combining electron deficient *A* and electron rich *D* groups in *D-A* architectures. These changes affect the structure of the energy levels and favour transitions at lower energy with higher delocalisation.

The second strategy instead, is aimed at the enhancement of backbone planarity. This is usually attempted by stabilising the quinoid form, generally more planar, over the aromatic one<sup>46</sup>. More planar structures have more delocalised orbitals and reduced band gaps<sup>48</sup>.

These approaches are limited by the implications that the changes in polymer properties like molar mass, regioregularity and polydispersion have on the self-organisation of the material whose higher scale morphology may be affected in ways that are detrimental to the over-all performance.

Another important issue that polymers face is the reproducibility of performances. Power conversion efficiencies for devices employing the same blend and a similar architecture may be quite different due to the limited control over purity or polydispersion and other variables associated with the preparation of the blends.

Reproducibility is clearly essential when many mechanisms responsible for the final performance are still partially understood. For this reason, part of the community has shifted its focus on the study of small-molecule donor in an effort to create a line of research better suited to support the theoretical effort in expanding the current understanding.

## Small-molecule donors

Small-molecular donors have gained momentum since the mid 2000's<sup>49,50,51</sup>. They have been the object of increasing attention because they allow greater chemical control, improved reproducibility and the direct assessment of structure-property relations<sup>52,53</sup>.

The family of acenes belongs to this category<sup>54,55,56</sup>. They show large charge mobilities, so large as to suggest band-like transport for highly ordered thin films<sup>16,57</sup>. This feature makes them particularly useful in the effort to understand the dynamics of molecular self-organisation.

Like polymers, small molecular donors suffer from the band gap problem. Engineering strategies similar to ones adopted for polymers, like the combination of *D* and *A* groups<sup>52,58</sup>, have been capable to partially address the problem by improving orbital delocalisation and absorption at the same time.

The small size of these compounds has also introduced the possibility to build more complex architectures combining *D* and *A* groups in different arrangements and of various nature. This approach may not be advantageous for monomeric units but works well for stand-alone structures. These attempts have been quite effective in delivering rather large PCEs around 7%<sup>59,60,61</sup> that are important to prove that small molecules can be as effective as polymers but without some of the drawbacks.

## Acceptors

The classification of acceptor materials follows a different logic. Due to the prevalence of fullerene based acceptors over the last couple of decades, it is customary to divide acceptor materials in fullerene and non-fullerene acceptors. Naturally the second group is rather large and varied and has known a significant boost in the last couple of years<sup>62,63,64,65,66</sup>.

The convenience of fullerene derivatives is difficult to deny. They are cheap to produce, have high mobilities and show an isotropic transport given by the pronounced molecular symmetry<sup>32,67,68</sup>. The excellent transport properties are enhanced by the tendency of fullerenes to aggregate thanks to intermolecular  $\pi$ - $\pi$  interactions between delocalised electronic densities.

However, depending on the type of heterojunction, this last property can either prove benefi-

cial, as in the case of a planar heterojunction, or detrimental to thermodynamic stability as it happens in a bulk heterojunction. The main shortcoming of fullerenes is associated with their very poor absorption capabilities. Due to their symmetry, many transitions are prohibited. As a result, UV-visible absorption is very low, so much that for donor:fullerene blends, only the donor is considered as absorbing material. Fullerene derivatives are obtained by functionalising the original structure with groups that increase absorption in the target spectral range. These modifications may also optimise the LUMO level that is directly linked with the  $V_{oc}$  of the device.

As already mentioned, in the last few years the community has become more and more conscious about the constraints imposed by fullerene acceptors and has progressively moved towards non-fullerene ones that a recent body of work has revealed to be very promising in boosting conversion efficiency in the current generation of experimental organic photovoltaic devices.

## Materials for single component solar cells

Beyond the binary distinction between acceptors and donors, sits an interesting class of materials collecting all those molecular architectures that can be used as unique photoactive components in solar cells. These materials are employed in the production of SMOSCs and have the potential to play an important role in solving some of the issues affecting organic photovoltaic materials.

The interest in these compounds comes from the necessity to improve on the bulk heterojunction design, whose performances are affected by the thermodynamic instability of the interface and the limited control that is possible to exert over it<sup>[32][69][70]</sup>.

While new techniques and experimental protocols could, in principle, enhance control over morphology and instability could be dealt with by selecting better materials, the possibility to go beyond the bulk heterojunction remains extremely appealing. This is because directing the self-organisation of blends, responsible for the final morphology, is a very complex task<sup>[71]</sup>. At present, the only way to control it is by intervening on the active layer during deposition. Specific choices like relative percentage of donor and acceptor in the blend, selection of the solvent, environment at deposition and possible use of additives can be exploited as tools for

greater control<sup>32,69,70,72</sup>. For what concerns instability on the other hand, little can be done to inhibit the spontaneous reorganisation of materials after deposition. A notable example is provided by fullerene-based acceptors whose tendency to aggregate invariably results in performance drops during the operating life of a device<sup>73,74</sup>.

Therefore, also in the case of SMOSC materials, acting on the molecular blocks promises to be the most effective way forward. The design of molecular structures for SMOSCs is based around the<sup>71</sup> introduction of a further chemical constraint between the donor and the acceptor through a covalent linker, capable of limiting and constraining the self-organisation of the blend.

Depending on the specifics of the linker, two different strategies have been undertaken. The first possibility is to select a linker with a flexible structure and a strongly insulating character. This means that the linker has to be chosen so as to interrupt the  $\pi$ -conjugated structure between *D* and *A* and avoid substantial changes to the properties of the isolated moieties.

With a linker of this type, donor and acceptor moieties are still free to undergo aggregation to some extent and a *D/A* interface is still required to achieve exciton dissociation. According to this strategy, the covalent linker just acts as a mechanical constraint and is used to freeze the nanophase separation to produce and maintain the desired morphology. In Fig. 1.8, on the left, a schematic representation of polymeric and oligomeric systems that can be produced with this approach is presented.

These architectures have the ability to absorb light into long-lived charge transfer states that ultimately result in free charges transported along the polymer on the *D* and *A* moieties repeated along the backbone. In the case of polymers, self-organisation should not influence performance as much as in the case of bulk heterojunctions. Rather, performance is chiefly limited by the capacity of the new structure to generate and maintain free charges, i.e. by its ability to favour charge separation and avoid recombination.

The other possibility consists in choosing a rigid linker that is shorter and less insulating. In this way, compounds with a more complex electronic structure are obtained that retain the crucial properties of the isolated moieties but are able to achieve efficient exciton dissociation and ensure fast charge transport. Within the larger class of materials based on this design, it is particularly interesting to focus on the ones including small oligomers as donors.

The vast majority of these architectures have fullerene derivatives as acceptor groups and follow *D-A* or *D-A-D* design scheme, commonly referred to as dyads or triads. Like before, performances are limited by the capacity to produce charges but this time, also morphology at local and higher-scale plays an important role. Based on the packing properties in fact, charges are displaced with variable efficiency and this has to be considered in addition to the ability to generate free carries.

However complex, recent works have demonstrated the potential of these materials to reach quite large PCEs. Double-cable polymers based on flexible insulating linkers have been reported<sup>[75][76]</sup> with PCE as high as 6.30 %, and block copolymers built from more rigid linkers not far behind at 5.28 %<sup>[77][78]</sup>. Molecular heterojunctions and more in particular *D-A* dyads have recently passed the 1 % mark<sup>[79]</sup> and have quickly reached PCEs between 2 %<sup>[80][81][82][83][84][85][86][87]</sup> and 3%<sup>[88]</sup>.

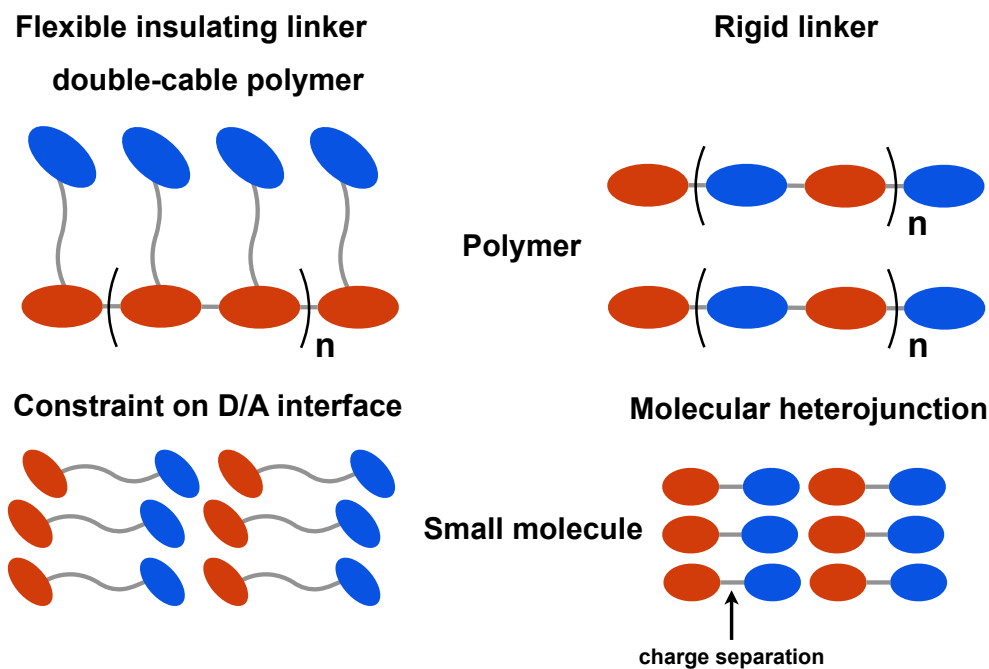


Figure 1.8: Schematic representation of the general architecture for SMOSC materials. Depending on the character of the linker the two moieties may be combined in a single architecture with markedly different character. On the *left*, an insulating linker produces assembly of molecules whose phase separation is mechanically controlled by the linker while most of the other properties of donor and acceptor moieties are preserved. On the *right*, the corresponding structures generated from a rigid linker. Structures are more compact and the isolated properties less preserved. These architectures should be able to achieve efficient dissociation on the molecule itself and ensure transport over the morphology. The D/A interface is no longer needed to dissociate the exciton.

This overview of the most prominent material classes investigated so far for organic solar cells closes this introductory chapter by highlighting the fundamental role of materials search. This aspect remains the most crucial to fulfil the promise of delivering commercially viable devices in the near future and certainly explains the extensive research that is being carried out throughout the community.

# Chapter 2

## Methods

Light to energy conversion processes, as in the case of the photovoltaic process, are multi-scale processes whose mechanisms crucially depend on length scales ranging from the molecular one at approximately  $10^{-1}$  nm to the typical device scale at approximately  $10^{-2}$  mm<sup>89,90</sup>. The modelling of these processes has to reflect this multi-scale character and thus requires the combination of different levels of theory to provide a satisfactory quantitative description<sup>91</sup>. Each level describes a different layer in the time scale domain, building on information obtained at lower time and length scales and in turn provides new parameters that inform the level above. A discussion of all these layers should start with the most fundamental scale and proceed upwards until all the macroscopic properties that describe the process are appropriately treated.

The smallest scale of interest is naturally the molecular scale. Molecular geometry and properties are determined by the electronic structure. Hence, the first layer in the theoretical treatment of photovoltaic materials modelling is occupied by electronic structure methods<sup>92</sup>. Indeed, an accurate description of the electronic distribution within the molecular structure is the fundamental input to the model and gives access to quantitative predictions of microscopic properties that, despite the intervening scale separation, have profound effects on photovoltaic performance<sup>93,94</sup>.

Within the community focused on the modelling of organic semiconductors, the methods most commonly employed are certainly density functional theory (DFT)<sup>95</sup> based approaches together with semiempirical methods<sup>96,97</sup>, a simplified and parameterised version of the

Hartree-Fock method conceived to decrease the overall computational cost.

In the following these classes of electronic structure methods will be outlined with particular focus on the aspects that are most relevant to the specific topic of organic semiconductors modelling.

## 2.1 Electronic structure methods for organic materials

Any accurate mathematical description of materials relies on the non-relativistic Schrödinger equation. The most general form of this equation is therefore the starting point of any electronic structure method. A molecular system can be conceptually reduced to a set of charged particles interacting among themselves. The behaviour of this system is described by a collective wave function governed by an Hamiltonian operator  $\hat{H}_{\text{many body}}$  that contains the description of the particle interactions. For an isolated system of  $N_n$  atomic nuclei and  $N_e$  electrons the many body problem can be expressed as:

$$\hat{H}_{\text{many body}} \Psi_a(\mathbf{q}_1, \dots, \mathbf{q}_{N_n}; \mathbf{r}_1, \dots, \mathbf{r}_{N_e}) = E_a \Psi_a(\mathbf{q}_1, \dots, \mathbf{q}_{N_n}; \mathbf{r}_1, \dots, \mathbf{r}_{N_e}) \quad (2.1)$$

with  $\mathbf{q}_i$  representing the nuclear coordinates and  $\mathbf{r}_i$  the electronic ones. Here, the time-independent Schrödinger equation is recast in the form of an eigenvalue problem. The index  $a$  runs over the infinite set of eigenvectors  $\Psi_a$  of the operator  $\hat{H}_{\text{many body}}$  with eigenvalues  $E_a$ . Each  $\Psi_a$  is interpreted as a collective wave function of all particles that describes their distribution in the ground state when  $a = 0$  or in any excited state of the system for  $a > 0$ . The operator  $\hat{H}_{\text{many body}}$  collects the kinetic terms and all the fundamental interactions  $\hat{V}...$  between all entities in the system:

$$\begin{aligned} \hat{H}_{\text{many body}} &= \hat{K}_e + \hat{K}_n + \hat{V}_{n-n} + \hat{V}_{e-e} + \hat{V}_{n-e} \\ \hat{K}_e + \hat{K}_n &= -\sum_{i=1}^{N_e} \frac{\hbar^2}{2m_e} \nabla_{\mathbf{r}_i}^2 + -\sum_{\alpha=1}^{N_n} \frac{\hbar^2}{2M_\alpha} \nabla_{\mathbf{r}_\alpha}^2 \\ \hat{V}_{n-n} &= \frac{e^2}{4\pi\epsilon_0} \sum_{\alpha,\beta}^{N_n} \frac{Z_\alpha Z_\beta}{|\mathbf{r}_\alpha - \mathbf{r}_\beta|} \\ \hat{V}_{e-e} &= \frac{e^2}{4\pi\epsilon_0} \sum_{i,j}^{N_e} \frac{1}{|\mathbf{r}_i - \mathbf{r}_j|} \\ \hat{V}_{n-e} &= -\frac{e^2}{4\pi\epsilon_0} \sum_{\alpha,i}^{N_n, N_e} \frac{Z_\alpha}{|\mathbf{r}_\alpha - \mathbf{r}_i|} \end{aligned} \quad (2.2)$$

The listed terms correspond to the kinetic contributions of electrons and nuclei and their instantaneous Coulomb interactions.

The general form of  $\Psi_a$  eigenvectors in Eq. 2.1 is a function of all nuclear and electronic degrees of freedom meaning that their precise knowledge is needed to describe their interactions and thus the dynamics of the system. This implies an enormous computational cost, often too large for the theory to be applied to any chemical system worth investigating, be it in the domain of organic electronics or in any other domain that aims to produce quantitative predictions. Simplification schemes are therefore required to lower the complexity and introduce more manageable mathematical objects that would make calculations easier. These schemes are built around the idea that particle-particle interactions can be approximated at the mean field level, i.e. each particle interacts with an average particle density describing the others. Depending on the particular simplification scheme adopted, many families of electronic structure methods can be derived. These methods have seen a proliferation in recent years due to the increased availability of computational resources and their ranks populate the modern day arsenal of quantum chemists.

## 2.2 The Born-Oppenheimer approximation

One of the most straightforward approximations rests on the often verified assumption that nuclear and electron dynamics happen on very different time scales, i.e. nuclei are much slower than electrons. This is justified by the simple observation that nuclei are orders of magnitude heavier than electrons. This is the premise underlying the *Born-Oppenheimer approximation*<sup>98</sup>, that offers a framework in which it is possible to decouple the two dynamics within the many body Schrödinger equation. In this picture, the electron wave function evolves according to the potential determined by the nuclei in a fixed configuration, so that one may write:

$$\hat{H}_e = \hat{K}_e + \hat{V}_{n-e} + \hat{V}_{e-e}$$
$$\hat{H}_e \Psi_k^e(\mathbf{q}_1, \dots, \mathbf{q}_{N_n} | \mathbf{r}_1, \dots, \mathbf{r}_{N_e}) = E_k(\mathbf{q}_1, \dots, \mathbf{q}_{N_n}) \Psi_k^e(\mathbf{q}_1, \dots, \mathbf{q}_{N_n} | \mathbf{r}_1, \dots, \mathbf{r}_{N_e}) \quad (2.3)$$

The dependence on the coordinates of the nuclei is preserved but, thanks to the decoupling, they enter as a set of external parameters. Despite this considerable improvement, the elec-

tronic wave function  $\Psi_k^e$  is still a function of all the electronic degrees of freedom. Other steps are required in order to further lower the number of degrees of freedom and finally deal with quantities that can be tackled numerically. Electronic structure methods can be classified according to the character of the approximation introduced at this step.

From the point of view of quantum theory, identical particles are indistinguishable. When many of them come together, a collective dynamics originates that is appropriately described according to the collective wave function, already shown in Eqs. [2.3](#) and [2.1](#). It makes thus little sense, in this context, to picture particles as independent objects and even more so to imagine independent descriptions of their dynamics. Yet, individual particles or at least, wave functions occupied by a single particle, are infinitely more convenient to describe and manipulate. However, it is fundamental for any simplification in this sense to be informed, as much as possible, by the constraints naturally emerging from many body quantum mechanics. The most important of these constraints is the one concerning the fermionic nature of electrons.

## 2.3 Hartree-Fock method

A particular ansatz for the many body wave function is based on the idea of factorising the ground state many body wave function  $\Psi_{k=0}^e$  in an antisymmetric combination of single-particle wave functions. This is at the core of the Hartree-Fock approximation<sup>92</sup>. This simplification trades the exact description of dynamical electron correlations for a theoretical simplicity that is almost unrivalled by other electronic structure methods. The loss of dynamical correlation depends on the description at mean field of the interaction. This description misses the extent at which electrons truly “keep away” from each other in the system dynamics.

The central assumption rests on the following relation:

$$\Psi_0^e(\mathbf{r}_1\sigma_1, \dots, \mathbf{r}_{N_e}\sigma_{N_e}) \sim \Phi_{1\dots N_e}(\mathbf{r}_1\sigma_1, \dots, \mathbf{r}_{N_e}\sigma_{N_e}) \quad (2.4)$$

$$\Phi_{a_1\dots a_{N_e}}(\mathbf{r}_1\sigma_1, \dots, \mathbf{r}_{N_e}\sigma_{N_e}) = \frac{1}{\sqrt{N_e!}} \begin{bmatrix} \varphi_{a_1}(\mathbf{r}_1\sigma_1) & \dots & \varphi_{a_{N_e}}(\mathbf{r}_1\sigma_1) \\ \vdots & & \vdots \\ \varphi_{a_1}(\mathbf{r}_{N_e}\sigma_{N_e}) & \dots & \varphi_{a_{N_e}}(\mathbf{r}_{N_e}\sigma_{N_e}) \end{bmatrix}$$

where the spin degrees of freedom  $\sigma$  have been written explicitly. By combining the variation principle with a requirement of orthonormality for each single-particle wave function, one may derive a set of  $N_e$  equations (one per electron) whose solution minimises the energy. This minimisation is restricted within the functional space of single Slater determinants of orthonormal single-particle wave functions  $\varphi_a$ :

$$-\frac{\hbar^2}{2m_e}\nabla^2\varphi_a(\mathbf{r}\sigma) + \frac{e^2}{4\pi\epsilon_0} \sum_{\sigma'} \int d^3\mathbf{r}' v_{\text{eff}}^{\text{HF}}(\mathbf{r}\sigma, \mathbf{r}'\sigma')\varphi_a(\mathbf{r}'\sigma) = \epsilon_a\varphi_a(\mathbf{r}\sigma) \quad (2.5)$$

where the effective potential is given as:

$$v_{\text{eff}}^{\text{HF}}(\mathbf{r}\sigma, \mathbf{r}'\sigma') = \delta_{\sigma\sigma'}\delta^{(3)}(\mathbf{r}-\mathbf{r}') [v_{n-e}(\mathbf{r}) + v_{\text{H}}(\mathbf{r})] + v_{\text{X}}^{\text{HF}}(\mathbf{r}\sigma, \mathbf{r}'\sigma')$$

$$v_{\text{H}}(\mathbf{r}) = \int d^3\mathbf{r}' \frac{1}{|\mathbf{r}-\mathbf{r}'|} \sum_{\sigma'} \sum_j^{N_e} |\varphi_j(\mathbf{r}'\sigma')|^2$$

$$v_{\text{X}}^{\text{HF}}(\mathbf{r}\sigma, \mathbf{r}'\sigma') = -\frac{1}{|\mathbf{r}-\mathbf{r}'|} \sum_j^{N_e} \varphi_j(\mathbf{r}\sigma)\varphi_j^*(\mathbf{r}'\sigma')$$

The key feature of these equations is that each electron feels the average electron cloud  $v_{\text{H}}$  and an exact description of exchange is ensured by the Slater determinant form. This set of equations is not linear, in particular the kernel term  $v_{\text{X}}^{\text{HF}}(\mathbf{r}\sigma, \mathbf{r}'\sigma')$  acts on  $\varphi_i$  through an integration over  $\mathbf{r}'$  introducing a highly non-local interaction accounting for electronic exchange. As a consequence, the best approximation to the ground state many body wave function can be obtained through self-consistent iteration<sup>99</sup> of the solution that is stopped once convergence below some threshold is attained.

As already mentioned, the Hartree-Fock approximation offers an exact treatment of electronic exchange but describes poorly dynamical electron correlation. Strategies to overcome this shortcoming exist and are based on the idea of building a complete orthonormal basis for the  $N_e$ -particle space by combining the complete single-particle orbital set coming from

each Hartree-Fock equation into Slater determinants. These approaches have limited applicability due to the fact that in practice, single-particle orbitals need to be in turn represented as finite combinations of functions called **basis set** functions<sup>[97]</sup>. The size of this basis set, that also determines the computational cost<sup>[100]</sup>, represents a limit to the larger functional space that can be spanned.

## 2.4 Semiempirical methods

Despite its convenience, the Hartree-Fock method still implies the calculation of a large number of two-centre integrals. To give an idea, their number depends on the size of the basis set, i.e. the set of  $M$  functions chosen to construct the larger single-particle orbitals  $\{\varphi_i\}_{i=1,\dots,N_e} = \{\sum_u C_{iu}\chi_u\}_{i=1,\dots,N_e}$  of the complete system. The number of integrals grows as  $M^4$ . For this reason further simplification schemes have been devised in order to curb the number of integrals that need to be computed. The simplification is performed by introducing a number of parameters whose values may be chosen according to the results of higher level calculations or, more commonly, according to available experimental data. The methods resulting from the application of these schemes belong to the family of *semiempirical methods*<sup>[96,97]</sup> that, despite their approximate nature, remain convenient in many circumstances to perform preliminary analyses or other kinds of predictions.

Hence, the goal is to reduce the number of Coulomb and exchange integrals between combinations of basis set functions. By expanding a single-particle wave function in the Hartree-Fock approach over a basis set:

$$\varphi_i(\mathbf{r}) = \sum_u C_{iu}\chi_u \quad (2.6)$$

and substituting this expression in the Hartree-Fock equations, the general form of exchange and Coulomb integrals becomes:

$$\langle uv|st\rangle = \int d^3\mathbf{r}_1 d^3\mathbf{r}_2 \chi_u(\mathbf{r}_1)\chi_v(\mathbf{r}_1) \frac{1}{|\mathbf{r}_1 - \mathbf{r}_2|} \chi_s(\mathbf{r}_2)\chi_t(\mathbf{r}_2) \quad (2.7)$$

A first simplification scheme is the so-called *complete neglect of differential overlap* (CNDO)<sup>[101]</sup> and it is based on the following rule:

$$\langle uv|st\rangle = \delta_{uv}\delta_{st}\langle uu|ss\rangle. \quad (2.8)$$

This means that all interactions are neglected except the ones between “*partial densities*”  $\chi_u(\mathbf{r})\chi_u(\mathbf{r})$  and  $\chi_s(\mathbf{r})\chi_s(\mathbf{r})$ . These partial densities can be on the same atom (one centre integrals) or on different atoms (two centre integrals). Moreover, these integrals are considered only for valence electrons while core electrons are collectively described through effective potentials. The values of these integrals are given through tabulated parameters according to:

$$\langle uu|ss\rangle = \gamma_{AA} \quad \text{where } \gamma_{AA} \text{ is equal to: } IP_A - EA_A \quad (2.9)$$

if functions  $s$  and  $u$  are centred on the same atom  $A$

$$\langle uu|ss\rangle = \frac{\gamma_{AA} + \gamma_{BB}}{2 + r_{AB}(\gamma_{AA} + \gamma_{BB})} \quad (2.10)$$

if functions  $s$  and  $u$  are centred on different atoms  $A, B$

This scheme has notable shortcomings, particularly when applied to spectroscopy. In fact, it is not able, by construction, to differentiate between singlet and triplet states. To overcome these shortcomings it is possible to opt for less drastic reductions in the number of integrals. Among the improvements on this scheme one is worth of particular attention because, to this day, it remains widely employed. It will be used in particular to give estimates of orbital overlaps with a good cost-to-accuracy ratio when modelling charge transfer between pairs of molecules in chapter 3 and 4.

The improved scheme is called *intermediate neglect of differential overlap* (INDO)<sup>102</sup>. It rests on the same simplification as the previous scheme but it retains a larger number of integrals:

$$\langle uv|st\rangle = \delta_{uv}\delta_{st}\langle uu|ss\rangle \quad \text{only if } u \text{ and } s \text{ are centred on different atoms} \quad (2.11)$$

This reduction is applied only to two centre integrals while integrals involving pairs of functions centred on the same atom are retained and their values are approximated according to a new set of parameters:

$$\begin{aligned} G_{ss} &= \langle ss|ss\rangle & G_{pp} &= \langle pp|pp\rangle \\ G_{sp} &= \langle ss|pp\rangle & G_{pp'} &= \langle pp'|pp'\rangle \\ L_{sp} &= \langle sp|sp\rangle \end{aligned} \quad (2.12)$$

All these parameters are attributed according to spectroscopic measurements with a widely employed parameterisation being the one by M. Zerner<sup>96</sup>. The method with this parameterisation is called Zerner intermediate neglect of differential overlap, or ZINDO method.

## 2.5 Density functional theory

In the last few decades, theoretical chemistry has seen the rise of DFT as one of its most prominent computational tools<sup>[103]</sup>. Density functional theory approaches are nowadays so varied and refined that constitute remarkably versatile and invaluable tools to direct the experimental endeavour and complement it with a truly microscopic physical insight.

Density functional theory starts from the many body equation and reformulates the problem shifting the focus from the many body wave function  $\Psi_{k=0}^e(\mathbf{r}_1, \dots, \mathbf{r}_{N_e})$  to the electronic density  $\rho(\mathbf{r})$ .  $\rho$  can be obtained from  $\Psi_{k=0}^e$  by integrating out all the electronic degrees of freedom except for one set:

$$\rho(\mathbf{r}) = \int d^3\mathbf{r}_2 \dots d^3\mathbf{r}_{N_e} \Psi_0^e(\mathbf{r}, \mathbf{r}_2, \dots, \mathbf{r}_{N_e}) \cdot \Psi_0^{e*}(\mathbf{r}, \mathbf{r}_2, \dots, \mathbf{r}_{N_e}) \quad (2.13)$$

With this shift of paradigm, the quantum mechanics of many body systems can be recast in a new form where, instead of solving the Schrödinger equation, an energy functional dependent on density is minimised with a Lagrange multiplier imposing that the density integrated over space returns the number of electrons in the system  $N_e$ :

$$\left. \frac{\delta}{\delta\rho(\mathbf{r})} \left[ E[\rho] - \mu \left( \int d^3\mathbf{r} \rho(\mathbf{r}) - N_e \right) \right] \right|_{\rho(\mathbf{r})=\rho_{\text{gs}}(\mathbf{r})} = 0 \quad (2.14)$$

The general form of this functional can be given as follows:

$$E[\rho] = \int \rho(\mathbf{r})v(\mathbf{r})d^3\mathbf{r} + F_{HK}[\rho(\mathbf{r})] \quad (2.15)$$

The functional in this expression contains a term dependent on the external potential determined by the nuclei and then a term that collects all the possible interactions between the electrons  $F_{HK}[\rho(\mathbf{r})]$ . This term is independent from the external potential and contains electronic kinetic terms, all correlations and fermionic effects in the set of  $N_e$  electrons. It is important to stress that these expressions represent an **exact** formulation of quantum mechanics with the central quantity being the ground state density  $\rho(\mathbf{r})$ , that encodes all the relevant information about the system. Density is a much more manageable quantity with respect to the many body function  $\Psi_0^e$  and, in principle, it is a physical observable<sup>[104]</sup>. The problem of minimising the density functional however, is far from trivial and all the difficulty intrinsic to the many body Schrödinger equation is just transferred to the  $F_{HK}$  term. Also in this case, further simplifications are required to produce any meaningful prediction.

In a similar fashion to the Hartree-Fock approach, a particular form of the density can be expressed as a series of one-electron orbitals according to

$$\rho(\mathbf{r}) = \sum_i^{N_e} f_i |\phi_i(\mathbf{r})|^2 \quad (2.16)$$

This expression is at the basis of a mapping proposed by Kohn and Sham<sup>[95][105]</sup>, between the original theory and a system of noninteracting particles that share the same ground state density of the many body system. In this case, a set of Schrödinger-like equations can be written,

$$\left[ -\frac{\nabla_{\mathbf{r}}^2}{2m_e} + v_H[\rho](\mathbf{r}) + v_{n-e}[\rho](\mathbf{r}) + v_{xc}[\rho](\mathbf{r}) \right] \phi_a(\mathbf{r}) = \epsilon_a \phi_a(\mathbf{r}) \quad (2.17)$$

where the kinetic term is that of a noninteracting system of particles and should not be confused with the exact one acting on the whole many body wave function in the original formulation. The potential terms  $v_H$  and  $v_{n-e}$  represent, respectively, the classical interaction potential between  $N_e$  electrons and the interaction between electrons and nuclei in the Born-Oppenheimer approximation, while  $v_{xc}$  is the *exchange-correlation* potential term accounting for all the many body effects that characterise the quantum dynamics and are missing in the previous terms. Despite the mapping into a noninteracting system of particles, this last formulation of the initial problem is still **exact** and thus yields the exact ground state electronic density corresponding to the many body system. The central problem is reduced in this way to the determination of the exchange-correlation functional.

A priori, an exact form of this functional would provide an exact description of the initial system. Kohn-Sham equations represent the foundation for a large majority of DFT applications employed today. As it will be shown further on in the chapter, not knowing the exact exchange-correlation confers to DFT a remarkable versatility and the capacity to capture the behaviour of vastly different systems. Despite the search for the exact functional is still ongoing, this unknown term subject to relatively few constraints has allowed the development of approaches tailored to different classes of physical systems, often able to capture accurately very specific behaviours<sup>[106]</sup>.

## 2.6 Functionals and their classification

The many functionals developed up to this day<sup>[107]</sup> can be classified in terms of their accuracy according to a categorisation first proposed by J. Perdew<sup>[108]</sup>. This section briefly outlines the general principles on which this categorisation is based.

The first assumption that is made on the exchange-correlation functional  $E_{xc} = \int d\mathbf{r} v_{xc} \rho(\mathbf{r})$  is that it can be separated into the sum of an exchange part  $E_x$  and a correlation part  $E_c$ . Starting from this general form, all DFT approaches can be derived by choosing the appropriate form for  $E_{x/c}$

In the most simple form the functional is taken to be the integral of a function of the density. This is called the *local (spin) density approximation* L(S)DA. The integrated function has a local character in the sense that it only depends on the density at a specific position in space  $\mathbf{r}$ , as follows:

$$E_{c/x} = \int d\mathbf{r} v_{c/x}[\rho(\mathbf{r})] \rho(\mathbf{r}) \quad (2.18)$$

No information is encoded about the local variation of the density. This approximation can be rather efficient for metals or materials with many, highly delocalised electrons yet it is rather inefficient for molecules. In molecules in fact, electronic structure reflects the arrangement of nuclei that may be very different from the regular structures found in many metals. Variations of the density over small distances are such that the inclusion of higher order terms in the Taylor expansion can strongly increase the predictive power. This is the reason behind the introduction of a second generation<sup>[109]</sup> of approximate functionals that are grouped under the label *generalised gradient approximation* GGA<sup>[110]</sup> (or meta-GGA) and includes functionals based on the following, general structure

$$E_{c/x} = \int d\mathbf{r} v_{c/x}[\rho(\mathbf{r}), \nabla\rho(\mathbf{r}), \nabla^2\rho(\mathbf{r})] \rho(\mathbf{r}) \quad (2.19)$$

A further important development that is essential to capture the main features of many functionals in use today relies on the inclusion of explicit exchange of Hartree-Fock type. The basic idea rests on the simple observation that the Slater determinant built with the occupied Kohn-Sham orbitals is the exact solution in the case of the noninteracting system. This means that when the interaction between different electrons is turned on the true exchange and correlation functional should contain at least a part of this exchange.

In view of this observation a percentage of Hartree-Fock exchange can be explicitly added to  $E_x$  and new functionals can be constructed. These functionals are called *hybrid functionals* and are currently among the ones with the best performances.

Historically, they were the ones whose advent allowed DFT to go below chemical accuracy in terms of predicted energy and contributed to the spread and generalisation of DFT within the chemical community<sup>[107]</sup>.

The general form of an hybrid functional can be given as follows:

$$E_{xc} = E_{xc}^{LDA} + a_1 (E_x^{HF} - E_x^{LDA}) + a_2 \Delta E_x^{GGA} + a_3 \Delta E_c^{GGA} \quad (2.20)$$

To hybrids belongs the renowned B3LYP functional<sup>[111][112]</sup> that is one of the most widely employed today and will be used in the applications of DFT considered in the text.

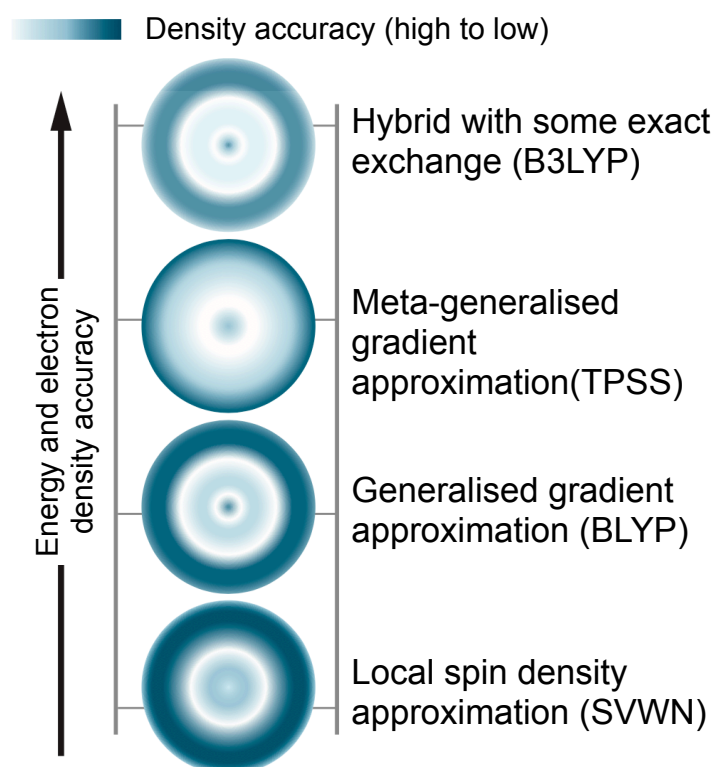


Figure 2.1: Graphical representation of the Jacob's ladder of chemical accuracy<sup>[108]</sup> adapted from ref. <sup>[113]</sup>. For each rung in the ladder an indication of the accuracy is given according to the heat map shown. In addition, an example of a DFT approach corresponding to each rung is given.

## 2.7 Time dependent extension

DFT can be extended to include interactions with time-dependent external potentials<sup>[14]</sup>. This is essential when describing the interaction of molecular systems with external fields of various nature, with the most relevant being without doubts the electromagnetic field, at the basis of the description for light-matter interactions. Strictly speaking, Kohn-Sham orbitals  $\{\varphi_a(\mathbf{r})\}_{a=1,\dots,N_e}$  should only be interpreted as a mathematical basis useful in realising the mapping between the interacting particle system and the auxiliary noninteracting one. Nonetheless, in the context of time-dependent DFT, it is possible to exploit the same mapping between the two systems and relate their responses in the case of a small external perturbation in the linear regime. To understand how, it is convenient to go back to the initial formulation of the many body problem in the form of the Schrödinger equation.

If a time-dependent perturbation is applied to the many body system and its intensity is small with respect to the internal interactions, it is possible to describe the total variation of the density operator as

$$\delta\hat{\rho}(\mathbf{r},t) = \int_0^\infty dt' \int d^3\mathbf{r}' \frac{\delta\hat{\rho}(\mathbf{r},t)}{\delta v(\mathbf{r}',t')} \delta v(\mathbf{r}',t') \equiv \int_0^\infty dt' \int d^3\mathbf{r}' \chi(\mathbf{r},t|\mathbf{r}',t') \delta v(\mathbf{r}',t') \quad (2.21)$$

that integrates over time and space all density variations produced by variations of the time-dependent potential.  $\chi$  is the linear response function of the many body system and can be also interpreted as the two-point correlation function between two consecutive measurements of the density operator.

In the interaction picture this reads

$$\chi(\mathbf{r},t|\mathbf{r}',t') = i \theta(t' - t) \langle \Psi_0^e | [\hat{\rho}(\mathbf{r}',t'), \hat{\rho}(\mathbf{r},t)] | \Psi_0^e \rangle \stackrel{\text{F.T.}}{t \rightarrow \omega} \chi(\mathbf{r},\mathbf{r}',\omega) \quad (2.22)$$

$$\chi(\mathbf{r},\mathbf{r}',\omega) = \sum_{k=1} \frac{\langle \Psi_0 | \hat{\rho}(\mathbf{r}) | \Psi_k \rangle \langle \Psi_k | \hat{\rho}(\mathbf{r}') | \Psi_0 \rangle}{\omega - (E_k - E_0) + i\eta^+} + \text{c.c.}$$

In this expression  $\{\Psi_k\}$  are the excited states of the many body system, and  $E_k$  their energies. Applying the same procedure to the Kohn-Sham system yields a similar quantity involving the single-particle orbitals  $\{\varphi_a\}$ .

$$\chi_{\text{KS}}(\mathbf{r},\mathbf{r}',\omega) = \sum_{a,b} (f_a - f_b) \delta_{\sigma_a \sigma_b} \frac{\varphi_a^*(\mathbf{r}) \varphi_b(\mathbf{r}) \varphi_b^*(\mathbf{r}') \varphi_a(\mathbf{r}')}{\omega - (\varepsilon_b - \varepsilon_a) + i\eta^+} + \text{c.c.} \quad (2.23)$$

where the  $(f_a - f_b)$  is non zero only if  $a$  and  $b$  are a pair of occupied and unoccupied Kohn-Sham orbitals from the Kohn-Sham set. The functional derivative is taken, this time, over the time-dependent potential in the non interacting system  $v_{KS}$ .

The two response functions are related by a very important equation that is often referred to as the central equation<sup>[95][115]</sup> in TD-DFT:

$$\chi(\mathbf{r}, \mathbf{r}', \omega) = \chi_{KS}(\mathbf{r}, \mathbf{r}', \omega) + \int d^3 \mathbf{r}_1 d^3 \mathbf{r}_2 \chi_{KS}(\mathbf{r}, \mathbf{r}_1, \omega) \left[ \frac{1}{4\pi\epsilon_0} \frac{e^2}{|\mathbf{r}_1 - \mathbf{r}_2|} + f_{xc}(\mathbf{r}_1, \mathbf{r}_2, \omega) \right] \chi(\mathbf{r}_2, \mathbf{r}', \omega) \quad (2.24)$$

where  $f_{xc}$  is called exchange-correlation kernel and is given by  $\mathcal{F} \left[ \frac{\delta V_{xc}[\rho](\mathbf{r}_1, t)}{\delta \rho(\mathbf{r}_2, t')} \right]$ . Through a series of steps and substitutions, it is possible to recast this equation into an eigenvalue problem, obtained by dropping also the time dependence of the time-correlation kernel, an approximation known as adiabatic local density approximation (ALDA).

In this form, the poles of the many body response function, coinciding with the many body excitation energies are reconstructed by combining energy differences  $\epsilon_b - \epsilon_a$  between occupied and unoccupied KS orbitals and the transitions are weighed with transition densities between these orbitals.

The eigenvalue problem from Eq. [2.24](#) can be expressed in a matrix form, after some non trivial algebra<sup>[115]</sup>

$$\begin{bmatrix} A & B \\ B^* & A^* \end{bmatrix} \begin{bmatrix} X_{\omega_k} \\ Y_{\omega_k} \end{bmatrix} = \omega_k \begin{bmatrix} -1 & 0 \\ 0 & 1 \end{bmatrix} \begin{bmatrix} X_{\omega_k} \\ Y_{\omega_k} \end{bmatrix} \quad (2.25)$$

where entries of  $A$  and  $B$  submatrices have the form:

$$\begin{aligned} A_{abcd} &= \delta_{ac} \delta_{bd} (\epsilon_b - \epsilon_a) + \\ &+ \int d^3 \mathbf{r}_1 d^3 \mathbf{r}_2 \varphi_a^*(\mathbf{r}_1) \varphi_b(\mathbf{r}_1) \left[ \frac{1}{|\mathbf{r}_1 - \mathbf{r}_2|} + f_{xc}(\mathbf{r}_1, \mathbf{r}_2, \omega) \right] \varphi_c^*(\mathbf{r}_2) \varphi_d(\mathbf{r}_2) \quad (2.26) \\ B_{abcd} &= \int d^3 \mathbf{r}_1 d^3 \mathbf{r}_2 \varphi_a^*(\mathbf{r}_1) \varphi_b(\mathbf{r}_1) \left[ \frac{1}{|\mathbf{r}_1 - \mathbf{r}_2|} + f_{xc}(\mathbf{r}_1, \mathbf{r}_2, \omega) \right] \varphi_c^*(\mathbf{r}_2) \varphi_d(\mathbf{r}_2) \end{aligned}$$

Solving this matrix equation yields a set of eigenvalues  $\omega_k$  that represent the excitation energies  $\omega_k = E_k - E_0$  and a set of eigenvectors that express the transition from  $\Psi_0$  to  $\Psi_k$  in terms of ‘‘particle-hole transitions’’ between occupied-unoccupied orbitals of the Kohn-Sham

system. Hence, it is possible to reconstruct the properties of the exact excited states from a series of transitions between occupied and unoccupied Kohn-Sham orbitals, that reproduce the true energies and allow an evaluation of transition intensities.

It is straightforward to see, at this point, that such information grants access to key molecular quantities resulting from the action of –weak– external time-dependent fields perturbing the system, like the absorption spectrum.

## 2.8 Modelling organic materials with DFT

As already remarked, the accuracy that can be achieved by DFT approaches depends on the choice of the exchange-correlation functional. This freedom has contributed to the immense success of DFT that can be tuned according to the system at hand while being able to provide a good description for a relatively small computational cost.

In the case of molecular materials, the functional most frequently employed is probably B3LYP<sup>[11][116]</sup>. This functional belongs to the class of global hybrids in which, as discussed, the exchange-correlation functional is chosen to carry an explicit fixed contribution of non-local Hartree-Fock exchange (around 20 %). Despite its convenience, this approach is not the most versatile and it is important to stress a few drawbacks that, in the case of organic semiconductors, may lead to inaccurate predictions.

One of the most important shortcomings of DFT to keep in mind when investigating molecular solids is the difficulty of standard exchange-correlation functionals to describe so-called “weak” interactions that emerge for the intrinsic quantum nature of electronic densities. Dispersion interactions between induced dipoles in different molecules or in different structures on the same molecular architecture are usually poorly described.

A rather straightforward approach to adopt is to explicitly include an empirical correction on top of DFT calculations. This strategy has proven quite successful in describing dispersion interactions with one notable example being the correction proposed by S. Grimme *et al.*<sup>[117][118][119]</sup>. This correction includes a series of dispersion coefficients and cutoff radii for pairs of atoms whose values are chosen according to other first principles calculations. The atomic environment is also taken into account to some degree in the determination of Van

der Waals coefficients.

The particular form of the energy dispersion correction (D3<sup>[120]</sup>) applied to the systems studied in this work to complement the DFT approaches has the following form:

$$E_{\text{disp}} = -\frac{1}{2} \sum_{\substack{i,j \\ \in \text{atoms}}} \left( \frac{C_{6ij}}{r_{ij}^6} f_6^{\text{damp}}(r_{ij}) + \frac{C_{8ij}}{r_{ij}^8} f_8^{\text{damp}}(r_{ij}) \right) \quad (2.27)$$

where

$$f_n^{\text{damp}}(r_{ij}) = \frac{s_n}{1 + 6 \left( \frac{r_{ij}}{s_{R,n} R_0^{ij}} \right)^{-\gamma}} \quad (2.28)$$

The proliferation of parameters is necessary to allow the possibility of tuning the correction according to the DFT functional selected and adjusting the functional description of the potential that the different combined terms generate. In particular,  $s_{R,n}$  and  $s_n$  are scaling factors dependent on the order  $n$ .  $f_{ij}^{\text{damp}}$  is a damping factor to control the weight of the correction term according to the length-scale and also to define the steepness of the function for small distances, through  $\gamma$ .  $R_0^{ij}$  is the cutoff distance of the interaction between the atom pair  $i, j$  and  $C_{nij}$  are the coefficients specific for the atomic pair.

Another important point concerns the description of the electron distribution. As seen, organic semiconductors owe much of their properties to the formation of  $\pi$ -conjugated structures over which electrons can delocalise. This feature of the electronic density can be affected by a well-known problem of DFT that is the *electron self-interaction error*<sup>[113][121]</sup>. With respect to Hartree-Fock, the approximate description of exchange and correlation through the xc-functional leads to an incomplete cancellation of Coulomb self-interactions of one-electron densities. This introduces a spurious repulsive term that results in an overestimation of electron delocalisation. In the case of organic semiconductors, this means that (1) energies of the HOMO are usually too high because electrons are destabilised by the residual self-interaction, (2)  $\pi$ -conjugation is overestimated and (3) charge transfer (CT) transitions, highly relevant for photovoltaic processes, are usually difficult to describe appropriately.

A way around this is to rely on long range corrected functionals<sup>[122]</sup>, capable of performing a scale-dependent tuning of the Hartree-Fock exchange, and the pure DFT approach. This tuning is based on the partitioning of the Coulomb operator in two terms governing the short-range and long-range regimes.

$$\frac{1}{r} = \frac{\text{erf}(\mu r)}{r} + \frac{1 - \text{erf}(\mu r)}{r} \quad (2.29)$$

Within the two scale ranges it is possible to choose different mixtures of semi-local correlation and Hartree-Fock exchange with the Hartree-Fock component being dominant in the long-range, so that the appropriate  $\frac{1}{r}$  behaviour can be reproduced. Different procedures exist to fix the value of the scale parameter  $\mu$ , with the most common being a fit on a set of test compounds followed by the assumption of transferability to similar systems.

Caution is also needed in the interpretation of the energy gaps between orbitals coming from DFT calculations. In molecular systems there are two important energy gaps that provide fundamental information on the material fitness to photovoltaic applications. The *transport gap*  $\Delta E_{\text{transp.}}$  defined by the difference in ionisation potential *IP* (i.e. the energy necessary to extract an electron from the neutral molecule) and electron affinity *EA* (i.e. the energy released when an electron is added to the neutral molecule) and the *optical gap*  $\Delta E_{\text{opt.}}$ . This last is lower than the transport gap by an amount that can be interpreted, in a single-particle orbital picture, as the binding energy between the excited electron and the hole. This binding energy is particularly large for organic materials, for which the delocalisation over small scale  $\pi$ -conjugated structures, translates into  $E_b$  in the order of tenths of an eV (often approaching 1 eV).

These two gaps, in principle, cannot be accessed from data produced by Kohn-Sham DFT calculations, of which only the HOMO eigenvalue has a physical interpretation, aside from the uncertainty coming from the delocalisation error. However, it has been observed empirically that the predicted HOMO-LUMO gap at B3LYP level often reproduces well the experimental optical gaps. This suggests that exchange-correlation functionals with the explicit inclusion of some proportion of non-local Hartree-Fock exchange (B3LYP, 20% HF) can be used to tune the theoretical HOMO-LUMO gap so as to reproduce either the transport or the optical gap.

Indeed, it has been shown<sup>[123]</sup> that a non-empirical system-specific tuning procedure can achieve excellent agreement for many families of compounds when used in combination with long range corrected functionals that allow the separation between small and large scale, thus establishing the possibility of a reliable interpretation of DFT eigenvalues for HOMO and

LUMO orbitals in the generalised Kohn-Sham formalism.

On the practical side, this fact provides a theoretical justification to the direct interpretation of DFT data that will be presented further on and also stand as further proof of the versatility of DFT approaches when a pragmatic stance is taken.

## 2.9 Beyond molecular scale: supramolecular organisation

Modelling molecular systems microscopically offers invaluable insight on the macroscopic behaviour of materials<sup>90</sup>. However, depending on the particular properties and on the system under investigation, the molecular environment at different scales has the ability to modulate the system responses and, sometimes, to deeply affect its large-scale properties.

Due to the vastness of the chemical space occupied by organic semiconductors<sup>1124</sup>, the variety of behaviours and effects is so large that a case-by-case investigation should, in principle, be carried out each time, a prospect that often seems overwhelming. Probing macroscopic properties translates into the simulation of the collective behaviour of a large number of interacting molecules. The simulation should be able to reproduce as accurately as possible all relevant interactions responsible for the self-organisation of the material. In this way a realistic description of the details of the supramolecular structure can be provided.

Similarly to what happens for electronic structure methods, it is mandatory to devise strategies able to reduce the computational cost implied by the treatment of all degrees of freedom participating in the dynamics of aggregated molecules in condensed phase. The dynamics of self-organisation may proceed at very different paces within different materials and is crucially dependent on the processing conditions. For photovoltaic applications, organic semiconductors are widely employed in thin films. Manufacturing of these films can be done via a number of techniques developed throughout the years by experimentalists<sup>125,126</sup>. These techniques can be quite varied and imply the use of solvents or particular physical conditions of pressure and temperature. The final morphology in condensed phase is highly dependent on the interplay between the interactions driving aggregation and the conditions determined by the deposition technique. Large polymers with complex monomeric units mainly interacting through “weak” dispersion forces will very likely show a disordered morphology and local order will appear on relatively small scales. Conversely, small molecules interacting

via relatively large dipole moments will organise more easily and possibly produce larger ordered regions. These two opposite behaviours show that, in order to describe appropriately the morphology in condensed phase, different strategies are required. A strategy focusing on the two ends of this *morphology spectrum* between disordered (amorphous) and ordered (crystalline) phases can be defined.

In the case of ordered morphology, one can exploit the translational symmetry intrinsic to crystalline media. This symmetry allows a considerable reduction in the number of degrees of freedom to treat and consequently, the direct use of electronic structure methods to describe the molecular environment in crystals. However, one importation complication emerges. The knowledge of the crystal motif is required as input and organic materials often exhibit polymorphism, resulting in macroscopic materials characterised by a number of regions with potentially different local order emerging from competing crystal structures within the system. As it will be discussed later, the prediction of crystal polymorphs has been the focus of intense research in recent years but, despite considerable recent advances<sup>[127][128][129]</sup>, remains a highly demanding and complex task<sup>[129][130][131]</sup>.

In the case of disordered morphologies, the natural choice for the computational approach is classical molecular dynamics (MD). MD is a very powerful tool that has greatly benefitted the field of materials science. It allows a description of the macroscopic properties of the aggregate phase while taking into account the effect of external thermodynamic variables like pressure and temperature. Provided that it is properly informed on the molecular details from higher levels of theory, like DFT, MD simulations can be very accurate and provide reliable, quantitative predictions of key properties for many materials. However, the lack of symmetry often translates in an important limitation on the final length-scale at which the condensed phase can be accessed, even if this limitation is strongly system-dependent.

Luckily, most properties relevant to photovoltaic performance are mostly determined by supramolecular structure at scales accessible through MD simulations<sup>[132]</sup>, with a notable exception being charge carrier mobility that can nonetheless be estimated with sufficient accuracy<sup>[89][90]</sup> as will be shown further on in chapters three and four.

This second level of methods employed to probe supramolecular structure in condensed phase will be presented in the following.

## 2.9.1 Classical molecular dynamics

Classical molecular dynamics is a computational method that is able to simulate the behaviour of many molecules and to describe their interactions in a realistic manner. The method is based on solving Newton's equations for a group of atoms under a set constraints. The treatment of the dynamics is therefore classical and allows a sampling of the configuration space of molecular systems. The effectiveness of MD has been largely demonstrated by the huge success and its current pervasiveness throughout materials science, chemistry, biology and physics.

MD takes advantage of the same, large time-scale separation between the dynamics of electrons and nuclei at the basis of the Born-Oppenheimer approximation. Where electronic structure deals mostly with electrons for fixed nuclei configurations, MD deals with the dynamics of nuclear configurations. Electronic degrees of freedom are integrated out and the details of electronic structure are encoded into a series of geometrical constraints on the nuclear configurations, i.e. molecular geometries. At the same time a set of coarse-grained parameters emerges governing the interactions between the degrees of freedom left by the application of the constraints. The form of these constraints is often given on the basis of reasonable physical assumptions,

$$U = U_{\text{bonded}} + U_{\text{non-bonded}} \quad (2.30)$$

$$U_{\text{bonded}} = U_{\text{stretch}} + U_{\text{bends}} + U_{\text{torsions}} + U_{\text{impropers}}$$

$$U_{\text{non-bonded}} = U_{\text{van der Waals}} + U_{\text{electrostatic}}$$

Bonded interactions model the oscillations around nuclear equilibrium conformation. These oscillations are produced by the interaction with neighbouring molecules and favoured by thermal motion. The functional form of the potentials is chosen to describe these motions in a way that best reproduces the physics near equilibrium:

$$\begin{aligned} U_{\text{stretch}} &= \sum_{\text{bonds}} \kappa_b (b - b_{\text{eq}})^2 & U_{\text{bends}} &= \sum_{\text{angles}} \kappa_{\theta} (\theta - \theta_{\text{eq}})^2 \\ U_{\text{torsions}} &= \sum_{\text{torsions}} \sum_n \kappa_n (1 + \cos(n(\varphi - \varphi_{\text{eq}}))) & U_{\text{impropers}} &= \sum_{\text{impropers}} \kappa_{\psi} (\psi - \psi_{\text{eq}})^2 \end{aligned} \quad (2.31)$$

Nonbonded interactions, on the other hand, take care of the residual long range effects of electronic distribution and nuclear charges. The Van der Waals (or dispersion) term models interactions produced by the quantum character of the electronic density (i.e. induced dipoles

interactions) while the electrostatic term deals with the effects of nuclear and electronic charges:

$$U_{\text{van der Waals}} = \sum_{\text{atom pairs}} 4\epsilon_{\text{pair}} \left[ \left( \frac{\sigma_{\text{pair}}}{r} \right)^{12} - \left( \frac{\sigma_{\text{pair}}}{r} \right)^6 \right]$$
$$U_{\text{electrostatic}} = \sum_{\text{atom pairs}} -\frac{1}{4\pi\epsilon_0} \frac{q_a q_b e^2}{r} \quad (2.32)$$

Parameters appearing in Eq.s [2.31](#), [2.32](#),  $\kappa$ ,  $\sigma$ ,  $\epsilon$  together with the equilibrium values of all residual degrees of freedom are the coarse-grained quantities informing MD about the electronic structure details that should be retained.

The collection of these parameters defines a *force field*. A large number of force fields have been developed throughout the years. They differ on the basis of the scheme adopted to assign values to the parameters, that is often tailored to the foreseen usage, with applications ranging from biomolecules to liquid crystals.

In this work in particular, the DREIDING force field<sup>[133]</sup> and a force field derived from the well-known CHARMM force field, CGenFF<sup>[134][135]</sup> have been used for the description of organic semiconductors in different contexts.

The philosophy underlying the parameterisation scheme of the first tries to limit as much as possible the proliferation of atom types. Equilibrium values of all geometry parameters are chosen according to the rules suggested by the hybridisation of bonding atomic orbitals and interaction coefficients are rather constrained.

Conversely, CGenFF, assigns parameters and equilibrium values of geometrical features with the aim of maximising the quality of the description to the expense of transferability. The parameters are many to account for all the possible atomic local environments. More specifically, a large range of chemical groups are parameterised taking into account functional groups frequently found in organic molecules like heterocyclic structures.

## 2.9.2 Simulating the amorphous phase

The application of MD to the sampling of amorphous configurations of organic materials is rather straightforward. A sensible force field is chosen to parameterise the geometry and the atoms in the compound and a system is built by placing a number of molecules in a simula-

tion volume. The number of molecules determines the computational cost of the procedure and usually a good balance between affordability and accuracy can be reached with systems in the order of  $10^3$  molecules.

As already pointed out, this number is ridiculously small compared to the typical molecules in an experimental sample  $\sim N_{\text{Avogadro}}$ , translating in the ability of MD to probe length scale in the order of 10-100 nm at best against the  $\mu\text{m}$  or mm (sometimes up to cm) scale of real-life systems. This situation may lead to the emergence of artifacts and finite size effects and can be made worse by the application of periodic boundary conditions. This last consists in simulating identical copies around the central system at the same time. These copies are used to replace molecules diffusing out of the simulation box with other molecules entering from the opposite side. Despite these limitations that may indeed lead to important deviations in the simulated behaviour, it turns out that, for many macroscopic properties of interest, even small samples can give an indication of the larger scale behaviour with negligible finite size effects.

The schemes adopted to assign initial positions and velocities to molecules, make it necessary to perform equilibration runs to avoid the introduction of a bias in the configurations extracted. In addition, the possibility to simulate external conditions offers a way to better model the morphology of the system. In the case of disordered morphologies for example, preparatory runs at higher temperature and constant pressure are useful in injecting a sufficient degree of disorder into the system.

After all preparation runs and equilibration are performed, longer simulations can be run for data production. By virtue of the the ergodic hypothesis the trajectories resulting from these simulations offer a sampling of the configuration space from which the morphology can be investigated and macroscopic properties estimated.

### **2.9.3 Simulation of the ordered phase: a combined Monte Carlo and DFT approach**

Very often, scant structural information about all the relevant crystal polymorphs (i.e. that can be populated in experimental conditions) of an organic compound is available from experimental characterisation. Therefore, the modelling of the ordered phase should consist

in a two-step procedure that combines a guess of the possible crystal structures and a subsequent refinement procedure based on periodic DFT calculations<sup>[136]</sup>. The theory behind periodic calculations consists in a rather straightforward extension to periodic systems of the methods described above and will not be presented in detail here.

It is more interesting, instead, to focus on the initial guess of the possible structures. A structure is determined by the unit cell parameters (sizes and angles) and by the positions and orientation of the molecules in the asymmetric unit. Given the number of degrees of freedom, the configurational space can be quite large and the problem of finding the most relevant structures coincides with a search for all the relevant minima of a rugged multidimensional energy landscape. Many approaches have been proposed to efficiently solve this problem. Among them Monte Carlo methods stand out for their efficiency and simplicity.

In general a Monte Carlo method is any method that exploits randomly generated numbers to solve a problem. In this particular situation, a MC method can be applied to perform an heuristic optimisation procedure and –hopefully– extract all minima with the largest probability of being populated.

The starting point is to set up an *importance sampling* of the configuration space. This is done by generating sequences of configurations (with no dynamical meaning), called Markov chains<sup>[137]</sup>, according to the following rule:

$$p(\Gamma_a, n+1) = p(\Gamma_a, n) + \sum [k(\Gamma_f, \Gamma_a)p(\Gamma_f, n) - k(\Gamma_f, \Gamma_a)p(\Gamma_a, n)] \quad (2.33)$$

whose meaning is rather easy to understand, the probability  $p$  to populate the configuration  $\Gamma_a$  at step  $n+1$  in the sequence is given by the probability at step  $n$  plus the sum over all the incoming contributions from other states minus the sum over all contributions relating to the possibility of leaving  $\Gamma_a$  for another state  $\Gamma_f$ . Assuming **equilibrium** the detailed balance relation should hold

$$k(\Gamma_f, \Gamma_a)p(\Gamma_f) = k(\Gamma_a, \Gamma_f)p(\Gamma_a) \quad (2.34)$$

the choice of  $k(\Gamma_f, \Gamma_a)$  as, first proposed by Metropolis *et al.*<sup>[138]</sup>,

$$k(\Gamma_a, \Gamma_f) = \min \left( 1, \frac{p(\Gamma_f)}{p(\Gamma_a)} \right) \quad (2.35)$$

ensures that the sequences will provide a sampling of configurations compatible with the system energy landscape at equilibrium.

When dealing with molecular systems the relevant probability distribution is the one corresponding to Boltzmann statistics, that holds for the canonical ensemble, realised when a system is in equilibrium with a heat reservoir at temperature  $T$ . The probability distribution can be written as

$$p(\Gamma_a) = \frac{e^{-\frac{E(\Gamma_a)}{k_B T}}}{\sum_{\Gamma \in \text{conf}} e^{-\frac{E(\Gamma)}{k_B T}}} \quad (2.36)$$

and the choice of rates between configurations becomes

$$k(\Gamma_a, \Gamma_f) = \begin{cases} \exp\left(-\frac{E(\Gamma_f) - E(\Gamma_a)}{k_B T}\right) & E(\Gamma_f) > E(\Gamma_a) \\ 1 & E(\Gamma_f) \leq E(\Gamma_a) \end{cases} \quad (2.37)$$

Hence, the algorithm proceeds as follows: starting from an initial configuration a new one will be proposed according to some criteria that depend on the extraction of a random number. Then, the decision to accept or reject the configuration will be done according to the expressions in Eq. 2.37. If the energy is lowered, then the configuration is always accepted, if the energy is higher a random number  $x_{\text{rand}}$  is extracted and the decision will be based on

$$\text{if } x_{\text{rand}} \in \left[ \exp\left(\frac{-\Delta E}{k_b T}\right), 1 \right) \text{ move is rejected} \quad (2.38)$$

$$\text{if } x_{\text{rand}} \in \left[ 0, \exp\left(\frac{-\Delta E}{k_b T}\right) \right) \text{ move is accepted}$$

In the case of the minimisation procedure, temperature can be exploited as an external parameter with no physical meaning. This is the basis for **simulated annealing**<sup>139</sup>, for which temperature is initially set to a large value to make the acceptance of unfavourable configurations more probable and better explore the configurational space; as the sequence grows, temperature is lowered so that a more refined sampling of the minima across the landscape can be achieved.

Prediction of polymorphs follows the procedure outlined above. Molecular geometry from first-principles calculations is given as input and a force field to estimate the energy of a configuration is chosen, complemented with atomic charges from higher-level calculations. The input is used to build a set of crystal structures by applying the transformations of the

most probable space groups among organic compounds<sup>[140][141]</sup>. Once the set of possible structures is constructed, for each unit cell trial moves are proposed by varying the lattice parameters and reorienting and translating the molecules, kept rigid, in the asymmetric units. The trial move then goes through the acceptance/rejection step using the force field evaluated energy in the decision step.

This sequence is repeated and at the same time the non-physical temperature is lowered to refine the sampling of regions corresponding to minima. When simulated annealing is completed for all structures, they are considered to be optimised (i.e. to provide a sufficient sampling of the energy landscape). At this point the final structures are clustered according to the similarity of their radial distribution functions and only structures with distinct properties are retained. A final ranking is built by comparing the force field energy estimates and their density.

In the end the procedure has produced the required crystal structures. As detailed above, these structures can be further refined through periodic DFT and an improved ranking based on first-principles energy evaluations is established.

A complete picture of the possible ordered morphologies is thus finally drawn that can be used as input for further analysis. As a last remark, one should note that this procedure completely neglects the entropic contribution in the ranking of the structures that is rather estimated in terms of the enthalpic contribution alone.

## 2.10 Coupling length scales: charge transport

Among the properties relevant to assess photovoltaic performance, charge transport is of particular importance and deserves to be treated separately due to its peculiar character. By definition, charge transport occurs across the typical length scale of the device, thus linking the molecular scale, that dominates in charge carrier transfers, to the carrier trajectory from production to collection in the electrode<sup>[89]</sup>. This trajectory is usually of the same order of the typical thickness of thin films employed as active layer, that of the order of the  $\mu\text{m}$ . The efficiency of the transport process is at the basis of the large performances of inorganic semiconductors and perovskite solar cells and it is one of the limiting properties for organic materials. The physical quantity that quantifies this transport efficiency is **charge**

mobility<sup>[15]</sup>, that can be defined as follows

$$\mu = \frac{\langle v_{\text{carrier}} \rangle}{|\vec{\mathbf{E}}_{\text{field}}|}. \quad (2.39)$$

In this formula, mobility is given by the ratio between the average velocity of the charge carrier along its trajectory  $\langle v_{\text{carrier}} \rangle$  over the intensity of the applied electric field between the electrodes. Here, the dynamics is assumed to be dominated by the drift caused by the applied electric field so that mobility estimates the efficiency at which transport happens in a given material per unit of applied field. It is straightforward to see how this quantity can be used to compare the performances of different materials.

A number of experimental techniques exist that provide direct information on the mobility of semiconductors, some of them suited, in particular, for organic materials<sup>[142]</sup>. Among these, one of the most widespread is the measurement of the  $J$ - $V$  curve of a pure layer of organic semiconductor in a particular device arrangement in which only the injection of one type of carrier is permitted by the arrangement of energy levels between semiconductor and electrodes. In this arrangement, most materials exhibit a current called ‘space charge limited current’. When current flows in the device under no irradiation, a lot of carriers, either holes or electrons, are injected in the layer. The ability of the material to transport the injected carriers naturally depends on its mobility  $\mu$ . The SCLC<sup>[143]</sup> method requires the measurement of the  $J$ - $V$  characteristics and a fit. The fit is performed according to the law describing the saturation current characterising the process, the Mott-Gurney law<sup>[144]</sup>:

$$J = \frac{9}{8} \epsilon_0 \epsilon_r \mu \frac{V^2}{L^3} \quad (2.40)$$

where  $V$  is the applied potential,  $L$  the thickness of the layer and  $\epsilon_0 \epsilon_r$  the dielectric permittivity of the organic material. This law is easily understood as a flow of the injected charges within a capacitor-like layer by noting that the factor  $\mu \frac{V}{L}$  is the velocity of charges while the other part can be seen as the charge accumulated by a capacitor  $Q \propto CV$ , hence the quadratic dependence on voltage. The typical voltage applied are in the range between 0.1 to 10 V in layers 150 to 200 nm thick, yielding external field intensities in the material  $10^5$ - $10^7$  V/m. A value of  $10^6$  V/m has been considered in the applications presented here.

A brief overview of one of the most widespread framework available to describe charge transfer (i.e. electron transfer) will be given in the following together with the approach employed to predict mobility. A deeper knowledge of the theoretical details will clarify how

mobility links together all length scales. This framework will assume prior knowledge about electronic structure and morphology and will therefore constitute the third and final layer of the modelling approach to organic materials used within this work.

### 2.10.1 Marcus theory for charge transfer

Given the quantum nature of electrons, electron transfer is in general a rather complex phenomenon to describe. However, some conditions that hold true for most organic solids, i.e. limited local order, thermal agitation and localisation of charges, allow the description of electron transfer in terms of discrete hops between neighbouring molecules<sup>[35]</sup>, or molecular fragments in the case of polymers, across which the electronic density tends to be strongly localised. In this picture, it is possible to derive an expression for the rates of exchange for each molecular site in a given morphology<sup>[7]</sup>. The hopping of a charge between two molecules can be interpreted as a chemical reaction



A series of further assumptions are needed in order to set up the framework in which to derive the analytic expression for the rates. Together with high temperature and localisation of the charges on single molecular sites, electron transfer is assumed to be much faster than nuclear dynamics in the system, so that the Condon approximation can be applied. In addition, it is assumed that the pair of exchanging molecules has an interaction term that can be treated as a perturbation of the single molecule Hamiltonian, i.e. the electronic coupling is small.

In this framework, it is possible to identify two major players, the electron involved in the exchange and the surrounding environment. The latter corresponds to the nuclear configurations of the molecules involved in the exchange but also more in general, to all other molecules in the system that will respond to the exchange. For simplicity, the surrounding environment can be described through a collective reaction coordinate  $Q$  indicating its state. In general, the system is set in a isobaric-isothermal ensemble so that the relevant thermodynamic potential to follow in order to describe the transfer reaction is Gibbs free energy  $G$ . For a thermodynamic state  $G$  can be written as the sum of three contributions  $G = U + PV - TS$ . For a process like the one being discussed, the  $PV$  and  $TS$  terms will be negligible and only the variation of internal energy between the initial and final state will be relevant. These

states are associated with two energy surfaces with values over the system configuration space. The collective reaction coordinate can be considered as mono-dimensional for the sake of simplicity, and the initial and final energy surface to be two parabolas horizontally and vertically shifted between each other. Despite the simplicity, this model is able to capture the process with reasonable accuracy for most cases of interest and will lead to the derivation of the rate describing electron transfer.

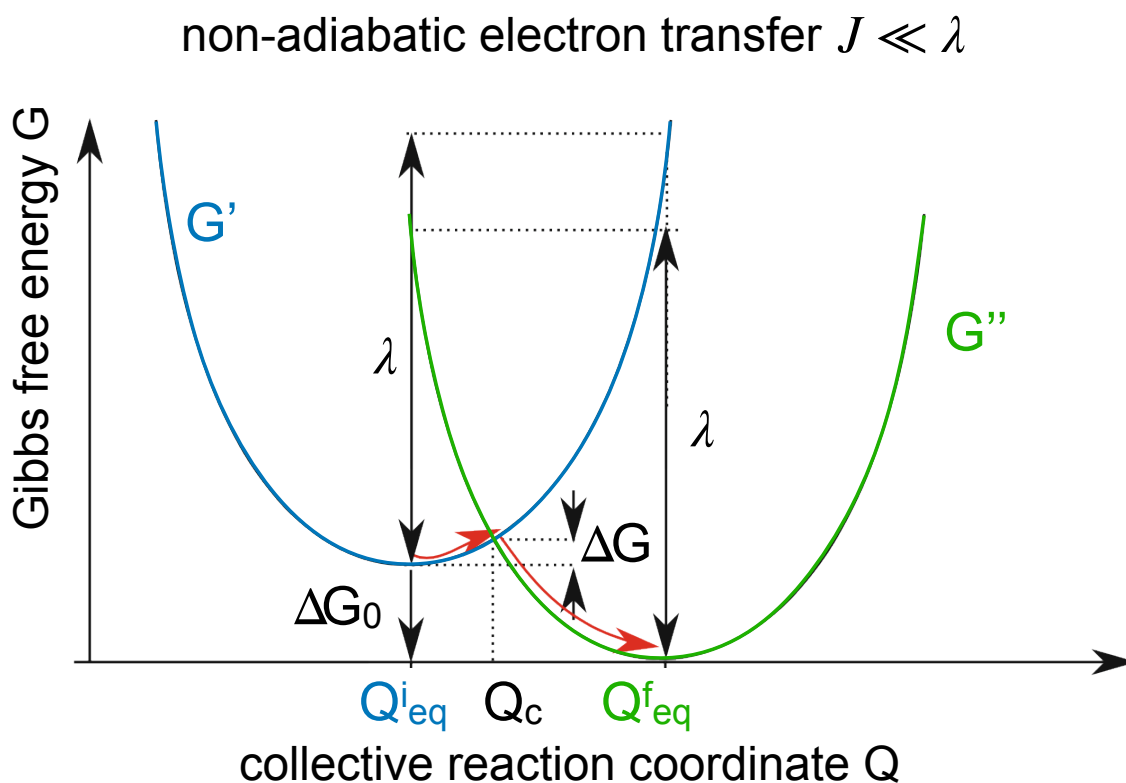


Figure 2.2: Depiction of the energy surfaces responsible for the “hopping” in the non-adiabatic regime of charge transfer. The interaction between the two states, i.e. the two molecules, is assumed sufficiently small as to leave the energy surfaces unchanged. *Red arrows* indicate the oscillations needed for the transfer between the two equilibrium positions. The transition can only happen at  $Q_c$  since the energy cannot change (the energy value is fixed) and the Frank-Condon approximation imposes that the nuclear configurations are the same ( $Q$  value is fixed).

The minima  $Q$  configurations of the energy surfaces are different in the initial and final state, namely  $Q_{\text{eq}}^i \neq Q_{\text{eq}}^f$  represent the two equilibrium configurations of the polarisable environment before and after the exchange, see Fig. 2.2. The two energy surfaces cross at a point where the reaction coordinate is indicated as  $Q = Q_c$ . By virtue of the Condon principle<sup>[145]</sup>,

the nuclear configuration should be the same for the transition to occur and moreover, due to energy conservation the transition cannot happen horizontally and can only take place at the intersection between the surfaces. The neighbourhood of the minimum  $Q_{\text{eq}}^i$  can be populated by the system due to thermal oscillations around its equilibrium point.

It is possible to derive explicitly an estimate for the quantity  $\Delta G$  that is the energy difference that should be provided by thermal agitation to reach the point where the surfaces cross. The explicit functional forms of the two parabolas under the assumptions above is:

$$\begin{aligned} G'(Q) &= \frac{k}{2}(Q - Q_{\text{eq}}^i)^2 + \Delta G_0 \\ G''(Q) &= \frac{k}{2}(Q - Q_{\text{eq}}^f)^2 \end{aligned} \quad (2.41)$$

$$\text{where } \Delta G_0 = G''(Q_{\text{eq}}^f) - G'(Q_{\text{eq}}^i)$$

$\Delta G_0$  is the energy difference between the minima of the two configurations of the environment and represents, geometrically, the vertical shift between the two functions. With some simple algebra one can express the energy difference between the initial minimum and the crossing as

$$\begin{aligned} \Delta G &= G'(Q_c) - G'(Q_{\text{eq}}^i) = \frac{k}{2}(Q_c - Q_{\text{eq}}^i)^2 + \Delta G_0 - \Delta G_0 = \\ &= \frac{k}{2} \left( \frac{Q_{\text{eq}}^i + Q_{\text{eq}}^f}{2} + \frac{\Delta G_0}{k(Q_{\text{eq}}^f - Q_{\text{eq}}^i)} - Q_{\text{eq}}^i \right)^2 \end{aligned} \quad (2.42)$$

Defining  $\lambda = \frac{k}{2}(Q_{\text{eq}}^i - Q_{\text{eq}}^f)^2$  the above expression becomes more compact and reads

$$\Delta G = \frac{(\Delta G_0 + \lambda)^2}{4\lambda} \quad (2.43)$$

$\lambda$  can be interpreted as the excess energy of the system on the initial surface relative to the final energy minimum in  $Q_{\text{eq}}^f$  and is called *reorganisation energy*. Considering that the nuclear configuration collectively expressed through  $Q$  obeys Boltzmann statistics, the probability to find  $Q$  at  $Q_c$  is

$$p(Q_c) = \exp\left(-\frac{\Delta G}{k_B T}\right) = \exp\left(-\frac{(\Delta G_0 + \lambda)^2}{4\lambda k_B T}\right) \quad (2.44)$$

At the same time, the rate of the electron transfer is given by Fermi's golden rule

$$p(e^- \text{ exchange}) = \frac{2\pi}{\hbar} |J_{12}|^2 \quad (2.45)$$

Combining the above Eq.s and considering an additional factor dependent on vibration (Franck-Condon factor)  $\frac{1}{\sqrt{4\pi\lambda k_B T}}$  the expression for the electron transfer between mol<sub>1</sub> and mol<sub>2</sub> can be finally obtained

$$k_{12} = \frac{|J_{12}|^2}{\hbar} \sqrt{\frac{\pi}{\lambda k_B T}} \exp\left(-\frac{(\Delta G_0 + \lambda)^2}{4\lambda k_B T}\right) \quad (2.46)$$

Electronic coupling  $|J_{12}|^2$  is the probability for the transition between two frontier orbitals of the exchanging pair. It represents how likely this transfer is when mediated by the weak interaction between the two molecules, treated as a perturbation  $\hat{H}_{\text{int. mol}_1\text{mol}_2}$ . At this point, using the amorphous or crystalline morphology predicted it is possible to compute rate lists for the molecules in the simulated morphologies. For amorphous configurations all sites will have, in general, a different environment and the number of rates to compute will be very large. Ordered configurations can again take advantage of the symmetry encoded in their structure by the space group and will thus have a much smaller number of rates that will be repeated over the crystalline structure<sup>[15]</sup>.

The calculation of electronic couplings deserves to be looked at in further detail. The approach discussed up to this point offers a picture in which carrier dynamics can be modelled as a sequence of exchanges between molecular pairs with configurations dictated by the morphology. The trajectory of a carrier corresponds to jumps between neighbouring sites for which polarisation of the surrounding medium – i.e. of the local assembly of molecules – is assumed to be negligible together with the electrostatic influence a distribution of carriers.

These conditions can be combined with the “frozen orbital” approximation that assumes the frontier orbitals of the exchanging dimer to emerge from the interaction of the frontier orbitals of the molecules. A model can thus be built on a vector space only spanned by the frontier orbitals  $\{\phi_1^{\text{FO}}, \phi_2^{\text{FO}}\}$  of the molecular sites. The effective hamiltonian employed reads:

$$\hat{H} = \sum_m \epsilon_m \hat{a}_m^\dagger \hat{a}_m + \sum_{m \neq n} (J_{mn} \hat{a}_m^\dagger \hat{a}_n + J_{nm} \hat{a}_n^\dagger \hat{a}_m) \quad (2.47)$$

where  $m, n$  run over the sites 1 and 2 in the dimer. The  $\hat{a}_i$  and  $\hat{a}_i^\dagger$  operators describe states localised over a site. The energy of the state associated with each site is  $\epsilon_i$ . Thanks to symmetry, in an ideal crystal lattice all sites are equivalent and thus all site energies are

the same. The  $J_{ij}$  are the electronic couplings that describe the process of destruction of the carrier at one site and its creation at another, i.e. the carrier exchange. It is important to remark that this model greatly simplifies the quantities involved. Indeed, in a rigorous approach, the electronic coupling should be given by:

$$J_{12} = \langle \varphi_1 | \hat{H}_{\text{dimer}} | \varphi_2 \rangle \quad (2.48)$$

where  $\varphi_{1,2}$  are the many-body electronic wavefunctions localised on the single sites. While here the expression is reduced to:

$$J_{12} = \langle \varphi_1^{\text{FO}} | \hat{H} | \varphi_2^{\text{FO}} \rangle \quad (2.49)$$

where FO stands for “frontier orbital”, LUMO for electron exchange or HOMO for the exchange of the hole and thus only involves singly-occupied orbitals obtained from HF, semi-empirical or DFT calculations. The solution to the system, i.e. energy levels of the dimer, is provided by this generalised secular equation:

$$(\mathbf{H} - E \mathbf{S}) \mathbf{C} = 0 \quad (2.50)$$

that can be recast in the form of secular equation according to a transformation involving the  $\mathbf{S}$  (see ref. [146](#)) the overlap matrix between  $\varphi_1^{\text{FO}}$  and  $\varphi_2^{\text{FO}}$ . The transformation is necessary in the general case in which  $\langle \varphi_1^{\text{FO}} | \varphi_2^{\text{FO}} \rangle \neq 0$ . When this happens the parameters need to be corrected to obtain the right values of electronic couplings and site energies [146](#).  $J_{12} = \langle \varphi_1^{\text{FO}} | \hat{H} | \varphi_2^{\text{FO}} \rangle$  can be evaluated through a projective method, in which the knowledge of dimer eigenstates is exploited according to:

$$J_{12} = \langle \varphi_1^{\text{FO}} | \sum_{k_a} |\psi_{k_a}\rangle \langle \psi_{k_a}| \hat{H} \sum_{k_b} |\psi_{k_b}\rangle \langle \psi_{k_b}| \varphi_2^{\text{FO}} \rangle \quad (2.51)$$

This projective formula contains all the information that needs to be provided from quantum-chemical calculations, in particular:

$$J_{12} = \sum_k \gamma_1^k \mathcal{E}_k \gamma_2^k \quad (2.52)$$

where  $\gamma_1^k$ ,  $\gamma_2^k$  are the projection of the initial and final states over the eigenstates of the dimer, while  $\mathcal{E}_k$  represents the  $k$ -th diagonal entry of the dimer matrix.

Thanks to this last formula it is finally possible to evaluate the transfer integrals. The procedure adopted for the calculations reported in this thesis work, has been largely based on the one reported in ref. [\[146\]](#), electronic structure calculations are performed with the semi-empirical INDO method in the Zerner spectroscopic parameterisation. Three separate calculations are carried out on the charged site, on the dimer and on the receiving site. The basis set is kept fixed and the dimer basis set is built as the direct sum of the separate basis sets of the site,  $\{\chi_{\text{dim}}\} = \{\chi_{\text{site 1}} \oplus \chi_{\text{site 2}}\}$ . The basis set being the same means that atomic orbitals are identical but shifted over the coordinates of the sites. The particular choice of the basis set implies that the overlap matrix  $\mathbf{S}$  deviates very little from the unit matrix and the determination of  $J_{12}$  and  $\epsilon$  can be directly done via the projection of  $\phi_1^{\text{FO}}$  and  $\phi_2^{\text{FO}}$  on the dimer eigenstates and summing the product of this projections weighted by the energy eigenvalues of the dimer to estimate  $J_{12}$ .

## 2.10.2 Kinetic Monte Carlo

The final step to fully exploit microscopic data from the rates and morphology is to model the dynamics of the charge carriers within the material. While several methods could be used to describe accurately this dynamics, it is very convenient to resort once again to Monte Carlo based methods. This time though, the solution provided by the method will not be used for the sampling of configurations but for the explicit solution of the dynamics and the generation of time dependent trajectories. These will then serve to estimate the physical quantities required to compute mobility (i.e. average transport velocity of a carrier  $\langle v \rangle$ ).

In this case, since the quantities of interest are dynamical *kinetic Monte Carlo* methods [\[147\]](#) are employed. They are based on the idea that typical systems encountered in physical chemistry will evolve in a landscape with many competing minima, or rugged energy landscapes, as typical for crystalline polymorphs, for instance. These minima can be pictured as wells on the potential energy surface and the dynamics of the system can be clearly distinguished between a dynamics happening inside the wells and another concerned with the crossing between wells.

In many cases the crossing dynamics is more interesting than the in-well dynamics. In principle, approaches like MD should be able to produce an accurate description of this dynamics.

However, the typical time step employed is constrained by the requirement that all relevant nuclear degrees of freedom have to be described. This usually limits the maximum time-step at the femtosecond range. If crossing between wells happens on a much larger time scale, as it is usually the case, a lot of the computational effort will be spent to describe essentially uninteresting dynamics. The goal of kinetic Monte Carlo is to overcome this *time-scale problem*<sup>[147]</sup> and probe the relevant times for the system modelled. In this view, the problem can be recast in terms of a hopping dynamics between a set of possible wells, or states, a form that perfectly fits the description provided by Marcus theory for charge transfer. For most systems, the dynamics within the initial state is such that memory of how the system entered the state can be assumed to be lost. Under this condition escape probability is a constant. In this approximation, the probability for a system to be found in the state at time  $t$  is given by

$$p_{\text{in}}(t) = \exp(-k_{\text{escape}} t) \quad (2.53)$$

consequently the cumulative probability of having escaped in the time interval  $(0, t)$  is given by

$$p_{\text{out}}^{\text{tot}}(t) = 1 - \exp(-k_{\text{escape}} t) \quad (2.54)$$

The derivative over time of this quantity gives the instantaneous escape probability

$$p_{\text{out}} = k_{\text{escape}} \exp(-k_{\text{escape}} t) \quad (2.55)$$

which also corresponds to the probability distribution of escaping times.

The most generic process will have a number of possible escape pathways. Taking the system to be in state  $i$  and labelling the other possible states with  $j$  one gets a probability distribution of escape times from  $i$  to all states  $j$  and an average escape time  $\tau$

$$\begin{aligned} k_{\text{escape from } i} &= \sum k_{ij} & p_j(t) &= k_{ij} \exp(-k_{ij} t) \\ \tau &= \int_0^\infty dt t \sum k_{ij} \exp(-\sum k_{ij} t) \end{aligned} \quad (2.56)$$

At this point, laying out an algorithm to simulate this dynamics is a simple procedure. The most convenient scheme can achieve time propagation of one step with the extraction of just two random numbers. A segment with the total length of  $k_{\text{escape from } i}$  can be built by taking the cumulative sum over the  $k_{ij}$  rates. The total segment has small domains of variable size

corresponding to the values of the rates in some particular units used for the simulation. A first random number  $x'_{\text{rand}}$  is drawn from a uniform distribution between 0 and 1. The number is multiplied by the total escape rate  $x'_{\text{rand}}k_{\text{escape from } i}$  and depending on which domain of the segment the value falls in, that pathway will be chosen and the system will be evolved to that state. Finally, in order to determine the time step of this evolution, which is non uniform by virtue of the discussion above, another random number  $x''_{\text{rand}}$  is extracted and transformed to produce an escape time using the total distribution of escape times for the initial state

$$t_{\text{escape}} = -\frac{\log(x''_{\text{rand}})}{k_{\text{escape from } i}}. \quad (2.57)$$

This algorithm can be employed in the prediction of mobility provided a few connections are clarified. Morphologies are considered as lattices, that might be crystalline or disordered. When a charge is injected, it evolves according to the hopping dynamics described by Marcus rates, usually in the presence of an electric field between the electrodes. This electric field will contribute to the dynamics by entering into the term  $\Delta G_0$  in Eq. [2.46](#), together with other contributions, like the differences in site energies in amorphous configurations.

Each site-to-site transfers of the charge is recorded and the process is repeated until the simulation time is “large enough” to consider the simulation converged.

The sequence of charge transfers will define a trajectory that, combined with the geometrical information of morphology allows the evaluation of carrier velocity. It has already been remarked that the two morphologies will present different problems. Due to the variability in local environment in amorphous configuration for example, the number of rates needed to perform the simulation will be very large and the variability will also reflect on the electronic coupling  $J_{12}$  and rates. Couplings typically decrease exponentially as a function of distance and the range of variability of rates will mirror the range of local environments. Many trajectories in the amorphous media could consist in carriers trapped within small clusters of molecules. This situation is made worse by the limited accessible size of this simulated morphologies and the use of periodic boundary conditions that introduce a bias in the modelling of the amorphous. These problems can be attenuated by considering many configurations extracted from the MD trajectory and by repeatedly simulating the injection and the dynamics over the same configuration many times, changing the site on which the charge is injected. Crystal structures on the other hand, will have a small variability of the rates, but in the

case of large exchange rate the prevalence of certain processes with low energy barrier will translate in very small evolutions steps limiting the accessible simulated time.

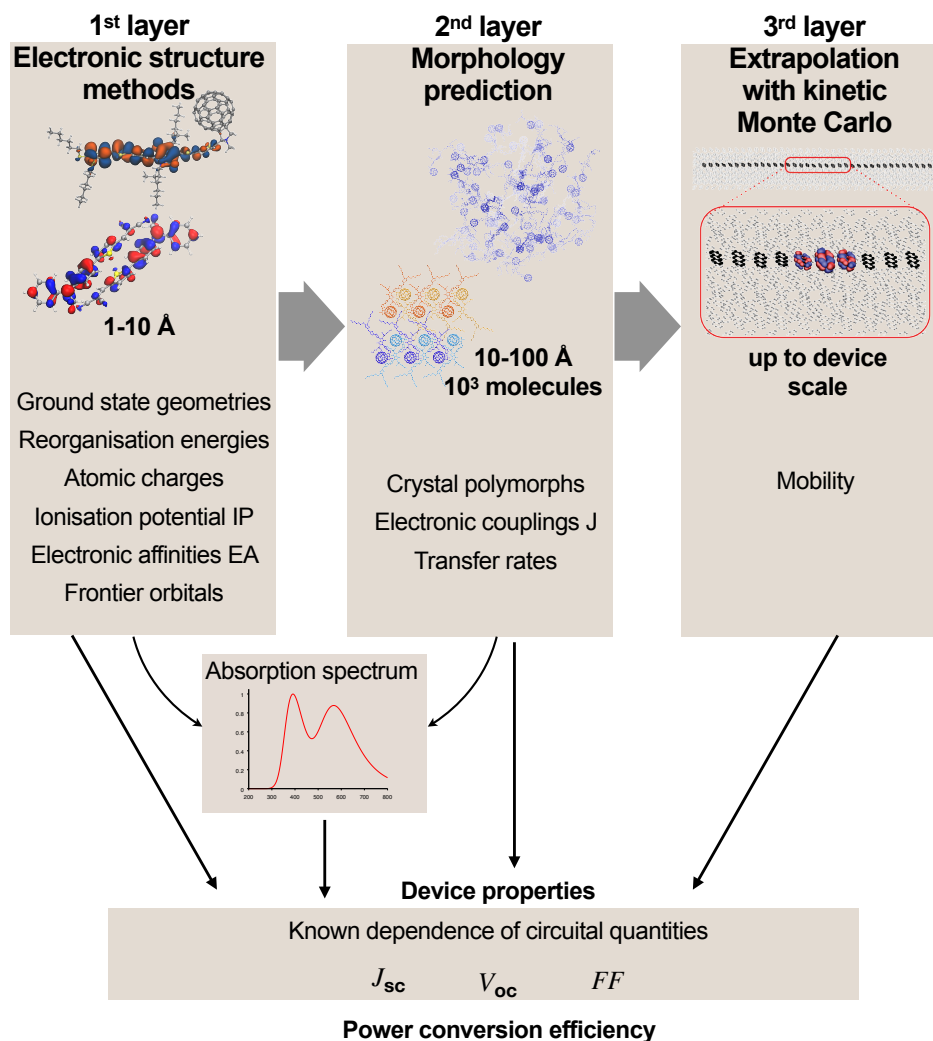


Figure 2.3: Scheme summarising the adopted protocol. Electronic structure methods are employed to generate accurate information on the orbital energies, geometries and charge distributions of the molecules, this is the first layer of computational methods employed. The next layer combines the information coming from the previous one (atomic charges, geometry, ...) to compute the most plausible packings of molecular assemblies, ordered or disordered, on the basis of electrostatic and dispersion interactions. This information can be used to refine electronic structure calculations by including details about the local molecular environment (absorption spectra) and can be also passed to the third layer. Kinetic Monte Carlo methods are used to extrapolate the information generated in the second layer and simulate processes happening at larger scales (charge transport). All data from the three layers can be used to give a general assessment of photovoltaic performance. A preliminary assessment can be given based on the estimates of relevant quantities: HOMO and LUMO, absorption spectrum, charge mobility. Quantitative assessment can also be foreseen by using the empirical relations that have been derived to link these quantities to the circuital quantities characterising a solar device,  $J_{sc}$ ,  $V_{oc}$  and  $FF$  and ultimately give an estimate of the PCE.

# Chapter 3

## The case of a small-molecule donor

As a first example of the methodology discussed in the previous chapter, in the following, the study of an interesting molecular system based on small-molecule donor is presented.

Together with non-fullerene acceptors<sup>[62,63]</sup>, small molecular materials are among the trending topics in current organic photovoltaics research. The designation of “small-molecule donor” has emerged in opposition to polymeric donors that, in the early days, were extensively investigated in solar cells devices. The initial predominance of polymeric materials is also the reason why organic photovoltaic devices are often referred to as “plastic photovoltaics”. The remarkable research effort around photovoltaic polymers continues to this day and has been capable of progressively increase the PCE up to remarkable values between 10 % and 12 %<sup>[148,149,150]</sup>. This has been achieved through the refinement of deposition techniques, the amelioration of morphology control and can also be attributed, to a large degree, to the trial-and-error strategy applied to the engineering of growingly complex monomeric units<sup>[151]</sup>. Despite the remarkable steps forward, the development of polymeric materials is somewhat emblematic of the woes affecting research in materials science. After an initial effort devoted to the investigation of novel materials in a variety of device architectures, the experimental side has somewhat shied away from a thorough rationalisation of the observed behaviour by the theoretical community. This has resulted in the generalisation of the above mentioned trial-and-error strategy, deprived of the invaluable input of modelling that is necessary in directing and optimising the research process. The effects of this are particularly evident in organic semiconductors where the chemical space is incredibly large and its map-

ping according to the properties relevant for applications, anything but straightforward. In part, this situation can be motivated by the fact that, in the early days, the status of computational approaches and the availability of computational resources was much less developed than now. In addition, polymeric materials represent rather complex systems to study and the rationalisation of their behaviour poses specific difficulties that are still, at present, not easy to overcome. This is why the rather crude indications of enhancing  $\pi$ -conjugation and improving self-organisation properties have always been considered sufficient theoretical inputs from molecular theory to guide the search for new materials.

Today the picture has dramatically changed, especially for what concerns computational methods and resources. The field has promptly responded as evidenced by the proliferation, in recent years, of works incorporating theoretical input of increasingly higher resolution. At the same time the domain has witnessed the growth of new experimental research lines more focused on providing data to tackle the open theoretical questions rather than chasing the uninformed enhancement of device performance.

This is exactly the setting in which small-molecule donors have been first approached. Small molecules have the advantage of shedding a few layers of complexity with respect to polymers<sup>51,58,152,153</sup>. For example, polymers often suffer from the reproducibility issue, i.e. it is difficult to reproduce devices based on the same material and matching already reported performances, while performances of devices based on small-molecule materials are highly reproducible<sup>52,152,153,154</sup> and also offer the possibility of directly link structure to the relevant properties, making the identification of “structure-property” relations much simpler.

The material presented in this chapter comes from one of these research lines, based on the simplification of molecular structures. Moreover, its remarkable behaviour is of particular interest *per se*, since it offers a conspicuous example of how supramolecular organisation and the presence of competing crystal polymorphs are able to affect fundamental properties like absorption and mobility.

The chapter is structured as follows. First, a presentation of the chemical system under investigation is given. Particular care is taken to stress the reported experimental behaviour and the characteristics that the protocol is expected to reproduce and describe microscopically. An outline of the computational details employed for the modelling follows this section. After that, the two final sections are devoted to the main results and a brief outline of the

conclusions that can be drawn from this analysis.

### 3.1 A small push-pull molecule

The compound is a small push-pull system consisting in a methyl-diphenylamine donor moiety linked to a dicyanovinyl acceptor group through a 2-5-thienyl spacer (MDTD)<sup>[155][156]</sup>. MDTD has been initially synthesised from another molecule, triphenylamine (TPA) already amply characterised as donor material in literature<sup>[156][157]</sup>. The synthesis of MDTD consists in the substitution of one of the external phenyl rings of TPA (in green in Fig. 3.1), linked to the nitrogen, with a methyl group. This substitution implies a reduced number of constraints on the other free phenyl ring and confers greater flexibility to the structure. The modification is based on a simplification criterion that has recently yielded some interesting results and that has produced materials with interesting properties going beyond the original field of photovoltaics<sup>[158]</sup>.

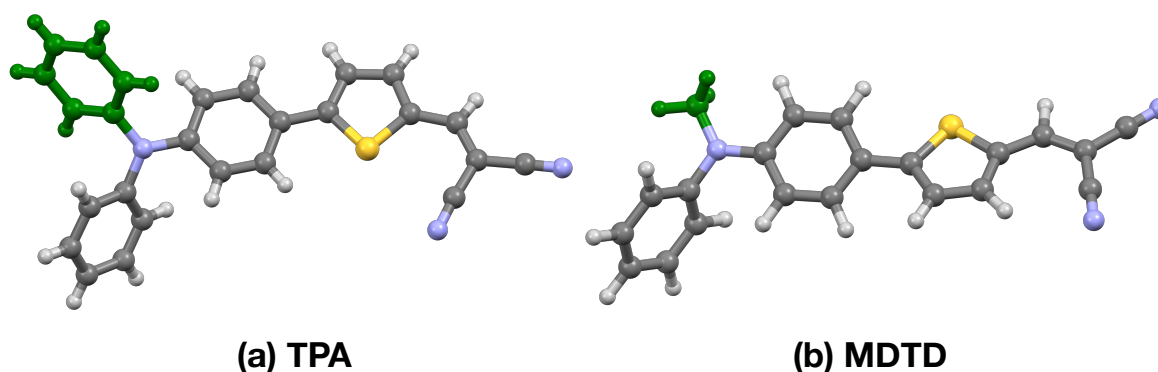


Figure 3.1: Molecular representations of TPA (*left*) and MDTD (*right*) with the residues involved in the substitution depicted in green.

To better understand the implications of this change, in ref.<sup>[156]</sup>, a comparison between the performance of MDTD and TPA is carried out. From this, clear evidence emerges on the importance of molecular structure in the determination of supramolecular order.

For material characterisation MDTD has been analysed in solid thin film conditions. Thin films are deposited either by spin-casting or vacuum evaporation and are later tested as donor layers in standard planar heterojunction solar devices, in combination with fullerenes. Upon

characterisation, a pronounced modification of the self-organisation of MDTD molecules can be inferred by comparing the shape of the absorption spectrum before and after performing a thermal treatment at 80° C<sup>[156]</sup>. The thin film spectrum undergoes a change in its shape characterised by a substantial redshift and a change in the absorption maxima structure, resulting in a final system with improved light-absorption properties and a better overlap with the solar spectrum. A behaviour not observed for equivalent TPA thin films. The goal is therefore to identify the microscopic atomistic details associated to this change in MDTD thin films through the modelling of the most thermodynamically relevant solid phases, i.e. that can be populated at ambient conditions, and the prediction of their absorption spectra. More specifically, on the basis of the results of the modelling, a microscopic description of the molecular packing responsible for the different optical response is proposed together with some hints on the thermodynamic characteristics of the possible mechanism responsible for this particular phenomenology.

The availability of good quality experimental data for charge mobility has also offered the possibility to corroborate the proposed explanation by comparing these data with predictions of mobility based on the microscopic predictions of morphology obtained from the absorption analysis.

## 3.2 Computational details

The simulation of the optical properties of a material in thin film conditions, requires to account for the effects of the molecular environment<sup>[159]</sup> on the electronic structure of single molecules. As abundantly discussed in the previous chapter, this requirement can be met via the application of a methodology able to predict with accuracy the supramolecular details having the strongest impact on electronic structure. The large majority of the thin films employed in solar cells active layers show a polycrystalline character where different regions with varying degree of order are simultaneously present<sup>[159][160][161]</sup>. The character of molecular stacking within these regions plays a major role in determining the efficiency of the material as active component in organic heterojunction solar cells. Moreover, as already pointed, if the material making up the thin film has more than one thermodynamically relevant crystal polymorph, distinct crystalline grains, or crystallites, featuring different crystal

phases may be present. At the same time, in the interfacial gaps between crystallites the material can be considered essentially amorphous. The strategy that has been presented in chapter 2, offers a straightforward solution to this problem. For this particular investigation the focus will be on the identification of the possible crystal packings, representative of the ordered domains of the thin film but also indicative of the local order that could emerge at smaller scale within amorphous regions. The explicit simulation of disordered morphologies has not been carried out due to the availability of theoretical data in the literature<sup>[162]</sup>.

A series of software packages implementing the strategy for morphology predictions have been employed. Polymorph prediction was carried out via the polymorph prediction module in Materials Studio. This module takes as input the geometry of the molecule obtained via a density functional theory (DFT) optimisation. This optimisation has been performed in Gaussian 16<sup>[163]</sup> at the B3LYP level<sup>[111][112]</sup> of theory in combination with Grimme's D3 correction to model dispersion forces and Pople's 6-311G(d,p) basis set<sup>[118][120]</sup>. From this geometry, the module builds a number of possible ordered structures based on the symmetry transformations of a set of space groups known to be the ones most frequently occurring among organic molecular crystals<sup>[140]</sup>. The structures produced are optimised according to the simulated annealing procedure outlined in chapter 2 to explore all energy minima. After each step, the energy is estimated via the classical DREIDING force-field<sup>[133]</sup> modified to include restricted electrostatic potential (RESP) charges<sup>[164]</sup> obtained at the same level of theory employed for the geometry optimisation. Following minimisation, the structures are clustered according to the similarity of their radial distribution functions and an energy ranking is defined, on the basis of the force-field. The lowest lying polymorphs are then extracted, and the ranking is refined through periodic density functional theory calculations. For each unit cell, geometric and atomic parameters are relaxed at the B3LYP-D3 level of theory in combination with an all-electron 6-31+G(d,p) basis set, modified for solid-state calculations performed in CRYSTAL17<sup>[136]</sup>.

The optimised unit cells for the relevant polymorphs are then used as input for the modelling of the crystal environment via the Ewald method<sup>[165]</sup>. According to this method, a supercell is first built starting from the unit cell. Three concentric regions are identified in the supercell from the geometric centre. The inner region is described at full quantum-mechanic level, in the second region molecules in the crystal structure are replaced by the corresponding

Mulliken charges for each atom in order to approximate the electrostatic potential determined by the crystal environment. In the third region the same task is carried out by a set of charges whose values have been fitted so as to reproduce the Madelung potential of the periodic structure<sup>[166]</sup>.

The complete distribution of charges of the second and third region is finally employed in conjunction with the quantum-chemical details of the first region for a series of vertical time-dependent density functional theory (TD-DFT) calculations performed in keeping with the previous geometry optimisation through Gaussian 16 at the same level of theory.

### 3.3 Main results

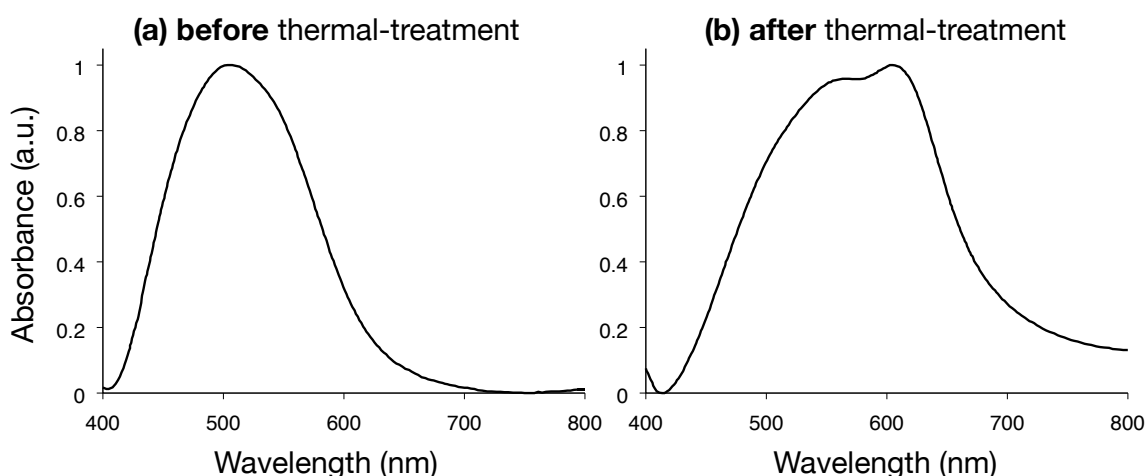


Figure 3.2: Experimentally measured absorption spectra for the thin film as-cast (*left*) and for the thin film after thermal treatment (*right*).

From the experimental studies in the literature, ref. <sup>[156]</sup>, the striking change in the absorption spectrum observed in thin film condition (see Fig. [3.2](#)) suggests the presence of at least two crystal polymorphs with markedly different stacking properties that are likely responsible for the pronounced change in absorption recorded<sup>[156]</sup>.

Polymorph prediction has been carried out for the system to identify the crystal structures possibly involved. The refined energy ranking of polymorphs obtained through the procedure, indicates the presence of two low-energy structures with a difference in their total

energies per molecule of 6.23 kcal/mol, see Table 3.1. This energy difference is significant, but it is reasonable to interpret it as an upper estimate of the actual difference in formation enthalpy of the two bulk structures with uncertainties coming from the systematic error of the procedure, the level of theory employed<sup>[167][168]</sup> and the possible variations in the energy landscape specifically associated with the thin film phase<sup>[169]</sup>.

The most stable polymorph (from here on, structure 1) belongs to the  $P\bar{1}$  space group. A comparison with the crystal phase reported experimentally (CCDC 1039019)<sup>[156]</sup>, reveals that they are very close and the procedure has correctly identified the lowest energy structure. For this reason, in the following analysis, the structure obtained from the full geometry relaxation via periodic DFT of the experimental structure reported in the crystal information file<sup>[156]</sup> has been considered.

The second polymorph (from here on, structure 2) identified belongs to the monoclinic  $P2_1/c$  space group. Molecules in this structure are arranged in pairs with the donor moiety of one molecule in close proximity to the acceptor moiety of the other (Fig. 3.3). This “head-to-tail” arrangement minimises dipole-dipole interactions. The main difference between the two structures lies precisely in the character of the stacking. Structure 1 has an approximate  $\pi$ - $\pi$  stacking in which molecules are simply shifted according to the relevant crystal axis, with the result that  $\pi$ -stacked pairs have molecules in which the axis going from donor to acceptor group is aligned in the same direction (Fig. 3.3). Structure 2 on the other hand, due to the larger number of transformations in the space group, allows  $\pi$ -stacked pairs to have opposing directions of the donor-acceptor axis. So that one molecule is rotated with respect to the other by 180 degrees around the axis perpendicular to the approximate conjugation plane of the compound (shown in blue in Fig. 3.3).

Polymorph	a	b	c	$\alpha$	$\beta$	$\gamma$	Space group	density	$\Delta E$
structure 1	5.65	7.99	17.00	82.61	84.39	90.25	$P\bar{1}$	1.494	0.00
structure 2	6.98	22.80	9.75	90.00	101.26	90.00	$P2_1/c$	1.488	6.23

Table 3.1: Computed cell parameters (a,b, c, Å,  $\alpha$ ,  $\beta$ ,  $\gamma$ , °), densities (D, g/cm<sup>3</sup>) and relative energies per molecule ( $\Delta E$ , kcal/mol) for the two crystal polymorphs (listed according to their relative stabilities, 1 being the most stable).

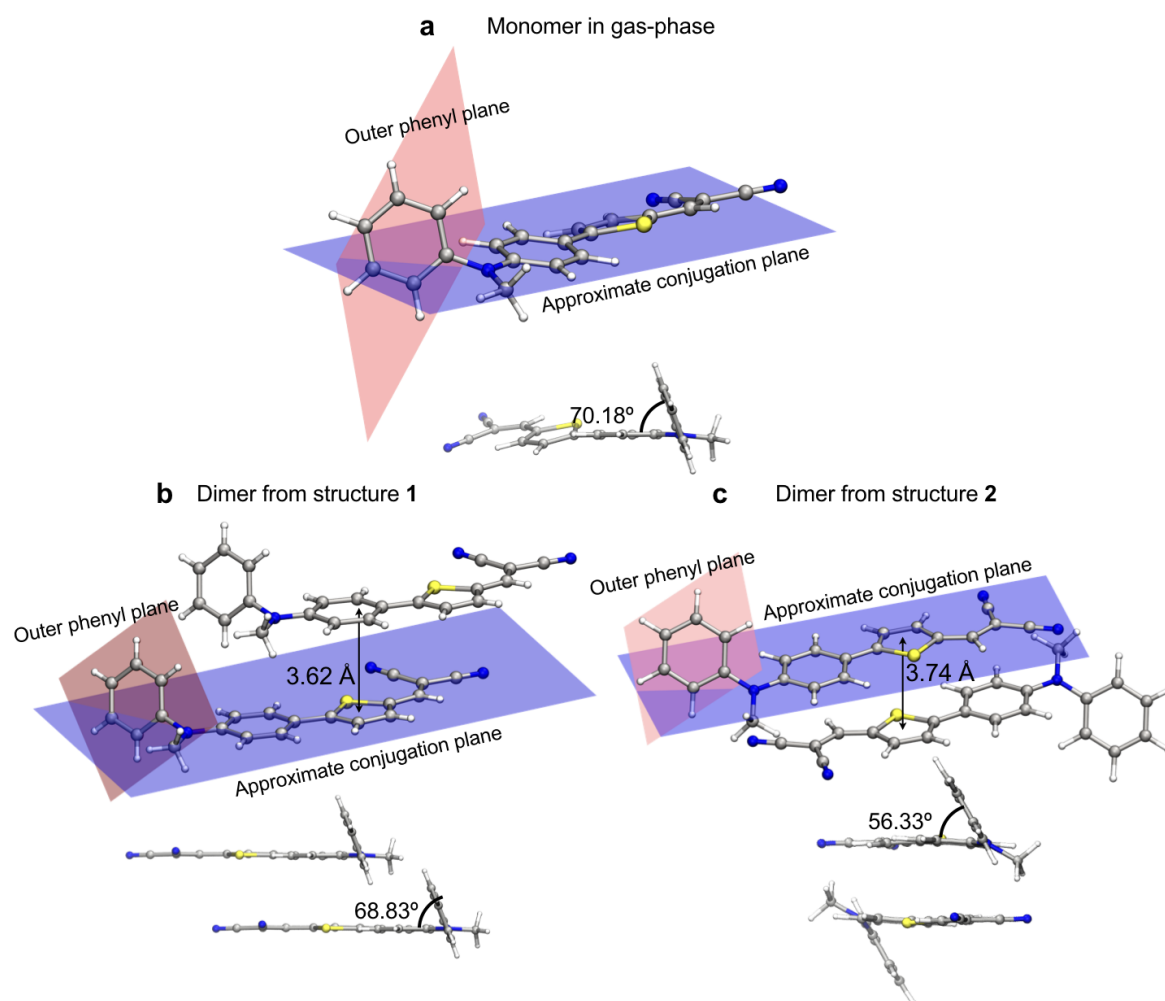


Figure 3.3: Molecular representation of the monomer geometry relaxed in gas phase a, and the dimers issued from structure 1 and structure 2, b & c. For each geometry the angle between the plane of the external phenyl ring and the conjugation plane is highlighted. All calculations have been performed at B3LYP/6-311+G(d,p) level of theory.

The difference in supramolecular organisation between crystal polymorphs may play a huge role in determining the absorption properties of a material. This is especially true in the case of MDTD, a push-pull system with a relatively large value of the dipole moment in gas phase (17.54 D) for which dipole-dipole interactions are major driver of self-organisation<sup>[170,171]</sup>. The fact that electrostatic interactions are so important, also justifies the choice of the Ewald procedure whose aim is precisely the modelling of the electrostatic molecular environment. Supramolecular organisation has two main effects on optical properties. The first is associated with changes in molecular geometry, the second, to the polarisable environment determined by the surrounding molecules<sup>[172,173]</sup>. The geometry effect can be accounted for

by performing spectral calculations on the molecular geometry found in the optimised unit cells of structure 1 and 2, i.e. by considering the molecular geometry in crystal phase. The second effect on the other hand, will be modelled via the Ewald embedding method. It is associated with the electrostatic environment and it is therefore dependent on aggregation details. Moreover, since the main difference between the two polymorphs lies in molecular stacking, it is reasonable to consider the molecular pair, the dimer, as the unit most relevant to the prediction of optical response.

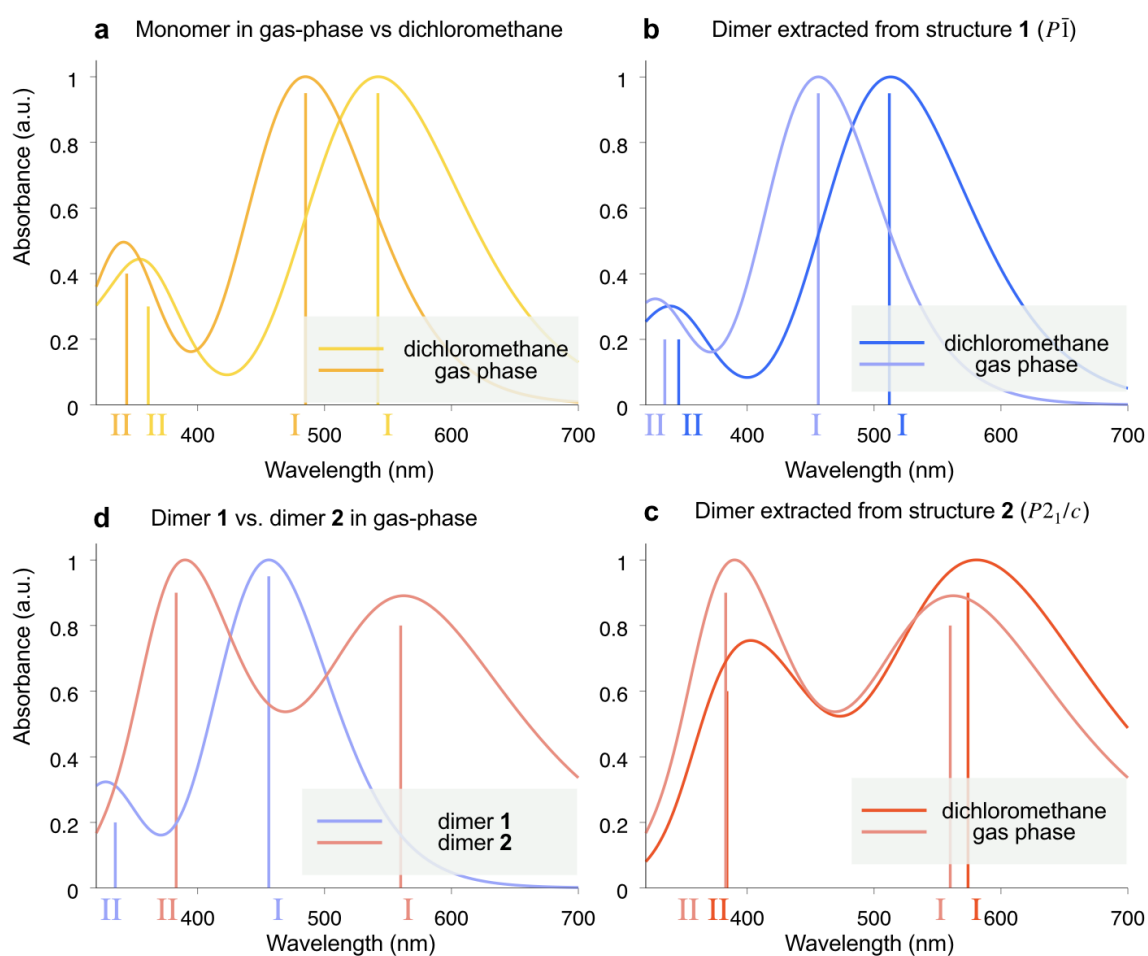


Figure 3.4: Predicted absorption spectra for a monomer in gas phase relaxed geometry in vacuum and in dichloromethane, b dimer with geometry extracted from structure 1 in vacuum and dichloromethane, c dimer with geometry extracted from structure 2 in vacuum and dichloromethane. d shows the comparison between the two dimers in vacuum. All calculations have been performed at B3LYP/6-311+G(d,p) level of theory, solvent when included is treated according to the polarisable continuum model (PCM)<sup>174</sup>. Spectra are normalised according to their maximum value.

Fig. 3.4 displays the predicted absorption spectra for the monomer in gas phase geometry

System	Transition I						Transition II					
	gas phase			dichloromethane			gas phase			dichloromethane		
	$\lambda$	$E$	$f$									
dimer 1	456	2.71	1.63	511.5	2.42	1.50	355	3.70	0.33	346	3.58	0.50
	HOMO-1 to LUMO		58 %	HOMO-1 to LUMO		40%	HOMO-2 to LUMO+1		54%	HOMO-3 to LUMO		48%
	HOMO to LUMO+1		41%	HOMO-1 to LUMO+1		34%	HOMO-3 to LUMO		15%	HOMO-2 to LUMO+1		40%
	HOMO to LUMO+1					28%	HOMO-3 to LUMO+1		30%			
	$D_{CT} = 5.93 \text{ \AA}$			$D_{CT} = 6.26 \text{ \AA}$			$D_{CT} = 2.14 \text{ \AA}$			$D_{CT} = 4.06 \text{ \AA}$		
dimer 2	560	2.21	0.95	574	2.17	1.30	383	3.24	0.86	384	3.23	0.70
	HOMO-1 to LUMO		70%	HOMO-1 to LUMO		74%	HOMO to LUMO+2		54 %	HOMO-3 to LUMO+1		72%
	HOMO to LUMO+1		28%	HOMO to LUMO+1		22%	HOMO-3 to LUMO+1		30 %	HOMO to LUMO+2		12%
							HOMO-2 to LUMO		12 %	HOMO-2 to LUMO		10%
monomer	485	2.56	0.93	542	2.29	1.05	344	3.60	0.43	359	3.45	0.42
	HOMO to LUMO		98%	HOMO to LUMO		98%	HOMO-1 to LUMO		82 %	HOMO-1 to LUMO		89%
							HOMO to LUMO+1		17 %	HOMO to LUMO+1		6%
	$D_{CT} = 6.70 \text{ \AA}$			$D_{CT} = 6.75 \text{ \AA}$			$D_{CT} = 3.67 \text{ \AA}$			$D_{CT} = 5.33 \text{ \AA}$		

Table 3.2: Data on the main transitions for gas phase and in solution (dichloromethane), predicted from spectral calculations at B3LYP/6-311+G(d,p) level of theory. For each transition the wavelength  $\lambda$  in nm, energy  $E$  in eV and oscillator strength  $f$  is reported. In addition, a list of the transitions between Kohn-Sham orbitals with the largest contribution is given together with the  $D_{CT}$ -index for all non-symmetrical structures (monomer and dimer 1).

and for the two dimers extracted from crystal structure 1 and 2. In Table 3.2, numerical data for the same transitions highlighted in the plots are presented. These transitions have the strongest oscillator strengths among all the predicted transitions. The other transitions falling in the relevant energy range will be considered in the following step of the investigation but will not be discussed in detail as the optical behaviour can be clearly deduced from the analysis of the main ones. Panel a shows the comparison of the monomer spectrum in gas phase and in presence of a polarisable medium, dichloromethane ( $\epsilon_r = 8.99$ ). The spectrum is redshifted while its shape is only slightly affected. The redshift is more important for transition I (HOMO to LUMO), shifted by 0.27 eV and less pronounced for the high-energy peak corresponding to transition II, 0.15 eV. Panels b and c show the combined effect of dimerisation in the two different crystal structures and allow a comparison between the effects of geometry alone (gas phase spectra) and geometry in combination with a polarisable medium. The dimer from structure 1 has a gas phase spectrum blue-shifted with respect to

the monomer. This is due to the parallel stacking of monomers in the pair resulting in an interaction term of molecular dipoles which increases the energy. The relative brightness of transitions is mostly unchanged by the presence of the solvent that gives, much like in the monomer's case, a redshift with respect to the gas phase spectrum with similar values (transition I, 0.29 eV, transition II, 0.12 eV). On the other hand, the behaviour of dimer 1 is significantly different. With respect to the monomer, the main transitions change in character and relative brightness. This time this effect can be attributed to the antiparallel stacking of molecular dipoles resulting in an interaction term lowering the overall energy. The interaction between the two molecules in the dimer is dominant and the dimer is less influenced by its environment. This is evident from the spectrum in dichloromethane that only experiences a negligible redshift in the low-energy peak (0.04 eV) and a change in the relative brightness of the main peaks (transition I, from 0.95 to 1.30, transition II, 0.86 to 0.70).

To better understand the reasons behind the different behaviours it is useful to analyse the geometrical features of the systems available in Fig. 3.3. In gas phase, the geometry of the monomer is approximately planar for the structure extending from the linked phenyl of the donor group to the acceptor group. In order to quantify the degree of planarity, the plane of the phenyl ring as approximate conjugation plane has been considered (shaded blue plane in Fig. 3.3). The average distance from this plane of all atoms except for the outer phenyl ring is 0.29 Å while the angle between the same plane and the plane (Fig. 3.3 in shaded red) of the outer phenyl ring is 70.18°.

In dimer 1 these parameters become 0.11 Å and 68.83° respectively, indicating that molecules in structure 1 become more planar due to intermolecular interactions. Dimer 2 on the other hand shows a degree of planarity similar to the gas phase monomer, with the average distance from the approximate conjugation plane being 0.31 Å but with a large change in the angle between the planes, which becomes 56.33°.

The data on the transitions offer additional insight. The main transitions of the monomer clearly show that the most relevant processes involve the transfer of the electronic density from the methyl-diphenylamine donor to the dicyanovinyl acceptor. Both transitions manifest a pronounced charge transfer character that has been quantified through the  $D_{CT}$  index<sup>175</sup>. This index has a value of 6.70 Å for transition I and 3.67 Å for transition II. The

distance between the donor and acceptor groups in the molecule (monomer in gas phase) is 10.74 Å. This means that for transition I the charge-transfer character is rather pronounced. These same considerations can be translated without much change to dimer 1. Despite the geometric changes induced by crystal phase 1 in the tilting angle of the outer phenyl and the effect on planarity, the two main transitions are very similar and limited to one of the molecules in the dimer. Indeed, the two systems show a similar susceptibility to the presence of a polarisable medium that favours charge-transfer transitions by lowering the overall energy.

Dimer 2 on the other hand, presents a much different response. Due to the different packing, the transitions involve the whole dimer. Transition I corresponds to the transfer of charge from the donor groups to the acceptor groups, occurring symmetrically on both molecules. In this transition, the smaller angle between the planes of the two phenyl rings allows a greater delocalisation of electron density on the outer free phenyl. The change in the angle, -13.84° with respect to the isolated molecule in gas phase, suggests that the inclination of this phenyl ring plays a role in modulating the energy of the transitions by partially modulating the conjugated structure. This fact, together with the favourable interaction of molecular dipoles, contributes to the observed change in the spectrum and also yields a system more tightly bound and more resilient to changes in the electrostatic environment. An indication of this is also given by the change in dipole magnitudes for the three structures. The final dipole of dimer 1 is 23.25 D implying a very limited compensation of single molecular dipoles, in contrast with dimer 2 where the overall dipole moment of 0.0029 D. The two dimers have similar distances between the molecules 3.62 Å for dimer 1 and 3.74 Å for dimer 2, computed as distances between the planes of the two structural phenyl rings of the monomers. The packings are comparably efficient as indicated by the densities 1.494 g/cm<sup>3</sup> for structure 1 and 1.488 g/cm<sup>3</sup> for structure 2.

After this preliminary assessment of the role played by the environment on absorption properties, the actual embedding has been implemented to provide a refined modelling of the crystal medium for both structures. The resulting spectra are reported in Fig. 3.5, while data on the transitions can be found in Table 3.3. Dimer 1 experiences a redshift similar to the one observed in dichloromethane for transition I, 0.27 eV while the redshift in the high-energy transition is more important, reaching a value of 0.31 eV. These values indicate

that molecules in this stacking are rather sensitive to their environment and an accurate modelling of it is absolutely necessary. The situation is similar for dimer 2 but for the opposite reason: in crystal structure 2 the dimers stacked in head-to-tail configuration form strongly interacting pairs, due to the antiparallel dipoles, this means that the electrostatic influence of the medium is less important. Indeed, one could picture this medium as a repeated motif of similar dimeric units with a small dipole moment and thus negligible overall polarisability. Corroborating this result, the charge distribution output from the Ewald procedure for structure 2 yields a spectrum that is very similar to the one in gas phase.

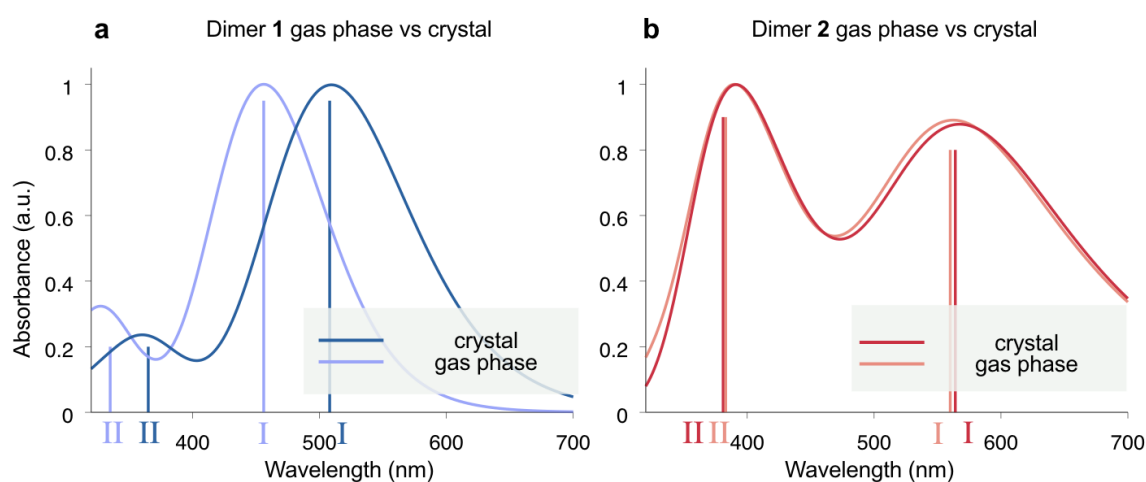


Figure 3.5: Predicted absorption spectra for a dimer 1 in the geometry found in crystal structure 1, b dimer 2 in the geometry found in crystal structure 2, both computed in vacuum and in the presence of the embedding charges. Transition with largest oscillator strengths are indicated with a vertical bar. All spectra are normalised.

The modelling of the crystal phase spectra for structure 1 & 2 and the availability of the experimental thin film absorption spectra before and after thermal treatment has prompted a further investigation aimed at estimating the approximate proportion of each crystal polymorph contributing to the experimental absorption signals. This has been done to validate the hypothesis that a conversion between the two structures, or rather an asymmetrical distribution of the two in the morphology of the thin films after thermal treatment, may be behind the change in the reported absorption signal.

The first step has consisted in performing a fit on the post-thermal treatment absorption spectrum to identify the main transitions responsible for the shape of the final signal. Several

System	Transition I						Transition II					
	gas phase			crystal phase			gas phase			crystal phase		
	$\lambda$	$E$	$f$	$\lambda$	$E$	$f$	$\lambda$	$E$	$f$	$\lambda$	$E$	$f$
dimer 1	456	2.71	1.63	509	2.44	1.74	355	3.70	0.33	366	3.39	0.36
	HOMO-1 to LUMO		58 %	HOMO-1 to LUMO		56%	HOMO-2 to LUMO+1		54%	HOMO-3 to LUMO		58%
	HOMO to LUMO+1		41%	HOMO to LUMO		36%	HOMO-3 to LUMO		15%	HOMO-2 to LUMO+1		28%
dimer 2	560	2.21	0.95	564	2.19	0.94	383	3.24	0.86	383	3.24	0.85
	HOMO-1 to LUMO		70%	HOMO-1 to LUMO		64%	HOMO to LUMO+2		54 %	HOMO-3 to LUMO+1		66%
	HOMO to LUMO+1		28%	HOMO to LUMO		28%	HOMO-3 to LUMO+1		30 %	HOMO-2 to LUMO		20%

Table 3.3: Data on the main transitions for gas phase and crystal phase predicted from spectral calculations at B3LYP/6-311+G(d,p) level of theory. The transitions are marked with vertical bars in Figure 3.5, for each, wavelength  $\lambda$  in nm, energy  $E$  in eV and oscillator strength  $f$  are reported. The proportion of Kohn-Sham orbitals transitions contributing to the main ones is also reported.

combinations of gaussians and lorentzians functions were tested, the best fit was obtained with a combination of three gaussian peaks, according to the following:

$$f_{\text{fit}}^{\text{free}}(\hbar\omega) = \mathcal{N}_a \sqrt{c_a} e^{-c_a \cdot (\hbar\omega - t_a)^2} + \mathcal{N}_b \sqrt{c_b} e^{-c_b \cdot (\hbar\omega - t_b)^2} + \mathcal{N}_c \sqrt{c_c} e^{-c_c \cdot (\hbar\omega - t_c)^2} \quad (3.1)$$

Relevant data on the fit are reported in Table 3.4. The region between 1.6 to 3.0 eV (roughly from 410 nm to 775 nm) has been chosen due to the largest value of normalised absorption. It is reasonable to assume that the spectrum after thermal treatment is characterised by different crystalline grains and regions with a more amorphous character. If the two polymorphs have a small relative free-energy difference (within 1-2 kcal/mol<sup>176</sup>) the grains will present the molecular packing of either structure 1 or 2.

Dataset	$R^2$	Relative strength $\mathcal{N}_{a,b,c}$	HWHM $\text{HWHM}_{a,b,c}$	Energy $e_{a,b,c}$
Free fit on sp. after thermal treatment	99.05 %	0.69	0.14	2.03
		0.68	0.17	2.49
		1.00	0.13	2.27
	$R^2$	Concentration $\mathcal{N}_{1,2,\text{am}}$	HWHM $\text{HWHM}_{1,2,\text{am}}$	Shift $e_{1,2,\text{am}}$
Constrained fit on sp. after thermal treatment	99.35 %	0.257	0.17	-0.03
		0.381	0.17	-0.20
		0.362	0.17	-0.14
	$R^2$	Concentration $\mathcal{N}_{1,2,\text{am}}$	HWHM $\text{HWHM}_{1,2,\text{am}}$	Shift $e_{1,2,\text{am}}$
Constrained fit on sp. before thermal treatment	99.91 %	0.368	0.21	0.19
		0.011	0.21	-0.30
		0.621	0.21	0.03

Table 3.4: Parameters from the fits performed on the available experimental spectra. The original absorption signal from ref. [156](#) is normalised, for this reason, relative strengths obtained from the free fit are reported with the largest value normalised to one. For the free fit the R-squared (percentage of the variability in the data explained by the model) is reported as goodness-of-fit measure along with the parameters of the peaks: strength, half-width at half-maximum (HWHM) in eV and energy of the transition in eV. Data for the constrained fits (on as-cast and post-thermal treatment spectra) are presented on the relative concentration of each component (amorphous, structure 1 and structure 2) normalised to 1, together with the energy shifts  $e$  of the predicted spectra (see model in Eq. [3.1](#)), the overall broadening of transitions (HWHM) and the R-squared.

The three peaks identified from the fit, can be attributed to the contributions of the three possible morphologies coexisting in the thin film. The peak at 2.03 eV is compatible with the low-energy transition predicted for structure 2 (2.19 eV), the second at 2.49 eV can be attributed to the absorption of structure 1 (2.44 eV) while the peak at 2.27 eV is likely linked to the amorphous phase. The amorphous spectrum can be approximated by the monomer's spectrum in dichloromethane with the brightest transition at 2.29 eV. The relative heights of the peaks are the product of the absolute strength of the transition (i.e. the oscillator strength) times a factor proportional to the relative abundance of each component in the thin

film. Theoretical values of oscillator strengths are available from the predicted absorption spectrum, so the necessary step to extract quantitative information on relative abundance of the various components is to perform a constrained fit on the final spectrum which includes the estimated parameters available from the theoretical prediction.

The constrained fit is performed applying the following model:

$$\begin{aligned}
 f_{\text{fit}}^{\text{constr.}}(\hbar\omega) = & \mathcal{N}_1 \sqrt{c} \left( f_{11} \cdot e^{-c \cdot (\hbar\omega - t_{11} - e_1)^2} + f_{12} \cdot e^{-c \cdot (\hbar\omega - t_{12} - e_1)^2} + f_{13} \cdot e^{-c \cdot (\hbar\omega - t_{13} - e_1)^2} \right) + \\
 & \mathcal{N}_2 \sqrt{c} \left( f_{21} \cdot e^{-c \cdot (\hbar\omega - t_{21} - e_2)^2} + f_{22} \cdot e^{-c \cdot (\hbar\omega - t_{22} - e_2)^2} + f_{23} \cdot e^{-c \cdot (\hbar\omega - t_{23} - e_2)^2} \right) + \\
 & \mathcal{N}_{\text{am}} \sqrt{c} \left( f_{\text{am}} \cdot e^{-c \cdot (\hbar\omega - t_{\text{am}} - e_{\text{am}})^2} \right)
 \end{aligned}
 \tag{3.2}$$

where the position of the peaks and the oscillator strengths are taken from the simulated spectra for the involved structures. All predicted transitions with energy inside the fitting interval, i.e. between 1.6 and 3.0 eV, and having a non-vanishing oscillator strength are included in the fit with a gaussian broadening. Data on these excited states are available in Table [3.3](#).

To build the fitting model a broadening  $c$  common to all transitions, an independent concentration  $\mathcal{N}_i$  as well as an energy shift  $e_i$  on the position of each spectra (all peaks in a single spectrum are assumed to be correlated) have been considered, yielding a final model with 7 free parameters.

The choice of a single broadening parameter for all peaks is justified by the fact that all components are expected to be affected similarly by the conditions in the thin film, vibrational contributions are assumed negligible. Values for the best fit are presented in Table [3.4](#). An analysis of the best-fit parameters offers valuable information about the system. After thermal treatment, the morphology of the thin film seems to be equally distributed between the different components with a prevalence of structure 2 (38.1%) and the amorphous phase (36.2%) over structure 1 (25.7%). This fact is a strong indication that the emergence of structure 2 as main component is a plausible explanation for the observed spectral change. Other important information is that all the predicted spectra are redshifted with respect to the experimental signal. The agreement is worse with structure 2 spectrum and the one used to model the amorphous phase (i.e. monomer in dichloromethane). In this case, the shift is rather pronounced for structure 2 spectrum while it is within the expected B3LYP error [177](#)

for the other component. Prediction of structure 2 spectrum is most likely to be affected by errors since it is lacking any experimental input.

To collect further proof that the formation of many structure 2 crystallites in the final thin film is indeed responsible for the changes in the spectrum, another fit with the same model as in Eq. 3.2 has been performed on the experimental absorption signal before thermal treatment. The fit confirms this hypothesis by indicating a prevalence of amorphous phase and structure 1, respectively 62.1% and 36.8%, while structure 2 only contributes as the 1.1% of the initial thin film morphology.

The comparison between before and after thermal treatment populations suggests that most structure 2 crystallites form starting from the amorphous regions, which decreases from 62.1% to 36.2%, while the interconversion between the two forms is limited (only 11%).

These data suggest that the thin film conditions have an effect on the free energy landscape such that the barrier to access the minimum corresponding to structure 2 is lower than the one corresponding to structure 1 which is nonetheless dominant in bulk conditions<sup>[156]</sup>. To better understand why this is the case, dimer geometries relaxed in dichloromethane with similar character to the ones found in the crystal polymorphs 1 and 2, i.e. “co-facial” and “head-to-tail”, were considered and their energy difference with respect to the single monomer in dichloromethane was derived. The choice of dichloromethane geometries was done to model the conditions of the amorphous phase in keeping with the assumption adopted before to model amorphous absorption. The desire to model the amorphous phase was motivated by the observation, from previous results, that a large part of the new structure 2 crystallites should nucleate from this phase.

Results suggest that dimers in the head-to-tail configuration have an energy gain of -6.54 kcal/mol while dimers stacked in a way similar to dimer 1 result in a slightly lower energy gain of -6.00 kcal/mol. Because of this difference the formation of “head-to-tail” dimers appears to be 2.15 times more probable than the other configuration.

Based on these considerations one could speculate that structure 1 has a more favourable packing from the energetic point of view yet has a smaller probability of nucleation because a larger assembly of monomers than the dimer is needed in order to stabilise the structure.

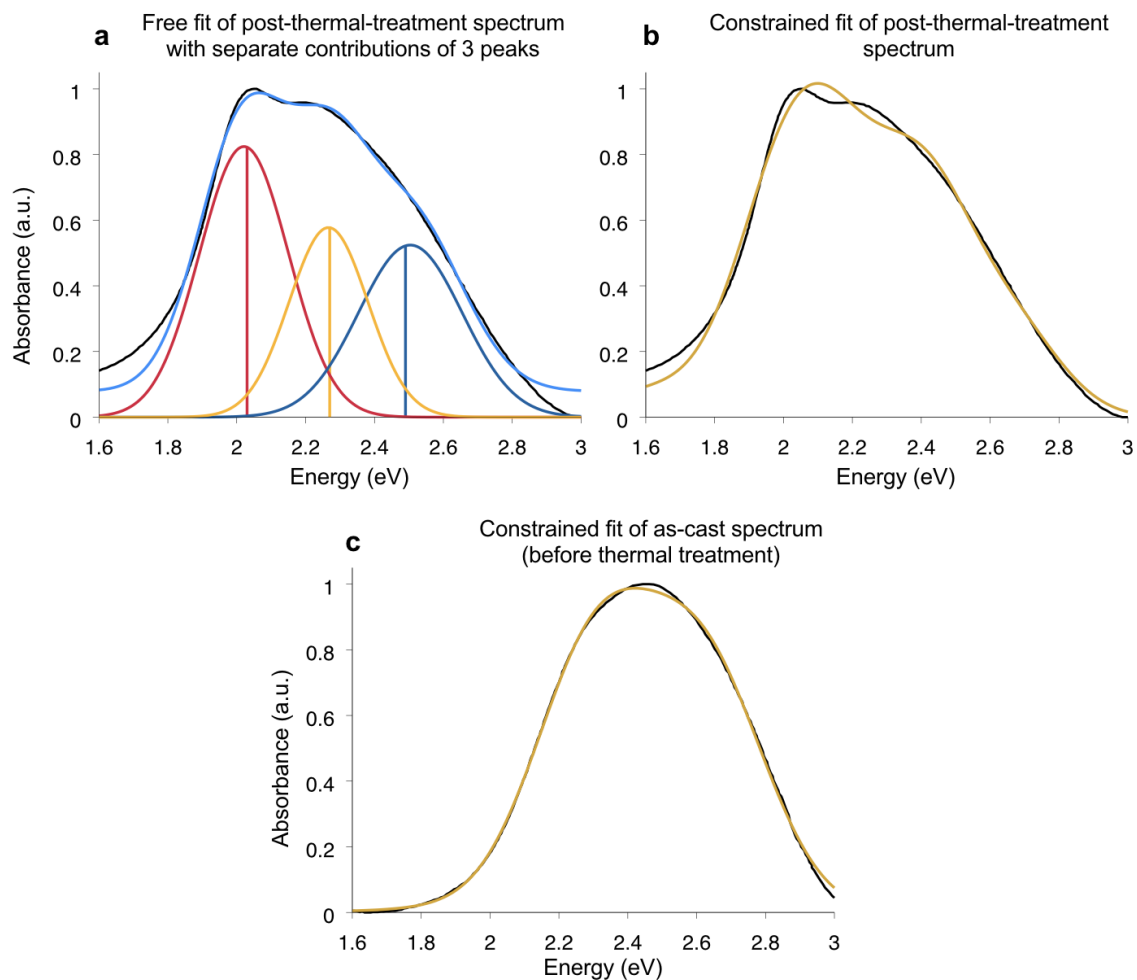


Figure 3.6: Plots of all the performed fits to the available experimental signals (black solid lines). Panel a reports the free fit and also shows the single components identified, numerical values can be found in Table 3.4. Panels b & c show the plots of the constrained fits mixing the predicted transitions between 1.8 and 3.0 eV for all components (structure 1, 2 and amorphous). Fitted curves are reported in golden colour and, when necessary, extrapolated beyond the fitting range.

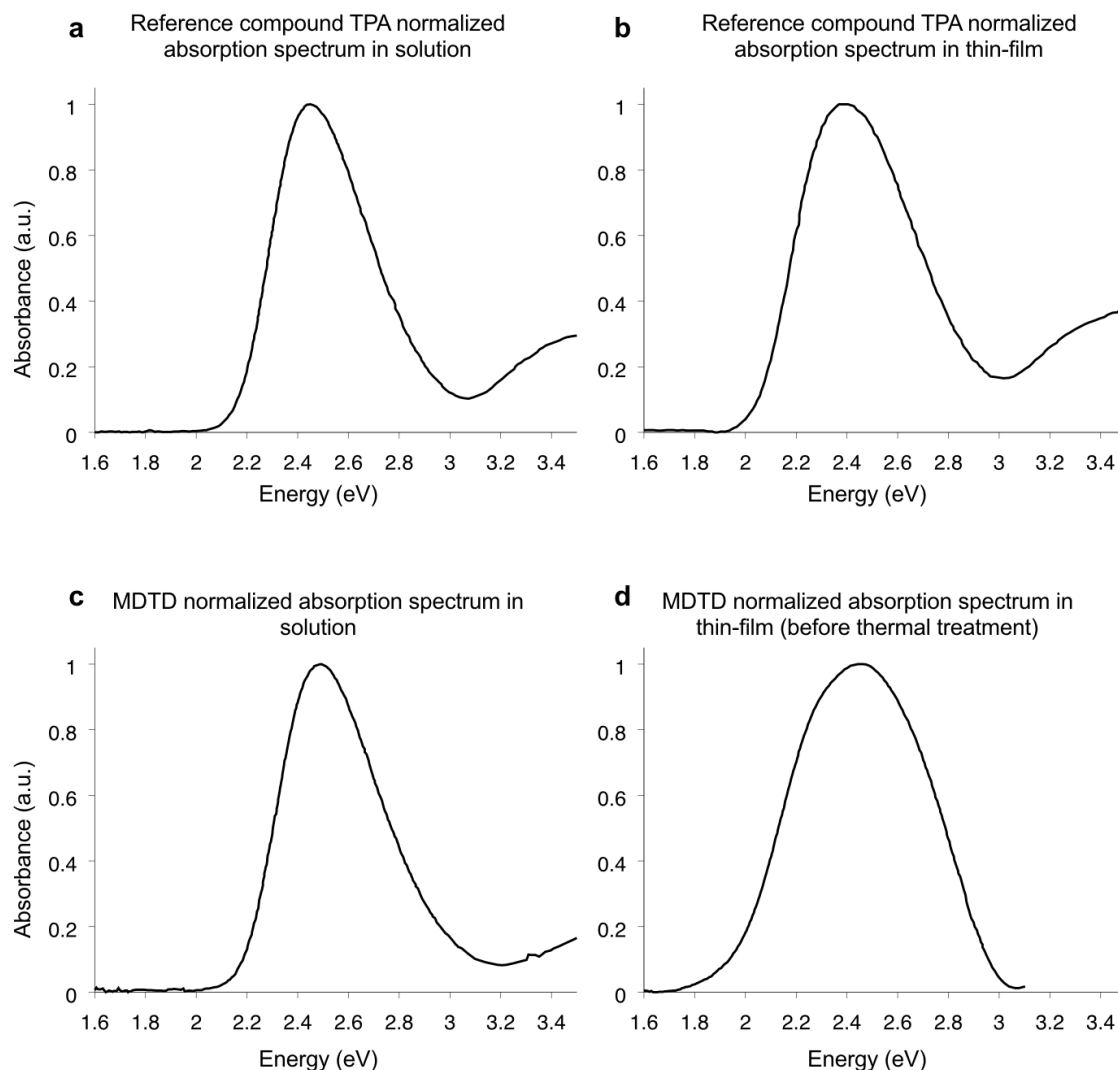


Figure 3.7: Normalised experimental absorption signals taken from ref.<sup>[156]</sup>. Panel a&b report the spectra for the reference compound triphenylamine from which MDTD is derived. TPA and MDTD performances are compared in ref.<sup>[156]</sup>. As already remarked, the similarity between the solution and thin-film spectra suggests a low degree of crystallinity of TPA thin-films. Panel c&d show the spectra for MDTD in solution and in thin film conditions before thermal treatment (used in the second constrained fit). All reported spectra are transformed in absorbance vs energy (eV) to appropriately visualise the broadening.

Fig. 3.6 shows all plots for the fits performed on the experimental signals before and after thermal treatment.

To further validate the observations from the absorption signals, carrier mobility in the thin film has also been predicted. According to ref.<sup>[156]</sup>, alongside the improved absorption properties, due to the change in the spectrum, an increase in charge transport efficiency with respect

to the TPA compound from which MDTD is derived is also observed. In particular, hole mobility increases from  $1.0 \cdot 10^{-5} \text{ cm}^2 / \text{ V} \cdot \text{ s}$  of the reference compound to  $5.0 \cdot 10^{-4} \text{ cm}^2 / \text{ V} \cdot \text{ s}$  of MDTD thin film after thermal treatment<sup>[156]</sup>. Although similar data on reference compound thin films are not available, theoretical results indicate that the increase is likely due to a larger degree of crystallinity of MDTD thin films, which is 63.8% in the films after thermal treatment. Indeed, from experimental ref.<sup>[156]</sup>, solution and thin film spectra of the reference compound appear to be very similar, suggesting a low degree of crystallinity for TPA thin films. The same is true for the solution and the thin film spectra before thermal treatment of MDTD available in Fig. 3.7. Results for the mobility according to kinetic Monte Carlo simulations of Marcus-like transport are reported in Table 3.5.

Component	$\mu_x$	$\mu_y$	$\mu_z$	$\mu_{\text{avg}}$	$k_{ij}^{\text{max}}$
structure 1	$2.98 \cdot 10^{-3}$	$7.78 \cdot 10^{-7}$	0.00	$1.80 \cdot 10^{-3}$	$2.6 \cdot 10^{14}$
structure 2	$9.55 \cdot 10^{-4}$	0.00	$1.60 \cdot 10^{-4}$	$4.25 \cdot 10^{-5}$	$4.6 \cdot 10^{14}$
amorphous	-	-	-	$3.30 \cdot 10^{-11}$	-

Table 3.5: Hole mobility estimates in  $\text{ cm}^2 / \text{ V} \cdot \text{ s}$  along the x, y and z cartesian axes and the average value. In the last column the value of the largest Marcus exchange rate between two neighboring molecules for each crystal structure is reported in  $1/\text{ s}$ . \*\*Amorphous mobility has been taken from ref.<sup>[162]</sup>.

The two MDTD polymorphs show different transport behaviours that naturally, can be attributed to the differences in their molecular packings. To make the comparison easier, mobilities along a common set of cartesian axes are reported. Both structures have their largest value of mobility along x.

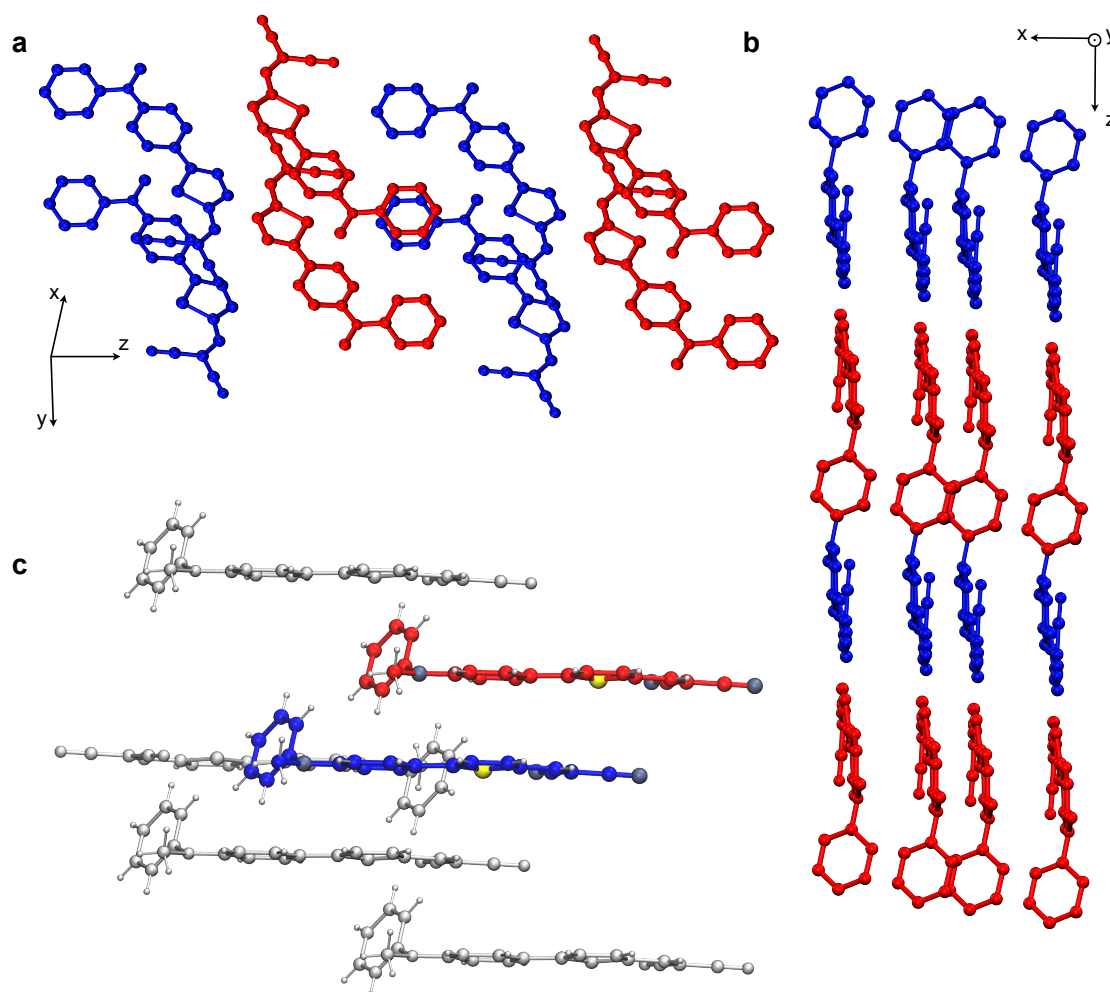


Figure 3.8: Representations of a  $2 \times 2 \times 2$  supercell of structure 1. Panel a shows the bc crystal plane with the two molecules transformed according to the space group elements in red and blue. Panel b shows the stacking of this structure in the a direction, that corresponds to x. Panel c features the group of neighbours considered for hole transport when the carrier is localised on the blue molecule.

Structure 1 presents a more isotropic mobility along all directions with mobility between 5 and 10 times smaller with respect to the dominant axis, yet still rather large for typical small-molecule donor materials. As already pointed out, structure 1 belongs to the  $P\bar{1}$  space group. The two molecules in the unit cell form a motif in the bc crystal plane that is then stacked in the a direction, which corresponds to the cartesian x axis (Fig. 3.8). This last direction is the one with the largest exchange. Hole transport is favoured by the increased planarity of MDTD molecules which fosters strong  $\pi$ - $\pi$  interactions yielding an efficient stacking responsible for large transfer integrals and hence transfer rates. The dimer with the largest transfer integral is the same dimer in Fig. 3.3b, considered for optical response.

Indeed, in the stacking direction mobility reaches a value of  $\mu_h^x = 1.26 \cdot 10^{-4} \text{ cm}^2/\text{V} \cdot \text{s}$ . In the other directions geometrical factors severely hamper electronic coupling and hence mobility, notably the edge-to-edge configuration of neighbouring pairs and their relative distance.

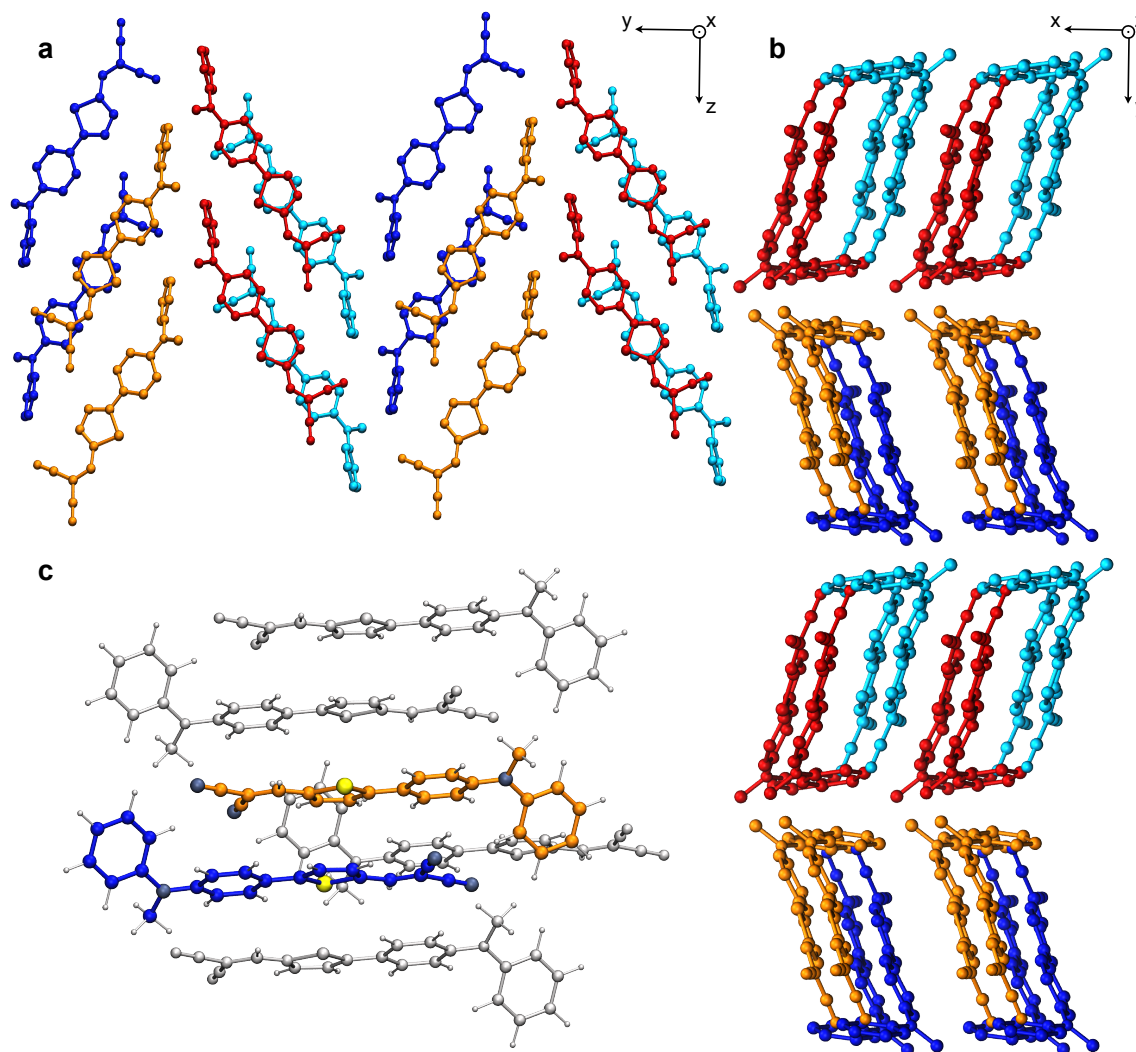


Figure 3.9: Representations of a  $2 \times 2 \times 2$  supercell of structure 1. Panel a shows the bc crystal plane with the four molecules transformed according to the space group elements in red, blue, cyan and orange. Panel b shows the stacking of the structure formed across bc in the a direction, that corresponds to x. Panel c features the group of neighbours considered for hole transport when the carrier is localised on the orange molecule.

Structure 2 belongs to space group  $P2_1/c$ . The four molecules in the unit cell form two herringbone structures in the yz-plane. The herringbone backbones can be identified as the outer phenyl rings of the donor group aligned in the z direction. The structures (orange&red and cyan&blue) are repeated along y, as shown in Fig. 3.9, and have opposite orientations

along z, i.e. donor-acceptor axes have opposite orientations and present a small offset in the x direction. The larger structure made up of the two planes is then stacked along x. Molecules belonging to different herringbones, i.e. cyan&red or blue&orange, form the head-to-tail dimers considered for the optical response that is also the pair with the largest transfer integral and exchange rate (see Fig. 3.9). This is further highlighted by the value of the mobility along x, for which a mobility of  $9.55 \cdot 10^{-4} \text{cm}^2/\text{V} \cdot \text{s}$  is reported, the largest among all directions.

$$\mu_{\text{thin-film}}^{\text{final}} = p_{\text{str } 0} \times \mu_{\text{str } 0} + p_{\text{str } 1} \times \mu_{\text{str } 1} + p_{\text{am}} \times \mu_{\text{am}} = \quad (3.3)$$

$$= 0.257 \times 1.8 \cdot 10^{-3} + 0.381 \times 5.6 \cdot 10^{-4} + 0.362 \times 3.3 \cdot 10^{-11} = 6.75 \cdot 10^{-4} \text{cm}^2/\text{V} \cdot \text{s} \quad (3.4)$$

The estimate is 1.35 times larger than the measured value, given the extent of the extrapolation and the many approximations involved, these estimates may be said to be in reasonable agreement with the experimental mobility and provide further evidence that the emergence of domains with a packing in agreement with structure 2 is a plausible explanation for the changes in the behaviour of the thin films.

### 3.4 Conclusions

The results of this theoretical investigation strongly suggests that the formation of crystallites with molecular packing close to the one found in structure 2 is the source of the change in absorption properties. Structure 2 appears more easily accessible starting from the amorphous phase, indicating that in thin film conditions this structure has a lower kinetic barrier height possibly due to dipole-dipole interactions. Contrary to the initial hypothesis, the interconversion between the two structures is rather limited. Structure 1, observed to be the dominant form in bulk conditions<sup>156</sup>, is more difficult to populate with respect to structure 2 in the conditions of the experimental study.

MDTD offers an example of an organic semiconductor that, due to its large dipole moment, undergoes dramatic changes in its self-assembly mechanism depending on the external conditions.

Although, in the particular case of MDTD the analysis is rather straightforward because the material experiences a particularly pronounced change in absorption, it can be expected that the same procedure, might likewise extract crucial information on morphology for other molecules for which electrostatic interactions are dominant, notably molecules with a push-pull character belonging to the class of D- $\pi$ -A. Control over electrostatic interactions via molecular level engineering, i.e. choice of functional groups in the D and A moieties, could allow remarkable control over supramolecular organisation and ultimately morphology. This mastery in directing the self-assembly of these systems would signify a considerable step forward to achieve a more complete control over the performance of functional materials in the domain of energy harvesting and far beyond.

# Chapter 4

## A donor-acceptor dyad test-case

After having studied MDTD as an example of a small-molecule donor, in this chapter, another theoretical investigation is presented on a compound issued from another trending topic in organic photovoltaics: single photoactive materials.

Devices based on single materials do not need *D-A* blends in their photoactive layers to generate photocurrents with exploitable intensity. In fact, analogously to what happens in inorganic semiconductors, they are able, alone, to ensure the production of free charge carriers with a reasonable efficiency.

The idea is not new; indeed, among the first organic solar devices conceived, it is possible to find many employing a single organic layer that were quickly discarded due to their poor performances after the advent of the planar heterojunction design<sup>[22]</sup>.

These initial poor performances can be traced back to one of the most characterising aspects of the physics of organic solar cells. The localisation of electrons in organic systems is constrained to the molecular structure and the relative dielectric constant for these materials is 2-3 times smaller than that of silicon.

These conditions result in the pair of the excited electron and the hole, called exciton, to be strongly bound ( $E_B \sim 500$  meV)<sup>[16][178]</sup>. As a consequence, thermal energy at ambient conditions is not enough to free a sufficient number of charge carriers.

Solving the problem of exciton dissociation is at the basis of the heterojunction design. Combining two materials with different electron affinities (i.e. a donor and an acceptor) results in an interface where excitons can be split and converted into a photocurrent. As remarked in

the introduction, planar heterojunctions are not able to solve all the problems, since another strong constraint is associated with the ability of excitons to reach the interface between the two materials. Excitons tend to be relatively short lived with average mean free paths before recombination that rarely go beyond 30 nm<sup>[24][178][179]</sup>. This means that there is a constraint on the thickness of the photoactive layer and this negatively impacts on the absorption properties of the active layer.

To overcome this further limitation, different strategies have been tested and one of the most efficient has been the combination of the two blended materials in new active layer morphologies. The result has been the conception of the so-called bulk heterojunction<sup>[180][181]</sup> for which an interface interspersed within the bulk of the active layer is produced. Ideally, within these new bulk conditions, all excitons generated within the volume are never too far from the interface and most of them can be split.

The efficiency of bulk heterojunctions ultimately depends on the properties of the phase separation between donor and acceptor. The optimised bulk interface that may arise from given deposition techniques is usually not thermodynamically stable and tends to degrade over time<sup>[74][182]</sup>. This degradation naturally affects photovoltaic performance and severely shortens device lifetime.

The recent renewed interest<sup>[71][77][86][183][184]</sup> in photoactive organic materials capable, alone, of ensuring excitonic separation, stems from the limited success at interface stabilisation and from the considerable advances in the theoretical understanding of the dissociation process.

As seen in the previous chapter, the trend of small-molecule donors arose to meet the demands of a community eager to rationalise the behaviour of organic materials through the study of chemical systems less complex than photoactive polymers. On the other hand, the design of small-molecule donors also comes from the realisation that the covalent linkage of moieties with different electronic affinities leads to the tuning of the relevant material properties. Electron-donating and electron-accepting groups in the same molecule foster the appearance of charge transfer transitions upon photon absorption. These transitions are often associated with better absorbing character and less bound excitons that are easier to split. This process is more complicated than inorganic materials since it involves steps determined by the complex electronic structure originating from the molecular architecture<sup>[185]</sup>.

The concept carried a little further and applied to bulk heterojunctions has allowed the emergence of molecular designs combining a known donor and a known acceptor with a link that is able to prevent excessive coupling (i.e. donor and acceptor properties are mostly retained). The link generates compounds capable of even more pronounced photoinduced charge transfer transitions leading to charge carrier separation on the molecule itself.

Hence, a new generation of compounds marks the return of single material organic solar cells (SMOSCs) on the forefront of organic photovoltaics research decades after the first underwhelming attempts. This new generation also carries another strong legacy from the intervening years. Molecules chosen to build these new *molecular heterojunctions*<sup>[186]</sup> are often found within a large database that has been compiled for donors and acceptors alike.

Many of these materials in fact, carry one or more fullerene moieties in combination with a small oligomer or another type of donor<sup>[71]</sup>. Commonly, structures with these properties are referred to as dyads. Dyads are not new in the landscape of molecular chemistry but the specific application in photovoltaics is rather recent<sup>[71]</sup>. So that data on photoelectric properties for many dyads is often available but a thorough characterisation of supramolecular organisation and its effects on important properties is lacking.

The investigation proposed in this chapter aims at partially filling this gap. At least for what concerns the information about length scales associated to the local molecular environment. To this end methods from chapter 2 are again applied to this chemical system with the goal of probing the character of self-organisation and its influence on mobility using direct atomistic detail. The structure of the chapter consists in an introduction on the compound followed by a section on the computational methods where particular care is devoted to the description of how methods of chapter 2 have been complemented to obtain mobility. Computational details are duly followed by the description of the main results and a closing section summarising the main findings.

## 4.1 The DPP-Ful donor-acceptor dyad

The dyad object of this study is obtained via the covalent bonding of a N-methyl [60]-fulleropyrrolidine (Ful), playing the role of acceptor, with a  $\pi$ -conjugated monodisperse oligomer, in this case a dithiafulvalene (DTF)-functionalized diketopyrrolopyrrole (DPP)

acting as donor<sup>[87]</sup> (see Fig. 4.1).

Experimentally<sup>[87]</sup>, the two moieties were selected on the basis of the performances of the separated molecules reported in the literature<sup>[187]</sup>, rather than through the application of more rigorous purpose-oriented design rules. Fulleropyrrolidine was chosen because fullerene derivatives still dominate the category of acceptor materials, although recently more and more effort has been put into the development of non-fullerene acceptors (NFA)<sup>[64][65][66]</sup>. The donor moiety instead, was chosen to compensate the poor absorption typical of fullerenes and on the basis of certain features thought to promote processability and good molecular packing, essential to transport efficiency<sup>[188][189][190]</sup>. In this work, the focus is precisely on transport dynamics of DPP-Ful with the aim of pointing out the electronic and structural features of the dyad that are most relevant to enhance power conversion efficiency.

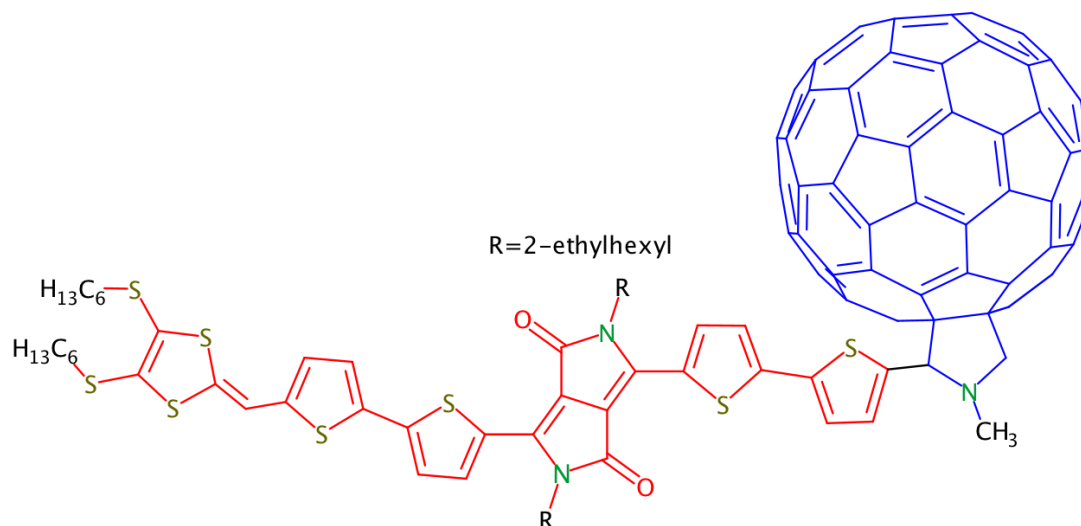


Figure 4.1: Chemical structure of DPP-Ful with [60]-fulleropyrrolidine (Ful) acceptor moiety in blue and the diathiafulvalene-functionalised diketopyrrolopyrrole (DPP) donor moiety in red.

## 4.2 Computational details

The modelling of DPP-Ful poses specific challenges due to its nature of ambipolar conductor<sup>[191]</sup>. Carriers of both signs can be transported independently over morphologies whose microscopic details are not entirely known<sup>[90][159]</sup>. As already discussed, from a theoretical point of view this requires the simulation of both ordered and disordered morphologies and to

model transport in both conditions. The first mandatory steps consist in the gas phase calculations on the isolated molecule. These calculations have been performed at density functional theory (DFT) level applying the B3LYP functional in conjunction with the triple- $\zeta$  Pople's basis set (6-311G(d,p))<sup>[111][112]</sup>. Dispersion interactions have been accounted for through the Grimme's empirical potential (D3)<sup>[118][120]</sup>. All optimisations have been performed at the same level of theory via the Gaussian09 package<sup>[192]</sup>.

Similarly to the system investigated before, the identification of the thermodynamically most relevant crystal structures has been performed via the polymorph predictor module of Materials Studio<sup>[193]</sup>. The prediction of crystal structures is carried out by arranging the packing motifs within a given space group and then by simultaneously optimising molecular packing inside the cell together with the unit cell parameters, exploiting the Monte Carlo procedure outlined in chapter 2. These steps were carried out using the DREIDING force field<sup>[133]</sup>, largely employed for molecular crystal prediction<sup>[9]</sup>. The search has been limited to the most probable space groups reported for similar organic compounds i.e.  $P2_12_12_1$ ,  $P2_1/c$ ,  $P\bar{1}$ ,  $P2_1$ ,  $C2/c$  and  $Pna2_1$  according to a series extensive studies<sup>[140]</sup>. A number of independent searches have been performed until no new low-energy structures, "significantly different" from those already obtained, were found. The resulting structures were clustered and ranked according to their energy and density and those with the highest rank were selected.

This ranking was then refined on the basis of to the results of full periodic DFT geometry optimisations of the unit cell parameters and atomic positions performed via CRYSTAL17<sup>[136]</sup>. The same exchange correlation functional, B3LYP-D3, was used together with an optimised basis set, tailored to describe the electronic density in condensed organic materials.

Amorphous configurations were extracted following an MD based protocol. Disordered configurations for a system of 500 molecules were obtained by taking 150 uncorrelated snapshots from a MD trajectory. The initial conditions were chosen as to accurately reproduce the disordered morphology. DPP-Ful molecules were initially placed at random positions in a cubic cell 270 Å wide. This configuration was evolved through a simulation in the NPT ensemble at high temperature  $T=800$  K and  $P=1$  atm until the volume of the cell reached convergence. Another NPT simulation was then performed at lower temperature,  $T=300$  K. The system was further evolved through a third NPT simulation for data production. All equilibrations are terminated at convergence of the volume. The data production run outputs

a 30 ns long trajectories. Simulations have been carried out via the NAMD2.12 package<sup>[194]</sup> in combination with CGenFF<sup>[134][135]</sup> and RESP<sup>[164]</sup> charges extracted from one of the above gas phase DFT calculations. Van der Waals cut-off is set at 12 Å and electrostatic interactions were treated according to the particle mesh Ewald method.

Charge dynamics was simulated, for both crystalline and amorphous phases, using the non-adiabatic high-temperature limit of the semiclassical Marcus charge transfer theory<sup>[195]</sup>, of which an overview is given in chapter 2. In the case of DPP-Ful, the approximation is justified by the fact that charge carriers in organic materials are mostly localised on single molecules that weakly interact with their neighbours<sup>[24][35][142][196]</sup>.

It can be useful to remind that in Eq. 2.46, the main parameters encoding microscopic information, are the reorganisation energy  $\lambda$ , a molecular level property evaluating the energy cost of exchanging a charge carrier, and the transfer integral  $J_{ij}$ , that is computed for each pair of exchanging molecules and quantifies the propensity of the carrier to be transferred mediated by the interaction Hamiltonian of the pair.

In the framework of Marcus theory conditions the coupling  $J_{ij}$  should be “small” compared to  $\lambda$  so that the interaction term between molecules in the exchanging pair can be treated perturbatively<sup>[146]</sup>. Calculations described in the following approximate reorganisation by neglecting the contribution due to the change in polarisation of the surrounding environment given by the exchange. Only intramolecular geometry reorganisation is considered according to the so-called “four-point method”<sup>[197][198]</sup>:

$$\lambda(h/e) = E_{nC}^{h,e} + E_{nC}^{h,e} - E_{cC}^{h,e} - E_{nN}^{h,e} \quad (4.1)$$

where the subscripts indicate molecular state ( $c$  or  $n$ , charged or neutral) and molecular geometry ( $C$  or  $N$ , charged optimised or neutral optimised). For the sake of coherence, the same DFT approach, B3LYP-D3, has been used for the calculations of reorganisation energies. The electronic couplings, also called transfer integrals, are computed treating the exchanging pair as an isolated dimer under the assumption that its orbitals arise just from the interaction of monomer frontier orbitals – HOMO for hole transport and LUMO for electron transport –  $\phi_i^{\text{H/L}}$  and  $\phi_j^{\text{H/L}}$ <sup>[199]</sup>:

$$J_{ij} = \langle \phi_i^{\text{H/L}} | \hat{H}_{\text{dimer}}^{\text{int}} | \phi_j^{\text{H/L}} \rangle \quad (4.2)$$

All the orbitals needed to estimate the electronic coupling are obtained through the semiempirical ZINDO method<sup>96</sup>, which has been proven to provide rather accurate estimates<sup>146</sup>.

Rates are evaluated for all pairs specified in this list. The final step to estimate mobility is to perform kinetic Monte Carlo simulations using the computed rate constants. As explained in chapter 2, see Eq. 2.39, mobility is given by the ratio of  $\langle v \rangle$ , the average velocity in the direction of the electric field  $\vec{E}_{\text{field}}$  and the magnitude of the latter. Since the molecule carries both a DPP electron donor moiety and a fullerene electron acceptor group and the two act as separate transport channels, the two distinct conducting moieties have been defined in order to simulate the charge-separated (CS) state. The separation of the two moieties is performed according to the localisation of the HOMO and LUMO orbitals (see Fig. 4.2). The separation is carried out by cutting the bond between the pyrrolidine in the fullerene moiety and the proximal thiophene ring, as sketched in Fig. 4.1. The bonds at the cut are saturated with hydrogen atoms and the computational procedure to simulate transport is applied to the morphologies of the separated moieties.

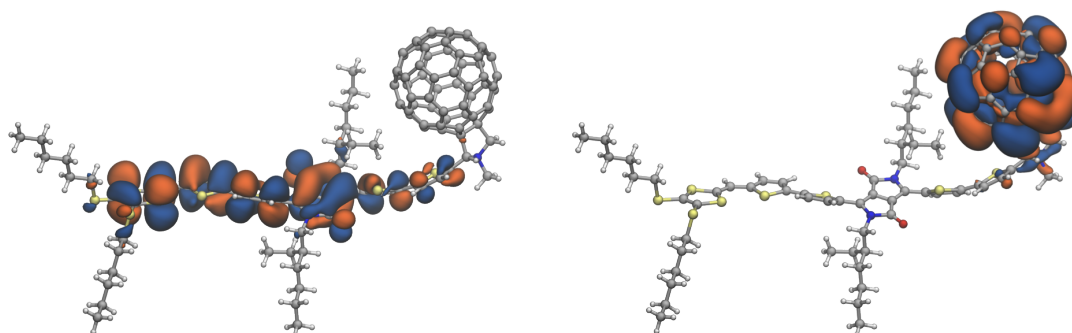


Figure 4.2: Isosurface (values  $\pm 0.005$ ) representation of frontier orbitals. (left, HOMO; right, LUMO).

### 4.3 Main results

In the previous section, it has been largely stressed that Marcus rates depend critically on two parameters (see Eq. 2.46) associated with molecular electronic properties and that these parameters need to be complemented with a description of the bulk structural properties (i.e. crystal structure packing or amorphous packing) of the materials that inform the model about the morphology. Their prediction is essential in producing a reliable simulation of charge transport performance.

Bulk properties are linked to morphology in condensed phase that is the result of the self-organisation of large numbers of molecules (i.e. the result of their intermolecular interactions). The prediction of solid phase packings, either crystalline or amorphous, remains to this day quite challenging<sup>[127][128][129][130][176]</sup>. This is especially true for relatively large organic compounds like dyads that, with many degrees of freedom, have a higher chance of showing polymorphism<sup>[200][201]</sup>.

The main difficulty lies in the heavy computational cost of an accurate treatment of intermolecular interactions that require a high-level description of the electronic structure including dispersion forces, a key driver for aggregation in molecular solids<sup>[200][202]</sup>.

As seen before in this investigation, crystal packings are guessed via a not-so-demanding computational procedure, that employs a classical force field for energy evaluation coupled with a Monte Carlo simulated annealing<sup>[203]</sup>. The output is a set of the most thermodynamic viable crystal polymorphs whose ranking is refined through higher level calculations. This procedure still overlooks contributions to the ranking, like the entropic contribution, that might change it significantly<sup>[176][203]</sup>.

Nonetheless, the hope is that a comparison between properties estimated for these simulated packings and the available experimental data may lead to the identification of the molecular packing behind the experimental observation. This is of course very relevant since it provides direct knowledge of microscopic details that either boost or inhibit transport efficiency of charge carriers. Moreover, the availability of crystal morphologies not directly accessible in the experiments due to their unfavourable thermodynamic rank, allows a comparison between them. Starting from this, a more general picture can be drawn that provides evidence essential in defining a set of synthetic principles to be followed in the design of dyads with enhanced performance.

### 4.3.1 Isolated molecules and crystalline polymorphs

A first step has been the characterisation of molecular properties relevant to charge transfer in gas phase. Previous works<sup>[71][87]</sup> have largely stressed how, in dyads, properties of the isolated donor and acceptor moieties should be retained in order to ensure optimal transport of the charge carriers in the final architecture. This means that they should remain suffi-

Data from	$\lambda_{\max}$	Oscillator strength	$E_{\text{HOMO}}$	$E_{\text{LUMO}}$	$\Delta E_{\text{gap}}$
B3LYP-D3/6-311G(d,p) calc.	622 (1.99 eV)	0.9	-4.88	-3.83	1.05
Experimental	653 (1.89 eV)	-	-4.95	-3.23	1.72

Table 4.1: Comparison between the results of the theoretical calculation and the available experimental data from<sup>[87]</sup>.  $\lambda_{\max}$  is reported in nm, the energies in eV.

ciently decoupled in terms of their respective electronic structure. A qualitative indication of this decoupling is given by the localisation of the frontier orbitals of the molecule reported in Fig. 4.2, whose energies are reported in Table 4.1. In this case, the strong localisation of the frontier orbitals in different parts of the molecule is clear evidence that the moieties are kept largely independent by the linker and can efficiently produce a charge-separated state<sup>[15][185]</sup>. Indeed, the HOMO is highly localised on the donor moiety, DPP, while the probability amplitude of the LUMO is markedly centred on the Ful moiety.

This effect can be traced back to some structural features of the dyad. In particular, the possibility of weak interactions of the fullerene with the closest aliphatic chain reduces the planarity of the thiophene rings linking the fullerene moiety to the diketopyrrolopyrrole group. As a consequence,  $\pi$ -conjugation is constrained to the remaining part of the donor moiety, producing a certain degree of insulation between the two parts, as can be seen in Fig. 4.2. This effect is further modulated by the interactions proper to each polymorph packing where it is generally amplified.

Starting from the gas phase data, reorganisation energies were also estimated according to Eq. 4.1. The ambipolar character of the molecule implies that both anionic and cationic states should be investigated. Despite the moieties being virtually independent in terms of transport after charge separation, the response of the whole structure to the presence of a carrier has been considered. Computed values for the hole ( $\lambda(h) = 361$  meV) are compatible with those reported for other diketopyrrolopyrrole derivatives,  $\lambda(h) \sim 300\text{--}400$  meV<sup>[204][205]</sup>. At the same time, the energy cost for the exchange of an electron ( $\lambda(e) = 212$  meV) is larger than but still compatible with the reported reorganisation energies for similar fullerene derivatives,  $\lambda(e) \sim 130\text{--}150$  meV for PCBM<sup>[206]</sup>. This agreement may be read as further evidence of the efficient decoupling of the moieties.

In general, polymorphs of the same compound can exhibit dramatically different transport properties. Thin films employed as active layers usually have a pronounced polycrystalline character, so that it could be expected that different crystal domains, with distinct orientations and possibly packing, will coexist with less ordered regions<sup>[159]</sup>. In order to provide a reasonable description of the structures present in DPP-Ful thin films, the 5 lowest energy crystal packings obtained have been predicted and analysed .

Polymorph	a	b	c	$d_{ij}^h$	$d_{ij}^e$	Space group	density	$\Delta E$
structure 0	16.75	9.63	53.95	3.4	3.1	$P2_12_12_1$	1.381	0.00
structure 1	19.26	18.97	22.80	4.9	2.6	$P2_12_12_1$	1.441	1.5
structure 2	18.97	31.92	13.65	3.45	3.2	$Pna2_1$	1.454	7.2
structure 3	12.85	40.54	15.77	4.3	3.4	$P2_12_12_1$	1.463	7.7
structure 4	9.68	31.63	32.71	3.5	3.0	$P2_12_12_1$	1.200	20.7

Table 4.2: Computed cell parameters (a, b, c, Å ), shortest distance between donor ( $d_{ij}^h$ , Å) and acceptor groups ( $d_{ij}^e$ , Å), densities (D, g/cm<sup>3</sup>) and relative stabilities ( $\Delta E$ , kcal/mol) for the five different crystalline polymorphs. All reported values refer to polymorphs fully optimised at the B3LYP-D3/opt. basis level. All space groups are orthorombic so all unit cell angles are 90°.

In Table 4.2 unit cell data for the crystals identified after full geometry optimization at the DFT level is reported. The structures belong to the  $P2_12_12_1$  symmetry group (structure 0 –i.e. the most stable–, 1, 3, 4) and  $Pna2_1$ (structure 2). At this level, all the extracted polymorphs are within a range of about 20 kcal/mol from the most stable structure, taken as reference. DFT energy differences between the polymorphs considered are rather pronounced. Based on these values in fact, the probability to populate any of the structures beyond polymorph 1 is absolutely negligible. Nonetheless, one has to consider that in actual thin films several polymorphs could co-exist due to the experimental conditions of deposition, which could favour the nucleation of a particular structure over another and achieve stability thanks to large kinetic barriers. At the same time, an incertitude of about 3 kcal/mol in the stabilities should be expected due to the level of theory<sup>[167][168]</sup>. As a consequence, all these polymorphs will be discussed in some details, starting from their structural features.

Ambipolar conduction means that, for the dyad, the most desirable packing should arise from

a balance between donor and acceptor competing arrangements. The quantity responsible for the differences in transport efficiency is the magnitude of the transfer integrals,  $J_{ij}$ . This magnitude is a function of the orbital overlap between the two moieties involved in the charge transfer. The relative distance between exchanging moieties,  $d_{ij}$ , is the most natural index in term of structure, but other, more complex, geometrical features controlling the integrals also emerge, as it will be shown. Among these important quantities are the angle between approximate conjugation planes of donor moieties and their relative shift. A detailed analysis of the polymorphs obtained can give more precise examples of these geometric features in the particular case of DPP-Ful, but results can easily be generalised since many characteristics are common to other dyads and, more in general, to photovoltaic materials.

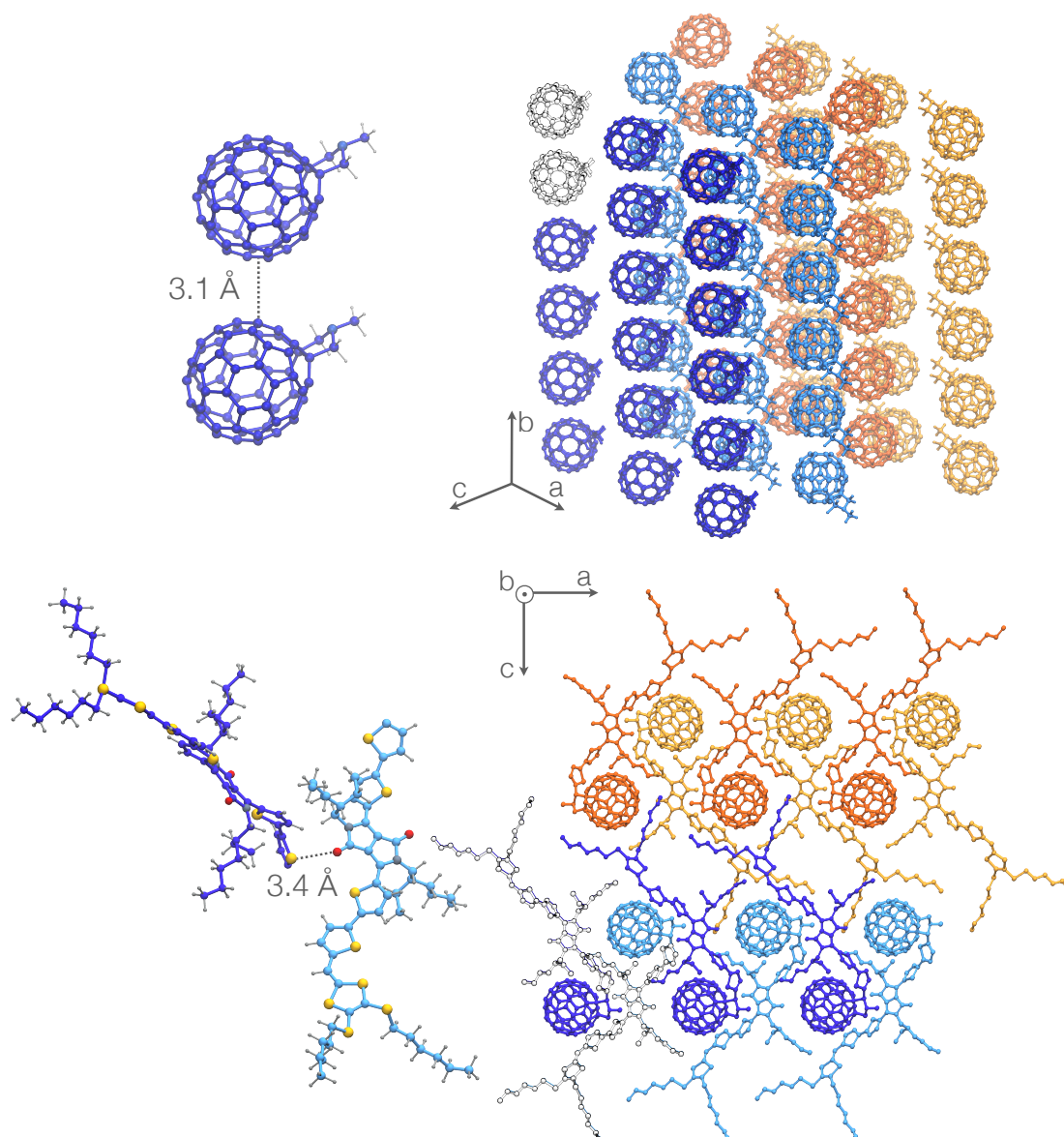


Figure 4.3: Structural features of the most stable polymorph 0 obtained after a full DFT optimisation: the shortest distance between fullerene pairs and the distribution of acceptor moieties (*top*), the shortest distance between DPP pair and a view of the herringbone structures in the *ac*-plane (*bottom*).

The optimised structure of the most stable polymorph (0), belongs to the orthorhombic  $P2_12_12_1$  space group and features four molecules in the asymmetric unit. In the supercell these molecules are arranged according to a double herringbone in the *ac*-plane of the crystal, as shown in Fig. 4.3. These two herringbones are identical but have opposite orientation, i.e. along the positive and negative directions of crystal axis *a*. The minimum approach

distance for donor moiety dimers is  $d_{ij} = 3.4 \text{ \AA}$  and is achieved for consecutive molecules belonging to the same herringbone (Fig. 4.3 lower-left). Layers are then stacked along  $b$ , where fullerenes form columns acting as conducting channels for electrons. The distance between fullerenes pairs in consecutive stacking planes is of  $3.1 \text{ \AA}$  ( $10.3 \text{ \AA}$  centre-to-centre). The closest contacts are achieved in the stacking direction for fullerenes, as well as in the orthogonal plane ( $bc$ ) for DPP molecules.

Current experimental characterisations of DPP-Ful offer limited information about the molecular details of packing, this is precisely the reason behind this computational study. However, it is important to test the agreement between the limited structural data available and the simulated data. Structural data from ref. 87 can be extracted from an X-ray diffraction (XRD) pattern. Direct comparison with this pattern has shown that polymorph 0, also offers the best over-all agreement with the experimental data despite an inconsistency with the highest peak in the low-angle region. The predicted patterns for all polymorphs investigated before and after B3LYP/D3 optimisation are available in Fig. 4.4. It is also interesting to notice that the most stable polymorph is not the one with the highest density (see Table 4.2) suggesting that dispersion-driven interactions between DPP-moieties are able to confer a higher stability and that these moieties play a key role in stabilising the packing from a thermodynamic point of view.

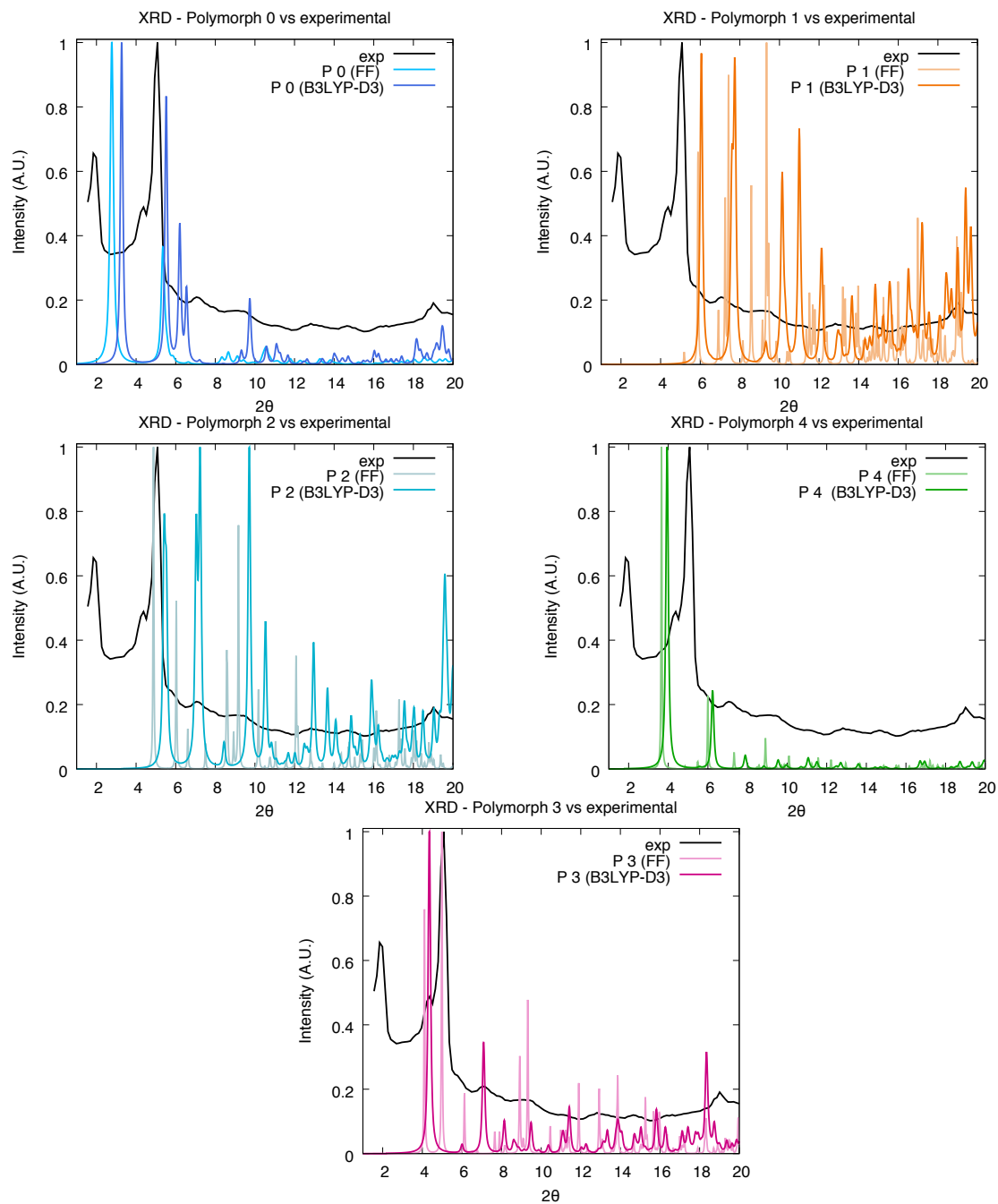


Figure 4.4: XRD patterns for all the considered polymorphs. The two superimposed spectra have been obtained from the force-field structure (FF) and the B3LYP-D3 refinement.

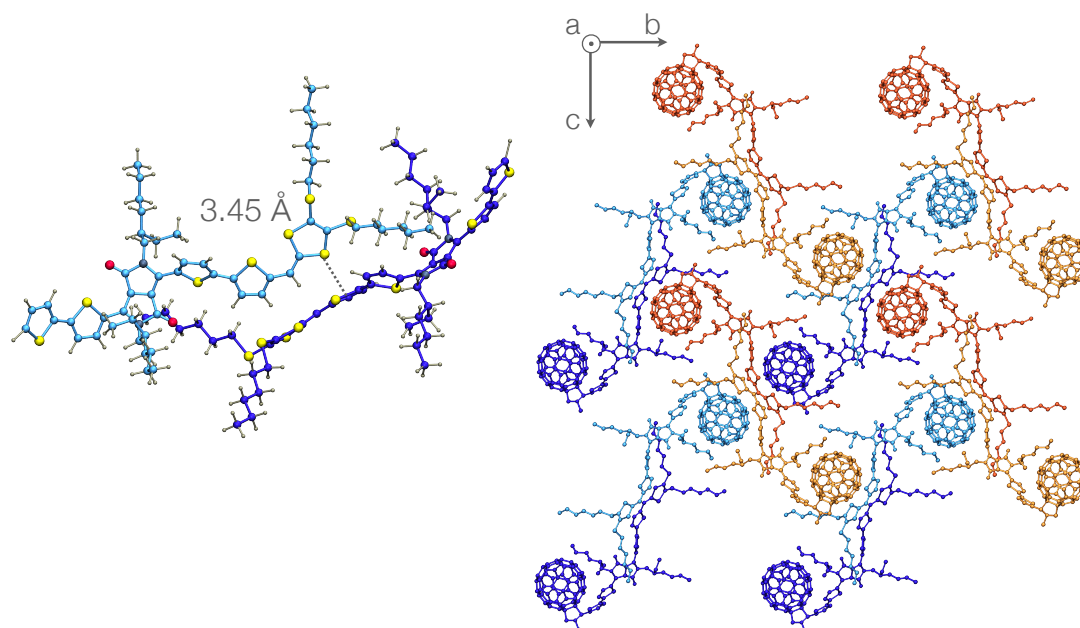


Figure 4.5: Structural features of the polymorph 1 obtained after a full DFT optimisation: the shortest distance between DPP pairs moieties with the largest orbital overlap for the structure (*bottom*) and a view of the crystal motif along the bc-plane (*left*).

The optimised motif of the next most stable packing, polymorph 1, features a structure in which fullerenes are distributed in a regular lattice in the bc-plane, with the space in between occupied by a close-knitted donor moiety matrix (Fig. 4.5, right). Similar planes are then stacked in the a direction where the closest approach between fullerenes belonging to stacked planes is achieved with a distance of  $d_{ij} = 2.9 \text{ \AA}$  allowing rather large values of  $J_{ij}$ .

The donor structure across the planes is composed of a network of DPP moieties with their backbones arranged almost perpendicularly so that no  $\pi$ -stacking is observed for DPP moieties in close proximity (see Fig 4.5, left). The packing is rather efficient and confers to the polymorph a density of  $1.443 \text{ g/cm}^3$ . The closest approach distance between DPP pairs is rather large,  $d_{ij} = 4.9 \text{ \AA}$ , and does not allow efficient transport of holes within the bc-plane nor across planes, along direction a.

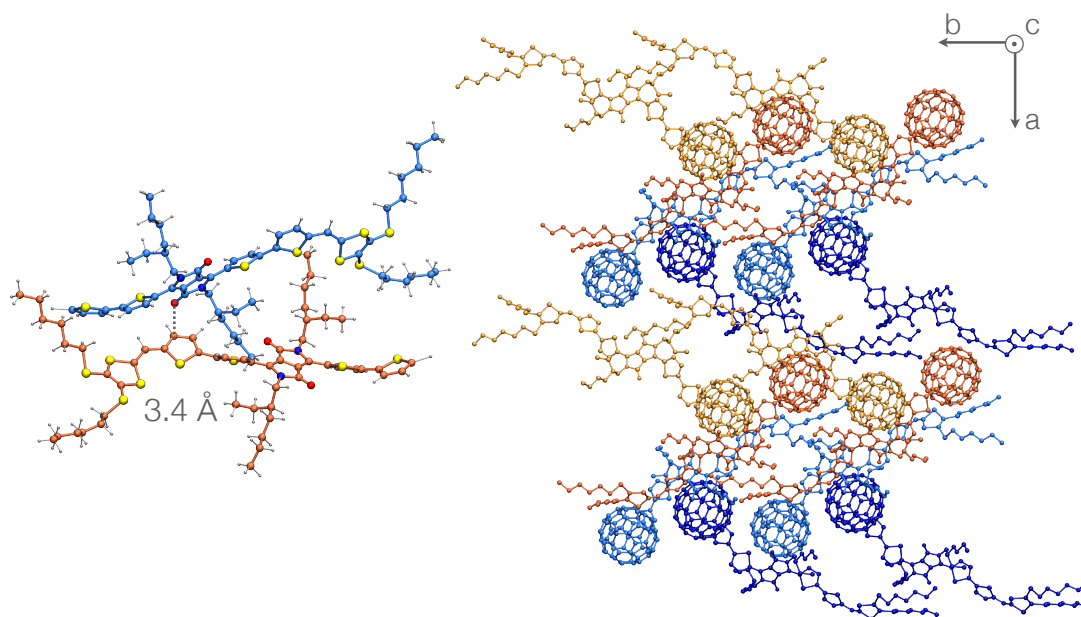


Figure 4.6: Structural features of the polymorph 2 obtained after a full DFT optimization: the shortest distance between for a DPP pair (*left*) and a view of the bc-plane (*right*).

The crystal motif of polymorph 2 presents one of the most efficient packings in the set. In the *a* direction fullerene moieties are arranged again in separated columns that constitute the backbone of two repeated herringbone structures in the *ab*-plane (Fig. 4.6, right). The minimum distance between a pair of DPP moieties is realised between molecules belonging to neighbouring herringbone structures along *c*, with a value of  $d_{ij}$  of 3.45 Å. The approximate conjugation planes of the pair at the point of closest approach are almost parallel and consequently the orbital overlap is large. DPP pairs in the other directions have reduced contact due to the hindrance of lateral aliphatic chains that keeps them distanced. Fullerene moieties in the backbone of the herringbone structures and stacked along *a* realise in this direction the minimum approach distance  $d_{ij}$  of 3.2 Å.

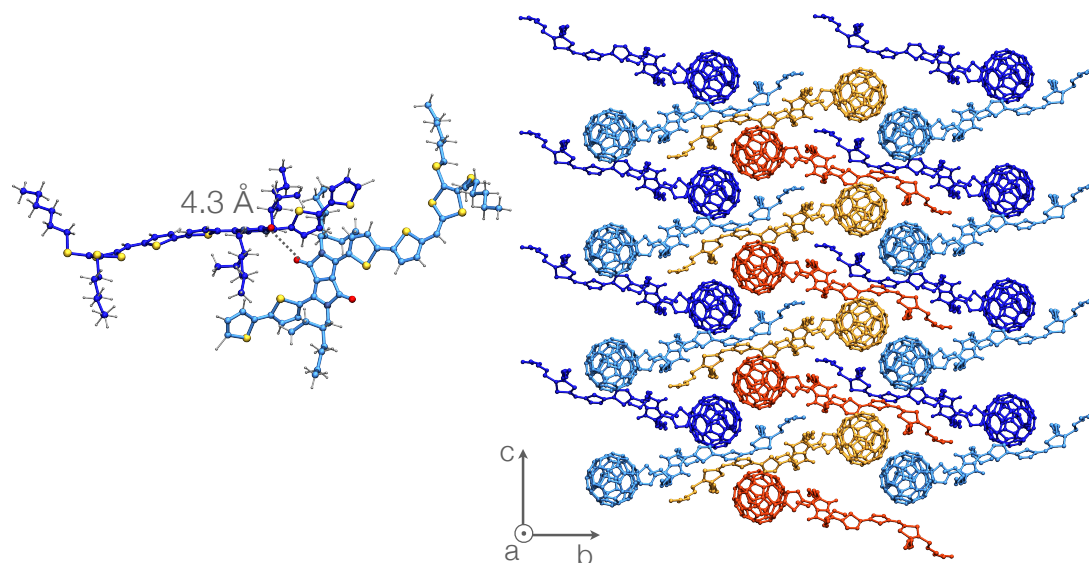


Figure 4.7: Structural features of the polymorph 3 obtained after a full DFT optimisation: the shortest distance between for a DPP pair (*left*) and a view of the bc-plane (*right*).

Polymorph 3 once again displays a motif composed by two herringbone structures, evident in the bc-plane that are then stacked along crystal axis a. In this case the two rows of molecules making up each distinct herringbone structures are more intertwined (see Figure 4.7) with respect to other similar structures in the other polymorphs. In this configuration, fullerenes are packed close to another fullerene belonging to a neighbouring herringbone structure. These pairs are then stacked along a, where column-like stacking appears again. All elements in the column reach a minimum distance of  $3.4 \text{ \AA}$ , ensuring rather large values for transfer integrals. The fact that rows belonging to the same herringbone motif are very intertwined in the bc-plane means that donor moieties remain more distant to accommodate for the fullerenes so that DPP moieties cannot reach efficient packing. The minimum distance in the bc-plane is around  $4.3 \text{ \AA}$  and the approach configuration is edge-on, that is detrimental to transfer efficiency. In the stacking direction a, the hindrance of the aliphatic chains brings the minimum approach distance at over  $9 \text{ \AA}$ , making transport along this direction completely inefficient.

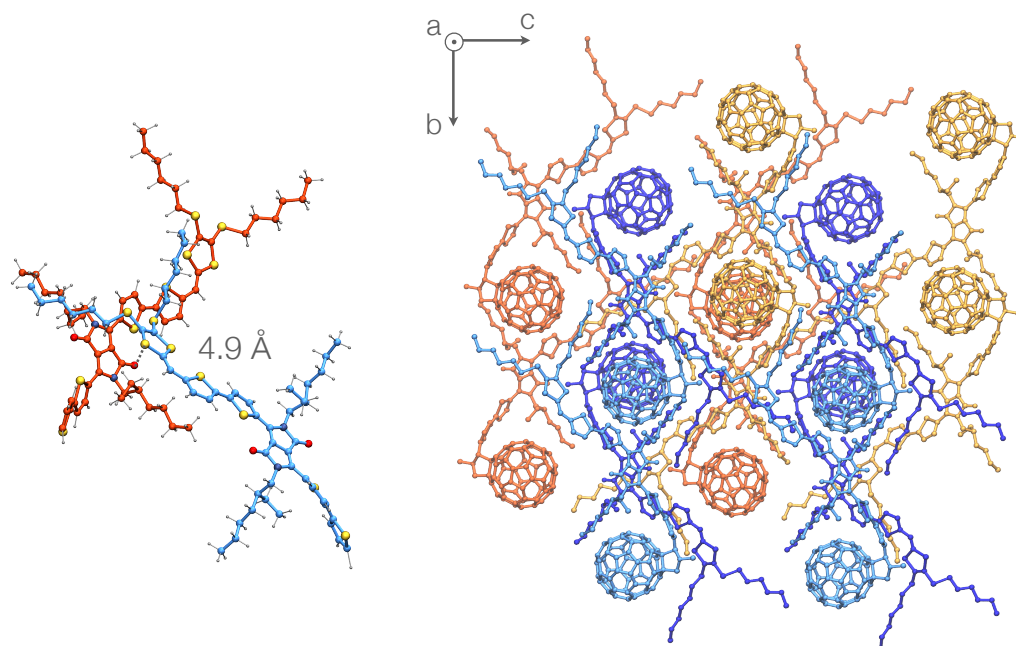


Figure 4.8: Structural features of the polymorph 4 obtained after a full DFT optimisation: the shortest distance between for a DPP pair (*left*) and a view of the bc-plane (*right*).

The structure of polymorph 4 is characterised by two herringbone motifs wedged into each other in the bc-plane and then stacked along a, as shown in Fig. 4.8. In this herringbone structure the closest approach for DPP moieties is realised between elements of different herringbone motifs (Fig. 4.8). This minimum distance is  $d_{ij} = 3.5 \text{ \AA}$  but the approach is edge-on, i.e. the approximate conjugation planes of the DPP backbones are almost perpendicular to each other. This arrangement lowers considerably the orbital overlap. The stacking along the direction a of the motif in the bc-plane results in the formation of fullerene columns or channels similar to what already observed for polymorph 1, see Fig. 4.5. The minimum approach distance for acceptor moieties in this direction is  $3.0 \text{ \AA}$ , a value small enough to allow large rates of electron transfer between fullerenes. Polymorphs 2 and 3 boast the largest densities in the set with  $1.454$  and  $1.463 \text{ g/cm}^3$  respectively.

As mentioned, the analysis of the localised structures provides valuable insight about the main features boosting or hampering transport at supramolecular level. In addition, relating packing to transport efficiency through the assessment of carrier mobilities may help identify and possibly generalise the main mechanisms at play. The results for the predicted carrier mobilities for all DFT structures are reported in Tables 4.3 and 4.4.

Polymorph	$d_{ij}^h$	$ J_{ij}^h $	$k_{ij}^h$	$\mu_h^{\text{avg}}$	$d_{ij}^e$	$ J_{ij}^e $	$k_{ij}^e$	$\mu_e^{\text{avg}}$
structure 0	3.4	$4.11 \cdot 10^{-3}$	$2.04 \cdot 10^{11}$	$2.81 \cdot 10^{-4}$	3.1	$2.71 \cdot 10^{-3}$	$3.34 \cdot 10^{11}$	$2.88 \cdot 10^{-4}$
structure 1	4.9	$2.06 \cdot 10^{-3}$	$4.38 \cdot 10^9$	$1.44 \cdot 10^{-7}$	2.6	$1.68 \cdot 10^{-2}$	$1.35 \cdot 10^{12}$	$9.12 \cdot 10^{-3}$
structure 2	3.45	$1.65 \cdot 10^{-2}$	$4.18 \cdot 10^{11}$	$1.64 \cdot 10^{-1}$	3.2	$2.57 \cdot 10^{-2}$	$2.15 \cdot 10^{12}$	$1.25 \cdot 10^{-1}$
structure 3	4.3	$4.64 \cdot 10^{-3}$	$1.91 \cdot 10^{10}$	$1.32 \cdot 10^{-6}$	3.4	$2.13 \cdot 10^{-2}$	$2.45 \cdot 10^{12}$	$7.74 \cdot 10^{-1}$
structure 4	3.5	$3.56 \cdot 10^{-4}$	$1.32 \cdot 10^8$	$1.12 \cdot 10^{-10}$	3.0	$2.76 \cdot 10^{-2}$	$4.93 \cdot 10^{12}$	$9.12 \cdot 10^{-6}$
amorphous	-	$2.50 \cdot 10^{-3}$	$8.38 \cdot 10^{11}$	$2.29 \cdot 10^{-6}$	-	$3.02 \cdot 10^{-3}$	$7.03 \cdot 10^{11}$	$2.32 \cdot 10^{-9}$

Table 4.3: Data on hole transport and electron transport  $d_{ij}$  in Å,  $J_{ij}$  in eV,  $k_{ij}$  in  $\text{s}^{-1}$ ,  $\mu$  in  $\text{cm}^2/\text{V} \cdot \text{s}$ . All reported values are obtained using B3LYP-D3 optimised structures.

The most stable polymorph (0) is also the one with performances in better agreement with experimental values<sup>[87]</sup> for both electrons and holes. Transport takes place mainly along the a-direction for holes while transport across different planes, i.e. along c, is strongly suppressed. In the ac-plane the configuration of the closest exchanging pair allows a rather large coupling element,  $J_{ij} = 4.11 \cdot 10^{-3}$  eV, yielding a Marcus rate of  $2.04 \cdot 10^{11} \text{ s}^{-1}$ . This rather large orbital overlap is ensured by the proximity of the conjugated backbone of one exchanging moiety to the diketopyrrolopyrrole unit of the second. The overall mobility along a reaches  $\mu_a(h) = 4.86 \cdot 10^{-4} \text{ cm}^2/\text{V} \cdot \text{s}$ , with the herringbone structures acting as main transport channels. Along crystal axis c on the same plane transport is significantly less efficient due to a smaller coupling between DPP moieties belonging to different herringbone structures,  $J_{ij} = 4.11 \cdot 10^{-4}$  eV giving  $\mu_c(h) = 2.84 \cdot 10^{-7} \text{ cm}^2/\text{V} \cdot \text{s}$ . In the stacking direction, corresponding to crystal axis b, the hole mobility is very low  $\mu_b(h) = 4.8 \cdot 10^{-11} \text{ cm}^2/\text{V} \cdot \text{s}$ . Conversely, along this direction, i.e. along the fullerene channels, the largest value for electron mobility is observed  $\mu_b(e) = 4.99 \cdot 10^{-4} \text{ cm}^2/\text{V} \cdot \text{s}$ , while being negligible in the other directions. As remarked above, this packing is not the most dense, yet its structure is able to maximise dispersion interactions by allowing a pronounced interdigitation of DPP moieties that ultimately yields the largest stability.

Comparison with the experimental data,  $\mu_{\text{exp}}(e) = 1.1 \cdot 10^{-4} \text{ cm}^2/\text{V} \cdot \text{s}$ ,  $\mu_{\text{exp}}(h) = 1.3 \cdot 10^{-4} \text{ cm}^2/\text{V} \cdot \text{s}$ , reveals that mobility predictions produced according to the protocol  $\mu_{\text{avg}}(e) = 2.88 \cdot 10^{-4} \text{ cm}^2/\text{V} \cdot \text{s}$ ,  $\mu_{\text{avg}}(h) = 2.81 \cdot 10^{-4} \text{ cm}^2/\text{V} \cdot \text{s}$  are able to reproduce the behaviour of the material experimentally observed. Estimates for both charge carriers are roughly 2.8 times larger than experimental mobilities but the order of magnitude and the relative values be-

tween holes and electrons are compatible with the observations<sup>87</sup>. This difference in the absolute values is to be expected given the fact that the procedure employed is not able to probe morphologies at all relevant scales but relies on an extrapolation procedure. In the intervening length scales up to the  $\mu\text{m}$  scale, many effects are to be expected in a real-life device that can lower the value of mobility with respect to an ideal periodic structure. It is however important to stress that the estimate presented here is still accurate enough to give an idea of the possible macroscopic performance and offers, despite these approximations, a rather solid way to link the performance of the macroscopic device to interesting microscopic details with atomistic resolution. A typical real-life device operates in a range of scales which goes from the thin film thickness (100 nm) to the cm scale. This means that charges are required to be transported over large distances and other effects (e.g. electrodes, interfaces, higher-scale morphology of the active layer) that lie outside the range of the treatment presented here may affect the overall transport efficiency.

It remains interesting to analyse the details of transport also for the other polymorphs. For example, polymorph 1 exhibits a much more unbalanced transport behaviour. Electron transport is more efficient than polymorph 0 given the closer packing in the a direction, and again only takes place along this axis. The minimum distance between two fullerenes belonging to different bc-planes is only 2.6 Å. This allows a large transfer integral,  $J_{ij} = 1.68 \cdot 10^{-2}$  eV and a large exchange rate giving a mobility of  $\mu_a(e) = 1.58 \cdot 10^{-2} \text{cm}^2/\text{V} \cdot \text{s}$ . Despite the proximity of DPP moieties in the close-knitted donor structure, the backbones in the closest exchanging pair cross almost orthogonally, resulting in a limited overlap of orbitals and low transport efficiency across the bc-plane with mobilities  $\mu_b(h) = 1.28 \cdot 10^{-7} \text{cm}^2/\text{V} \cdot \text{s}$  and  $\mu_c(h) = 8.18 \cdot 10^{-8} \text{cm}^2/\text{V} \cdot \text{s}$ , several orders of magnitude lower than the electronic one.

The crystal motif of polymorph 2 is the one in the set able to reach the best compromise between the packings of the two moieties and shows very large transport efficiencies for both carriers ( $\mu_a(e) = 2.16 \cdot 10^{-1} \text{cm}^2/\text{V} \cdot \text{s}$  and  $\mu_c(h) = 2.84 \cdot 10^{-1} \text{cm}^2/\text{V} \cdot \text{s}$ ). Optimal transport occurs in orthogonal directions for holes and electrons, respectively along c and a. This means that electrons move preferentially along the fullerene channels that are aligned along a, while holes move preferentially within the plane perpendicularly to the direction of the herringbone structures (see Fig. 4.6).

Polymorph 3 instead, offers an example of another limiting case. Fullerenes are optimally

packed and can transport electrons efficiently, reaching very large mobilities compared to the standard of organic photovoltaics materials, the predicted value is as large as  $1.34\text{cm}^2/\text{V}\cdot\text{s}$  in the a direction, while in the other two directions transport is absolutely negligible. Donor moieties on the other hand have reduced orbital overlap, with the largest value of the transfer integral being  $J_{ij} = 4.64 \cdot 10^{-3}$  eV and largest hole mobilities in the order of  $10^{-6}\text{cm}^2/\text{V}\cdot\text{s}$ . Polymorph 4 structure displays low transport efficiencies for both carriers. While also in this case the stacking along a gives rise to channels of fullerenes for electron transport, the larger distance compared to polymorph 1 and the configuration of the pairs with the closest approach translate in a smaller electron mobility,  $\mu_a(e) = 1.58 \cdot 10^{-5}\text{cm}^2/\text{V}\cdot\text{s}$  along the direction of the fullerene stacking that is negligible in the other orthogonal directions. DPP pairs in closest proximity have a shortest distance of  $3.5 \text{ \AA}$  which is comparable to the one found in polymorph 0 but the particular configuration of the exchanging pair makes the orbital overlap sensibly smaller ( $J_{ij} = 3.56 \cdot 10^{-4}$  eV) and results in very small mobilities along all directions, the largest being  $\mu_c(h) = 6.88 \cdot 10^{-11}\text{cm}^2/\text{V}\cdot\text{s}$ .

Polymorph	$\mu_a(e)$	$\mu_b(e)$	$\mu_c(e)$	$\mu_a(h)$	$\mu_b(h)$	$\mu_c(h)$
structure 0	$1.00 \cdot 10^{-6}$	$4.99 \cdot 10^{-4}$	$1.17 \cdot 10^{-11}$	$4.86 \cdot 10^{-4}$	$4.80 \cdot 10^{-11}$	$2.84 \cdot 10^{-7}$
structure 1	$1.58 \cdot 10^{-2}$	$7.56 \cdot 10^{-11}$	$1.46 \cdot 10^{-10}$	$1.98 \cdot 10^{-7}$	$1.28 \cdot 10^{-7}$	$8.18 \cdot 10^{-8}$
structure 2	$2.16 \cdot 10^{-1}$	$2.15 \cdot 10^{-11}$	$1.11 \cdot 10^{-4}$	$3.80 \cdot 10^{-7}$	$7.04 \cdot 10^{-10}$	$2.84 \cdot 10^{-1}$
structure 3	$1.34 \cdot 10^0$	$8.90 \cdot 10^{-13}$	$1.64 \cdot 10^{-9}$	$8.47 \cdot 10^{-10}$	$9.09 \cdot 10^{-10}$	$2.28 \cdot 10^{-6}$
structure 4	$1.58 \cdot 10^{-5}$	$3.08 \cdot 10^{-11}$	$4.51 \cdot 10^{-11}$	$5.68 \cdot 10^{-11}$	$1.72 \cdot 10^{-10}$	$6.88 \cdot 10^{-11}$

Table 4.4: Electron and hole mobilities along all crystal axes a, b and c for the polymorphs discussed. All reported values are in  $\text{cm}^2/\text{V}\cdot\text{s}$  and are obtained using the B3LYP-D3 optimised structures.

The comparison carried out offers an overview of the consistently different behaviours that polymorphs of a same (complex) molecule can have and more in general of the fundamental role played by supramolecular organisation. Nonetheless, the main goal remains to prove the effectiveness of computational approaches in complementing and interpreting experimental data. Indeed, from the present analysis, DPP-Ful reveals a dominant crystalline form that is thermodynamically favoured over the others. This is consistent with data reported in the experimental reference<sup>87</sup>, suggesting the presence of “long-range ordering” in photoactive layers made with this material. These results suggest that the computational approach im-

plemented is able to effectively link the general microscopic features of the crystal form observed in experiments providing a direct picture of the molecular packing responsible for the large reported efficiency of DPP-Ful-based devices.

### 4.3.2 Amorphous phase

After the discussions of the most probable crystal structures that serve as indicators of possible local order emerging in thin films, the analysis of the amorphous phase is in order. Amorphous configurations remain interesting for two main reasons. First, amorphous regions may coexist with more ordered ones and contribute to the overall performance of the device. Second, completely amorphous films are generally more convenient to produce compared to polycrystalline or crystalline ones<sup>207</sup>. As already remarked, the opposite is true in simulations, where the amorphous phase is more challenging to model compared to the ordered one. In fact, the absence of long-range order makes it formally inaccurate to apply PBC. This requires the production of a significant number of configurations with relatively large amounts of molecules in order to have reliable estimates of the structural effects affecting the mobility (no border effects). Following the approach described in the computational details, configurations of 500 molecules in cells whose linear size is roughly 106 Å after convergence of the volume were produced.

For all sufficiently close molecular pairs the transfer integrals and the associated rates were computed. Naturally, this step of the calculation is more expensive in this case. In ordered phases periodicity limits the number of possible pair configurations and only a small set of rates repeated over the lattice is sufficient. Mobility estimates were computed for every configuration extracted. Disordered systems are to a good extent isotropic, so different directions of the applied electric field can be considered in order to collect some statistics on mobility, results are reported in Table 4.3. Amorphous mobilities show a marked difference between the two charge carriers. The reason can be deduced from the analysis of the pair distribution functions  $g(r)$  for acceptor and donor moieties. The pair distribution function is defined according to the following:

$$g(r) = \frac{N(r)}{4\pi r^2 \rho_{\text{ideal}}} \quad (4.3)$$

Where  $N(r)$  is the number of molecules with distance  $r$  from a given molecule and the de-

nominator is the linear density of an ideal gas with the same total density  $\rho_{\text{ideal}}$  of the cell. Peaks and troughs of the distribution indicate deviations with respect to the ideal gas behaviour. They reveal how the geometry and chemical character of the material may introduce some degree of order at supramolecular scale.  $g(r)$  has been calculated for both moieties separately. For each moiety a point is chosen from which to compute distances according to their respective characteristics. Fullerene moieties are symmetric enough for the centroid to be a sensible choice while diketopyrrolopyrrole moieties have a more complex geometry. For this reason, the relevant point selected is the centre of charge of the donor moiety in its positively charged state. Pair distribution functions for both moieties are reported in the plot in Fig. 4.9.

Complementing the discussion of Fig. 4.9 with data for the amorphous phase reported in Table 4.3 gives us useful insight in the behaviour of DPP-Ful in disordered morphologies. The first peak at around 7.5 Å in Fig. 4.9 is an indication that fullerenes tend to attract each other and form small clusters with a rather efficient packing and high exchange rates reaching  $10^{11} \text{ s}^{-1}$ . The depletion zone following this first peak is a sign that the donor moieties attached to the fullerenes have more hindrance and require a certain volume around the cluster to be accommodated. This more or less regular alternation of clusters and regions occupied by donor moieties causes the amorphous material to have a poor performance in terms of electron transport as electrons are very unlikely to be able to move across neighbouring clusters and hence remain trapped. The difficulty of donor moieties in assembling due to the hindrance of aliphatic chains and their linear geometry results instead in a more favourable morphology for hole transport. The structure is sufficiently intertwined and homogeneous to achieve non-negligible transport performances. Electronic couplings between neighbouring molecules have an average magnitude of  $10^{-3} \text{ eV}$  (see Table 4.3) and the homogeneous structures allows an average transport rate of  $10^{11} \text{ s}^{-1}$ . These structural features are reflected in the values of mobilities. Thanks to conformational disorder, holes can achieve mobilities of  $\mu_{\text{am}}(h) = 2.29 \cdot 10^{-6} \text{ cm}^2/\text{V} \cdot \text{s}$  on DPP moieties, a value significantly larger than the estimated mobilities for polymorphs 1, 3 and 4 (see Table 4.3). Conversely, due to the relative ease with which fullerene moieties are able to assemble, clusters severely affect the electron transport efficiency of the amorphous medium with a very low value of  $\mu(e) = 2.32 \cdot 10^{-9} \text{ cm}^2/\text{V} \cdot \text{s}$ , not comparable with any of the crystal polymorphs studied

exhibiting, on average, far larger mobilities for electrons.

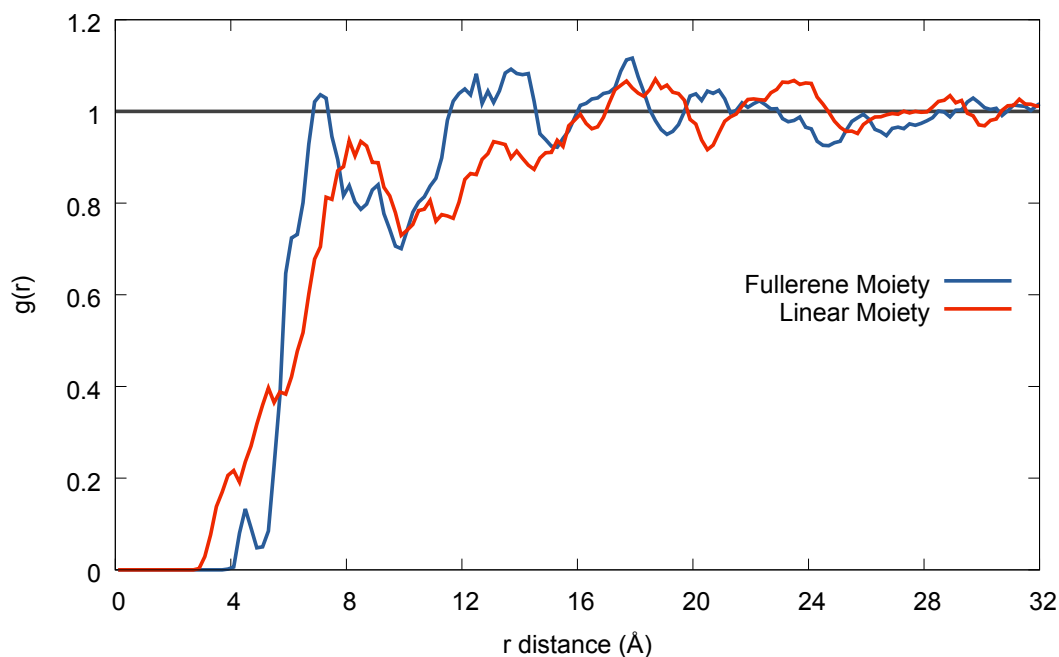


Figure 4.9: Radial Pair distribution functions for the donor (red) and acceptor (blue) moieties of DPP-Ful.

## 4.4 Conclusions

This investigation has allowed a molecular-level characterisation of the packing that may likely be responsible for the transport properties of DPP-Ful active layers reported in ref. [87](#). The comparison of transport efficiencies for both carriers in the different polymorphs extracted enabled the outlining of some general features that might be well applicable to other dyads and hence prove useful in directing future experimental work. For example, functionalisation with aliphatic chains to donor moieties has been shown to improve solubility and processability of the material [187](#)[188](#)[189](#)[190](#) but it also makes more difficult for DPP moieties to achieve efficient packing. Despite the possibility for these chains to promote order at ambient temperature due to steric hindrance, the analysis of the predicted structures suggests that they introduce stringent constraints to the packing of donor moieties, considerably hindering the  $\pi$ - $\pi$  stacking and hence transfer efficiencies between molecules.

At the same time, their presence on the diketopyrrolopyrrole unit seems to promote the inter-

action with the fullerene moiety so as to enhance the relative insulation of donor and acceptor moieties by diminishing the  $\pi$  conjugation of the linker. Clearly, these effects might be overestimated by the method used and in particular by the description of dispersion forces. However, even assuming a substantial geometric change of aliphatic chains in the experimental crystal structure their effect could remain important. Indeed, a modulation of their length may very well lead to dyads with better stacking properties of donor moieties while maintaining good stability of the crystal structure at ambient temperature and good solubility. In addition, it has been found that in general fullerene moieties and donor moieties do compete for optimal packing. This means that not all stable polymorphs have the same efficiency in transporting holes or electrons unless an equilibrium is reached against these mechanisms. This fact results crucially in a highly directional carrier transport that is not, in general, a desirable feature for polycrystalline thin films, with many randomly oriented ordered regions coexisting between which carriers should be able to cross as swiftly as possible. Moreover, holes and electrons in packings exhibiting high transport efficiencies tend to be optimally conducted in directions orthogonal to each other. This is possibly due to the fact that fullerenes are rather large molecules and, when stacked in columns determine orthogonal planes with considerable spacing between them. Competing clustering of fullerene and donor moieties emerges also in the amorphous phase, an indication that the typical hurdles linked to fullerene-derivatives in bulk heterojunction blends are also transferred to molecular heterojunctions. A number of these features can be extrapolated to a substantial degree to the larger class of organic photovoltaics dyads. This demonstrates the validity of approaches able to predict molecular level properties and more importantly, to complement it with information about packing at the supramolecular level. The latter task remains one of the most delicate steps, in an ideal implementation an appropriate description including disorder and effects of morphologies at higher scales, through some models at larger scale, would allow more realistic predictions, fundamental in providing an even more accurate prediction of photovoltaic performance.

# Chapter 5

## Conclusions

It is difficult to underestimate the role that computational protocols for materials discovery are expected to play in the coming years<sup>[10][129][208][209]</sup>.

At present, the development of *in silico* protocols is at an early stage. Their use is still limited to complementing the experimental endeavour rather than fully driving the search for new compounds in the chemical space<sup>[12]</sup>. In order to get there, it is necessary to perform an intermediate step in which the microscopic mechanisms governing the behaviour of organic semiconductors are revealed. This is the context in which the current work has been set.

The protocol employed here is the combination of different methods aimed at the evaluation of microscopic properties known to be predictive of photovoltaic efficiency. These methods were developed to investigate time and length scales that are often below the typical ones concerned with photovoltaic behaviour. Hence, the purpose of this work has been to extrapolate the description of the system provided by these methods at scales larger than the molecular one while retaining every relevant microscopic detail.

The absorption behaviour of a small-molecule donor has been investigated in chapter 3. The simulation of the effects of the aggregated phase has allowed the identification of the solid state structures responsible for the reported absorption spectrum. The protocol has successfully identified the role of self-organisation driven by dipolar interactions and has revealed the presence of geometric features impacting the electronic structure that are very sensitive to the environment. The microscopic picture reconstructed has been able to describe the effects of the thermal treatment on the emergence of crystalline domains within the thin

film. It has also clarified the manner in which different polymorphs compete within the solid phase. Thanks to the emergence of some highly dominant variables governing the described behaviour, it has been quite straightforward to extrapolate these findings to other molecular systems sharing the same characteristics. In addition, the evaluation of charge transport properties has also served to elucidate how variable crystalline order impacts free carrier mobilities and how the simultaneous presence of different structures affects the overall transport efficiency.

Part of the same protocol has been applied to simulate the behaviour of the DPP-Ful dyad in chapter 4. This material has been reported to reach a PCE of 2.2% in some experimental SMOSCs<sup>[87]</sup>. For DPP-Ful, the focus has been shifted on the relation between charge transport and solid state packing. The goal has been to investigate the implications of polymorphism, a common aspect in organic solids<sup>[131]</sup>, on charge transport for active layers characterised by the coexistence of multiple solid phase structures. Once again, the protocol has been able to identify the most plausible microscopic picture associated with the observed behaviour. The computational analysis has revealed general effects associated with the presence of common functional groups. The interplay between molecular structure and dispersion interactions, playing a key role in organic molecular assemblies, has been uncovered. A competition between the packing mechanisms of *D* and *A* moieties has also emerged that could be expected to be present in many other dyads with *A* moieties based on fullerene derivatives.

The studies presented have proven the predictive power of the protocol based on the application of fundamental methods, even when they are extrapolated at scales larger than the molecular one. Being a part of this early-stage effort in development, both examples have relied heavily on experimental observations. The protocol has successfully expanded the comprehension of the behaviour of the systems analysed and the simulated data have provided a microscopic view that has allowed the explanation of the different observations under a unified molecular picture.

These promising results will naturally prompt additional studies to assess the performance of the same protocol on a larger set of systems that capture more fully the variety of conditions relevant to organic photovoltaics. For instance, studies on the supramolecular organisation at *D/A* interfaces could greatly aid the optimisation of heterojunctions. The same should

be true for the interfaces between photoactive materials and the electrodes, or between the buffer layers that are often present in organic solar devices.

In conclusion, research in organic semiconductors will benefit from the development of protocols<sup>210</sup> similar to the one employed in this work. These protocols are essential to tackle the complex phenomena<sup>211</sup> produced by the collective behaviour of molecules, emerging in organic solids. This effort is fundamental to the development of organic technologies that are currently being investigated as possible answers to many global challenges such as the optimisation of energy production and storage<sup>12,37</sup>. For what concerns organic solar cells, this optimisation coincides with the synthesis of materials with large PCEs that are easier and cheaper to fabricate<sup>212</sup> to meet the increasing energy demand across the globe. The deployment of these computational tools to look for better performing organic photovoltaic compounds would also generate new data enabling a deeper understanding<sup>213</sup> of the theory behind this class of functional materials. Through an iterative process, this could lead to refine the theoretical framework and ultimately to an automated identification of photovoltaic candidates leading to a new generation of organic solar cells representing a more versatile and effective alternative to silicon technologies.

# Bibliography

- [1] P. Ertl, *Journal of chemical information and computer sciences* **43**, 374 (2003).
- [2] K. L. Drew, H. Baiman, P. Khwaounjoo, B. Yu, and J. Reynisson, *Journal of Pharmacy and Pharmacology* **64**, 490 (2012).
- [3] P. S. Gromski, A. B. Henson, J. M. Granda, and L. Cronin, *Nature Reviews Chemistry* **3**, 119 (2019).
- [4] S. Fratini, S. Ciuchi, D. Mayou, G. T. De Laissardière, and A. Troisi, *Nature materials* **16**, 998 (2017).
- [5] P. Friederich, A. Fediai, S. Kaiser, M. Konrad, N. Jung, and W. Wenzel, *Advanced Materials* **31**, 1808256 (2019).
- [6] C. J. Brabec, *Solar energy materials and solar cells* **83**, 273 (2004).
- [7] W. Tress, in *Organic Solar Cells* (Springer, 2014), pp. 67–214.
- [8] J.-L. Bredas and J. R. Durrant, *Organic photovoltaics* (2009).
- [9] A. N. Sokolov, S. Atahan-Evrenk, R. Mondal, H. B. Akkerman, R. S. Sánchez-Carrera, S. Granados-Focil, J. Schrier, S. C. Mannsfeld, A. P. Zoombelt, Z. Bao, et al., *Nature communications* **2**, 437 (2011).
- [10] J. Hachmann, R. Olivares-Amaya, S. Atahan-Evrenk, C. Amador-Bedolla, R. S. Sánchez-Carrera, A. Gold-Parker, L. Vogt, A. M. Brockway, and A. Aspuru-Guzik, *The Journal of Physical Chemistry Letters* **2**, 2241 (2011).
- [11] A. Jain, Y. Shin, and K. A. Persson, *Nature Reviews Materials* **1**, 1 (2016).
- [12] D. P. Tabor, L. M. Roch, S. K. Saikin, C. Kreisbeck, D. Sheberla, J. H. Montoya, S. Dwaraknath, M. Aykol, C. Ortiz, H. Tribukait, et al., *Nature Reviews Materials* **3**, 5 (2018).
- [13] D. Chen, A. Nakahara, D. Wei, D. Nordlund, and T. P. Russell, *Nano letters* **11**, 561 (2011).
- [14] R. W. Cahn, in *The Coming of Materials Science* (Pergamon, 2001), vol. 5 of *Pergamon Materials Series*, pp. 253 – 304.
- [15] J.-L. Brédas, D. Beljonne, V. Coropceanu, and J. Cornil, *Chemical reviews* **104**, 4971 (2004).
- [16] Y. Li, V. Coropceanu, and J.-L. Brédas, *Charge Transport in Crystalline Organic Semiconductors* (2010), chap. Chapter 7, pp. 193–230.
- [17] H. Bässler and A. Köhler, *Charge Transport in Organic Semiconductors* (Springer Berlin Heidelberg, Berlin, Heidelberg, 2012), pp. 1–65.
- [18] L. J. A. Koster, S. E. Shaheen, and J. C. Hummelen, *Advanced Energy Materials* **2**, 1246 (2012).
- [19] J. E. Donaghey, A. Armin, P. L. Burn, and P. Meredith, *Chemical Communications* **51**, 14115 (2015).
- [20] A. C. Mayer, S. R. Scully, B. E. Hardin, M. W. Rowell, and M. D. McGehee, *Materials today* **10**, 28 (2007).

- [21] G. Chamberlain, *Solar cells* **8**, 47 (1983).
- [22] C. W. Tang, *Applied physics letters* **48**, 183 (1986).
- [23] P. Heremans, A. K. Tripathi, A. de Jamblinne de Meux, E. C. Smits, B. Hou, G. Pourtois, and G. H. Gelinck, *Advanced Materials* **28**, 4266 (2016).
- [24] W. Tress, in *Organic Solar Cells* (Springer, 2014), pp. 67–214.
- [25] A. J. Heeger, *Advanced Materials* **26**, 10 (2014).
- [26] M. C. Scharber and N. S. Sariciftci, *Progress in polymer science* **38**, 1929 (2013).
- [27] S. H. Park, A. Roy, S. Beaupre, S. Cho, N. Coates, J. S. Moon, D. Moses, M. Leclerc, K. Lee, and A. J. Heeger, *Nature photonics* **3**, 297 (2009).
- [28] G. Dennler, M. C. Scharber, and C. J. Brabec, *Advanced materials* **21**, 1323 (2009).
- [29] Y. Cui, H. Yao, L. Hong, T. Zhang, Y. Tang, B. Lin, K. Xian, B. Gao, C. An, P. Bi, et al., *National Science Review* **7**, 1239 (2019), ISSN 2095-5138.
- [30] L.-M. Chen, Z. Hong, G. Li, and Y. Yang, *Advanced Materials* **21**, 1434 (2009).
- [31] H. Hoppe and N. S. Sariciftci, *Journal of Materials Chemistry* **16**, 45 (2006).
- [32] X. Yang, J. Loos, S. C. Veenstra, W. J. Verhees, M. M. Wienk, J. M. Kroon, M. A. Michels, and R. A. Janssen, *Nano letters* **5**, 579 (2005).
- [33] V. Shrotriya, G. Li, Y. Yao, T. Moriarty, K. Emery, and Y. Yang, *Advanced functional materials* **16**, 2016 (2006).
- [34] C. Riordan and R. Hulstron, in *IEEE Conference on Photovoltaic Specialists* (IEEE, 1990), pp. 1085–1088.
- [35] D. D. S. Fung and W. C. H. Choy, in *Organic solar cells: materials and device physics*, edited by W. C. H. Choy (Springer, 2012), pp. 1–17.
- [36] R. Xue, J. Zhang, Y. Li, and Y. Li, *Small* **14**, 1801793 (2018), <https://onlinelibrary.wiley.com/doi/pdf/10.1002/sml1.201801793>, URL <https://onlinelibrary.wiley.com/doi/abs/10.1002/sml1.201801793>.
- [37] R. Po and J. Roncali, *Journal of Materials Chemistry C* **4**, 3677 (2016).
- [38] H. Shirakawa, E. J. Louis, A. G. MacDiarmid, C. K. Chiang, and A. J. Heeger, *Journal of the Chemical Society, Chemical Communications* pp. 578–580 (1977).
- [39] C. K. Chiang, C. Fincher Jr, Y. W. Park, A. J. Heeger, H. Shirakawa, E. J. Louis, S. C. Gau, and A. G. MacDiarmid, *Physical review letters* **39**, 1098 (1977).
- [40] N. S. Sariciftci, L. Smilowitz, A. J. Heeger, and F. Wudl, *Science* **258**, 1474 (1992).
- [41] B. Kraabel, J. C. Hummelen, D. Vacar, D. Moses, N. Sariciftci, A. Heeger, and F. Wudl, *The Journal of chemical physics* **104**, 4267 (1996).
- [42] R. E. Peierls, *Quantum theory of solids* (Clarendon Press, 1996).
- [43] J. Roncali, *Macromolecular Rapid Communications* **28**, 1761 (2007).
- [44] J. Chen and Y. Cao, *Accounts of chemical research* **42**, 1709 (2009).
- [45] J. Gierschner, J. Cornil, and H.-J. Egelhaaf, *Advanced materials* **19**, 173 (2007).
- [46] Y.-J. Cheng, S.-H. Yang, and C.-S. Hsu, *Chemical reviews* **109**, 5868 (2009).
- [47] P. Cheng and Y. Yang, *Accounts of Chemical Research* (2020).

- [48] T. Mikie and I. Osaka, *Journal of Materials Chemistry C* (2020).
- [49] J. Roncali, P. Frere, P. Blanchard, R. de Bettignies, M. Turbiez, S. Roquet, P. Leriche, and Y. Nicolas, *Thin solid films* **511**, 567 (2006).
- [50] J. Roncali, *Accounts of chemical research* **42**, 1719 (2009).
- [51] A. Mishra and P. Bäuerle, *Angewandte Chemie International Edition* **51**, 2020 (2012).
- [52] S. Roquet, R. de Bettignies, P. Leriche, A. Cravino, and J. Roncali, *Journal of Materials Chemistry* **16**, 3040 (2006).
- [53] F. Baert, C. Cabanetos, A. Leliege, E. Kirchner, O. Segut, O. Alévêque, M. Allain, G. Seo, S. Jung, D. Tondelier, et al., *Journal of Materials Chemistry C* **3**, 390 (2015).
- [54] A. K. Pandey and J.-M. Nunzi, *Advanced Materials* **19**, 3613 (2007).
- [55] L. C. Palilis, P. A. Lane, G. P. Kushto, B. Purushothaman, J. E. Anthony, and Z. H. Kafafi, *Organic electronics* **9**, 747 (2008).
- [56] K. N. Winzenberg, P. Kemppinen, G. Fanchini, M. Bown, G. E. Collis, C. M. Forsyth, K. Hegedus, T. B. Singh, and S. E. Watkins, *Chemistry of Materials* **21**, 5701 (2009).
- [57] H. Oberhofer, K. Reuter, and J. Blumberger, *Chemical reviews* **117**, 10319 (2017).
- [58] S. D. Collins, N. A. Ran, M. C. Heiber, and T.-Q. Nguyen, *Advanced Energy Materials* **7**, 1602242 (2017).
- [59] Y. Sun, G. C. Welch, W. L. Leong, C. J. Takacs, G. C. Bazan, and A. J. Heeger, *Nature materials* **11**, 44 (2012).
- [60] T. S. Van Der Poll, J. A. Love, T.-Q. Nguyen, and G. C. Bazan, *Advanced Materials* **24**, 3646 (2012).
- [61] J. E. Coughlin, Z. B. Henson, G. C. Welch, and G. C. Bazan, *Accounts of chemical research* **47**, 257 (2014).
- [62] C. Yan, S. Barlow, Z. Wang, H. Yan, A. K.-Y. Jen, S. R. Marder, and X. Zhan, *Nature Reviews Materials* **3**, 1 (2018).
- [63] J. Hou, O. Inganäs, R. H. Friend, and F. Gao, *Nature materials* **17**, 119 (2018).
- [64] L. Krückemeier, P. Kaienburg, J. Flohre, K. Bittkau, I. Zonno, B. Krogmeier, and T. Kirchartz, *Communications Physics* **1**, 1 (2018).
- [65] J. Zhang, H. S. Tan, X. Guo, A. Facchetti, and H. Yan, *Nature Energy* **3**, 720 (2018).
- [66] Y. Firdaus, V. M. Le Corre, S. Karuthedath, W. Liu, A. Markina, W. Huang, S. Chattopadhyay, M. M. Nahid, M. I. Nugraha, Y. Lin, et al., *Nature communications* **11**, 1 (2020).
- [67] Y. He and Y. Li, *Physical chemistry chemical physics* **13**, 1970 (2011).
- [68] Q. Xie, E. Perez-Cordero, and L. Echegoyen, *Journal of the American Chemical Society* **114**, 3978 (1992).
- [69] S. Günes, H. Neugebauer, and N. S. Sariciftci, *Chemical reviews* **107**, 1324 (2007).
- [70] Y. Huang, E. J. Kramer, A. J. Heeger, and G. C. Bazan, *Chemical reviews* **114**, 7006 (2014).
- [71] J. Roncali and I. Grosu, *Advanced Science* **6**, 1801026 (2019).
- [72] C. J. Brabec, S. Gowrisanker, J. J. Halls, D. Laird, S. Jia, and S. P. Williams, *Advanced Materials* **22**, 3839 (2010).
- [73] N. Li, J. D. Perea, T. Kassar, M. Richter, T. Heumueller, G. J. Matt, Y. Hou, N. S. Güldal, H. Chen, S. Chen, et al., *Nature communications* **8**, 1 (2017).

- [74] P. Cheng and X. Zhan, *Chemical Society Reviews* **45**, 2544 (2016).
- [75] C. Li, X. Wu, X. Sui, H. Wu, C. Wang, G. Feng, Y. Wu, F. Liu, X. Liu, Z. Tang, et al., *Angewandte Chemie* **131**, 15678 (2019).
- [76] G. Feng, J. Li, Y. He, W. Zheng, J. Wang, C. Li, Z. Tang, A. Osvet, N. Li, C. J. Brabec, et al., *Joule* **3**, 1765 (2019).
- [77] J. H. Lee, C. G. Park, A. Kim, H. J. Kim, Y. Kim, S. Park, M. J. Cho, and D. H. Choi, *ACS applied materials & interfaces* **10**, 18974 (2018).
- [78] C. G. Park, S. H. Park, Y. Kim, T. L. Nguyen, H. Y. Woo, H. Kang, H. J. Yoon, S. Park, M. J. Cho, and D. H. Choi, *Journal of Materials Chemistry A* **7**, 21280 (2019).
- [79] J. Roncali, *Advanced Energy Materials* **1**, 147 (2011).
- [80] S. Lucas, T. Leydecker, P. Samorì, E. Mena-Osteritz, and P. Bäuerle, *Chemical Communications* **55**, 14202 (2019).
- [81] A. Labrunie, J. Gorenflot, M. Babics, O. Aleveque, S. Dabos-Seignon, A. H. Balawi, Z. Kan, M. Wohlfahrt, E. Levillain, P. Hudhomme, et al., *Chemistry of Materials* **30**, 3474 (2018).
- [82] F. Pierini, M. Lanzi, P. Nakielski, S. Pawłowska, O. Urbanek, K. Zembrzycki, and T. A. Kowalewski, *Macromolecules* **50**, 4972 (2017).
- [83] S. Izawa, K. Hashimoto, and K. Tajima, *Physical Chemistry Chemical Physics* **14**, 16138 (2012).
- [84] T. Nishizawa, H. K. Lim, K. Tajima, and K. Hashimoto, *Chemical communications* pp. 2469–2471 (2009).
- [85] T. L. Nguyen, T. H. Lee, B. Gautam, S. Y. Park, K. Gundogdu, J. Y. Kim, and H. Y. Woo, *Advanced Functional Materials* **27**, 1702474 (2017).
- [86] M. Marinelli, M. Lanzi, A. Liscio, A. Zanelli, M. Zangoli, F. Di Maria, and E. Salatelli, *J. Mater. Chem. C* **8**, 4124 (2020), URL <http://dx.doi.org/10.1039/D0TC00541J>.
- [87] K. Narayanaswamy, A. Venkateswararao, P. Nagarjuna, S. Bishnoi, V. Gupta, S. Chand, and S. P. Singh, *Angewandte Chemie International Edition* **55**, 12334 (2016).
- [88] W. Wang, R. Sun, J. Guo, J. Guo, and J. Min, *Angewandte Chemie* **131**, 14698 (2019).
- [89] D. Andrienko, *Supramolecular Materials for Opto-Electronics* p. 309 (2014).
- [90] D. Andrienko, *Handbook of Materials Modeling: Methods: Theory and Modeling* pp. 1431–1442 (2020).
- [91] P. Kordt, J. J. van der Holst, M. Al Helwi, W. Kowalsky, F. May, A. Badinski, C. Lennartz, and D. Andrienko, *Advanced Functional Materials* **25**, 1955 (2015).
- [92] R. M. Martin, *Electronic structure: basic theory and practical methods* (Cambridge university press, 2020).
- [93] J. J. Intemann, K. Yao, H.-L. Yip, Y.-X. Xu, Y.-X. Li, P.-W. Liang, F.-Z. Ding, X. Li, and A. K.-Y. Jen, *Chemistry of Materials* **25**, 3188 (2013).
- [94] A. Katsouras, N. Gasparini, C. Koulogiannis, M. Spanos, T. Ameri, C. J. Brabec, C. L. Chochos, and A. Avgeropoulos, *Macromolecular rapid communications* **36**, 1778 (2015).
- [95] E. Engel and R. M. Dreizler, *Density functional theory* (Springer, 2013).
- [96] M. C. Zerner, *Reviews in computational chemistry* **2**, 313 (1991).
- [97] C. J. Cramer, *Essentials of computational chemistry: theories and models* (John Wiley & Sons, 2013).
- [98] M. Born and R. Oppenheimer, *Annalen der Physik* **389**, 457 (1927).

- [99] J. Slater, *Physical Review* **91**, 528 (1953).
- [100] D. L. Strout and G. E. Scuseria, *The Journal of chemical physics* **102**, 8448 (1995).
- [101] J. A. Pople, D. P. Santry, and G. A. Segal, *The Journal of Chemical Physics* **43**, S129 (1965).
- [102] J. Pople, D. Beveridge, and P. Dobosh, *The Journal of Chemical Physics* **47**, 2026 (1967).
- [103] K. Burke, *The Journal of chemical physics* **136**, 150901 (2012).
- [104] C. Matta and R. Gillespie, *Journal of Chemical Education* **79**, 1141 (2002).
- [105] W. Kohn and L. J. Sham, *Physical review* **140**, A1133 (1965).
- [106] H. Sun and J. Autschbach, *ChemPhysChem* **14**, 2450 (2013).
- [107] A. D. Becke, *The Journal of chemical physics* **140**, 18A301 (2014).
- [108] J. P. Perdew and K. Schmidt, in *AIP Conference Proceedings* (American Institute of Physics, 2001), vol. 577, pp. 1–20.
- [109] D. C. Langreth and M. Mehl, *Physical Review B* **28**, 1809 (1983).
- [110] J. P. Perdew and W. Yue, *Physical review B* **33**, 8800 (1986).
- [111] C. Lee, W. Yang, and R. G. Parr, *Physical review B* **37**, 785 (1988).
- [112] A. Becke, *J Chem Phys* **98**, 648 (1993).
- [113] S. Hammes-Schiffer, *Science* **355**, 28 (2017).
- [114] E. Runge and E. K. Gross, *Physical Review Letters* **52**, 997 (1984).
- [115] M. E. Casida, in *Recent Advances In Density Functional Methods: (Part I)* (World Scientific, 1995), pp. 155–192.
- [116] A. Becke, *J Chem Phys* **98**, 648 (1993).
- [117] S. Grimme, *Wiley Interdisciplinary Reviews: Computational Molecular Science* **1**, 211 (2011).
- [118] S. Grimme, R. Huenerbein, and S. Ehrlich, *ChemPhysChem* **12**, 1258 (2011).
- [119] J. Moellmann and S. Grimme, *The Journal of Physical Chemistry C* **118**, 7615 (2014).
- [120] S. Grimme, J. Antony, S. Ehrlich, and H. Krieg, *The Journal of chemical physics* **132**, 154104 (2010).
- [121] J. P. Perdew and A. Zunger, *Physical Review B* **23**, 5048 (1981).
- [122] T. Stein, L. Kronik, and R. Baer, *The Journal of chemical physics* **131**, 244119 (2009).
- [123] L. Gallandi, N. Marom, P. Rinke, and T. Körzdörfer, *Journal of chemical theory and computation* **12**, 605 (2016).
- [124] R. Olivares-Amaya, C. Amador-Bedolla, J. Hachmann, S. Atahan-Evrenk, R. S. Sánchez-Carrera, L. Vogt, and A. Aspuru-Guzik, *Energy Environ. Sci.* **4**, 4849 (2011).
- [125] C. Reese, M. Roberts, M.-m. Ling, and Z. Bao, *Materials today* **7**, 20 (2004).
- [126] G. Horowitz, *Journal of materials research* **19**, 1946 (2004).
- [127] D. A. Bardwell, C. S. Adjiman, Y. A. Arnautova, E. Bartashevich, S. X. Boerrigter, D. E. Braun, A. J. Cruz-Cabeza, G. M. Day, R. G. Della Valle, G. R. Desiraju, et al., *Acta Crystallographica Section B: Structural Science* **67**, 535 (2011).
- [128] A. M. Reilly, R. I. Cooper, C. S. Adjiman, S. Bhattacharya, A. D. Boese, J. G. Brandenburg, P. J. Bygrave, R. Bylisma, J. E. Campbell, R. Car, et al., *Acta Crystallographica Section B: Structural Science, Crystal Engineering and Materials* **72**, 439 (2016).

- [129] A. R. Oganov, C. J. Pickard, Q. Zhu, and R. J. Needs, *Nature Reviews Materials* **4**, 331 (2019).
- [130] A. J. Cruz-Cabeza, *Acta Crystallographica Section B: Structural Science, Crystal Engineering and Materials* **72**, 437 (2016).
- [131] A. J. Cruz-Cabeza, N. Feeder, and R. J. Davey, *Communications Chemistry* **3**, 1 (2020).
- [132] T. Wang, G. Kupgan, and J.-L. Brédas, *Trends in Chemistry* (2020).
- [133] S. L. Mayo, B. D. Olafson, and W. A. Goddard, *Journal of Physical Chemistry* **94**, 8897 (1990).
- [134] K. Vanommeslaeghe, E. Hatcher, C. Acharya, S. Kundu, S. Zhong, J. Shim, E. Darian, O. Guvench, P. Lopes, I. Vorobyov, et al., *Journal of computational chemistry* **31**, 671 (2010).
- [135] W. Yu, X. He, K. Vanommeslaeghe, and A. D. MacKerell Jr, *Journal of computational chemistry* **33**, 2451 (2012).
- [136] R. Dovesi, V. Saunders, C. Roetti, R. Orlando, C. Zicovich-Wilson, F. Pascale, B. Civalleri, K. Doll, N. Harrison, I. Bush, et al. (2017).
- [137] J. R. Norris, *Markov chains*, 2 (Cambridge university press, 1998).
- [138] N. Metropolis and S. Ulam, *Journal of the American statistical association* **44**, 335 (1949).
- [139] E. Aarts and J. Korst (1988).
- [140] A. D. Mighell, V. L. Himes, and J. Rodgers, *Acta Crystallographica Section A: Foundations of Crystallography* **39**, 737 (1983).
- [141] J. Donohue, *Acta Crystallographica Section A: Foundations of Crystallography* **41**, 203 (1985).
- [142] V. Coropceanu, J. Cornil, D. A. da Silva Filho, Y. Olivier, R. Silbey, and J.-L. Brédas, *Chemical reviews* **107**, 926 (2007).
- [143] H. Li, L. Duan, D. Zhang, and Y. Qiu, *The Journal of Physical Chemistry C* **118**, 9990 (2014).
- [144] P. Murgatroyd, *Journal of Physics D: Applied Physics* **3**, 151 (1970).
- [145] M. Lax, *The Journal of chemical physics* **20**, 1752 (1952).
- [146] B. Baumeier, J. Kirkpatrick, and D. Andrienko, *Physical Chemistry Chemical Physics* **12**, 11103 (2010).
- [147] A. F. Voter, in *Radiation effects in solids* (Springer, 2007), pp. 1–23.
- [148] S.-H. Liao, H.-J. Jhuo, P.-N. Yeh, Y.-S. Cheng, Y.-L. Li, Y.-H. Lee, S. Sharma, and S.-A. Chen, *Scientific reports* **4**, 6813 (2014).
- [149] Y. Liu, J. Zhao, Z. Li, C. Mu, W. Ma, H. Hu, K. Jiang, H. Lin, H. Ade, and H. Yan, *Nature communications* **5**, 1 (2014).
- [150] D. Qian, L. Ye, M. Zhang, Y. Liang, L. Li, Y. Huang, X. Guo, S. Zhang, Z. Tan, and J. Hou, *Macromolecules* **45**, 9611 (2012).
- [151] R. Po, G. Bianchi, C. Carbonera, and A. Pellegrino, *Macromolecules* **48**, 453 (2015).
- [152] B. Walker, C. Kim, and T.-Q. Nguyen, *Chemistry of Materials* **23**, 470 (2011).
- [153] M. T. Lloyd, J. E. Anthony, and G. G. Malliaras, *Materials Today* **10**, 34 (2007), ISSN 1369-7021.
- [154] S. Roquet, A. Cravino, P. Leriche, O. Alévâque, P. Frère, and J. Roncali, *Journal of the American Chemical Society* **128**, 3459 (2006).
- [155] C. Cabanetos, P. Blanchard, and J. Roncali, *The Chemical Record* **19**, 1123 (2019).
- [156] Y. Jiang, C. Cabanetos, M. Allain, P. Liu, and J. Roncali, *Journal of Materials Chemistry C* **3**, 5145 (2015).

- [157] Y. Jiang, M. Allain, D. Gindre, S. Dabos-Seignon, P. Blanchard, C. Cabanetos, and J. Roncali, *Scientific reports* **7**, 1 (2017).
- [158] Y. Jiang, D. Gindre, M. Allain, P. Liu, C. Cabanetos, and J. Roncali, *Advanced Materials* **27**, 4285 (2015).
- [159] J. Rivnay, S. C. Mannsfeld, C. E. Miller, A. Salleo, and M. F. Toney, *Chemical reviews* **112**, 5488 (2012).
- [160] T. Wang, G. Kupgan, and J.-L. Brédas, *Trends in Chemistry* **2**, 535 (2020), ISSN 2589-5974.
- [161] A. A. Virkar, S. Mannsfeld, Z. Bao, and N. Stingelin, *Advanced Materials* **22**, 3857 (2010).
- [162] D. Alberga, I. Ciofini, G. F. Mangiatordi, A. Pedone, G. Lattanzi, J. Roncali, and C. Adamo, *Chemistry of Materials* **29**, 673 (2017).
- [163] M. Frisch, G. Trucks, H. Schlegel, G. Scuseria, M. Robb, J. Cheeseman, G. Scalmani, V. Barone, G. Petersson, H. Nakatsuji, et al., *Gaussian 16* (2016).
- [164] C. I. Bayly, P. Cieplak, W. Cornell, and P. A. Kollman, *The Journal of Physical Chemistry* **97**, 10269 (1993).
- [165] D. Presti, L. Wilbraham, C. Targa, F. Labat, A. Pedone, M. C. Menziani, I. Ciofini, and C. Adamo, *The Journal of Physical Chemistry C* **121**, 5747 (2017).
- [166] E. Madelung, *Phys. Z* **19**, 32 (1918).
- [167] M. Cutini, B. Civalieri, M. Corno, R. Orlando, J. G. Brandenburg, L. Maschio, and P. Ugliengo, *Journal of chemical theory and computation* **12**, 3340 (2016).
- [168] K. Hongo, M. A. Watson, R. S. Sanchez-Carrera, T. litaka, and A. Aspuru-Guzik, *The Journal of Physical Chemistry Letters* **1**, 1789 (2010).
- [169] S. E. Fritz, S. M. Martin, C. D. Frisbie, M. D. Ward, and M. F. Toney, *Journal of the American Chemical Society* **126**, 4084 (2004).
- [170] C. J. Takacs, Y. Sun, G. C. Welch, L. A. Perez, X. Liu, W. Wen, G. C. Bazan, and A. J. Heeger, *Journal of the American Chemical Society* **134**, 16597 (2012).
- [171] F. Würthner, *Accounts of Chemical Research* **49**, 868 (2016).
- [172] G. Heimel, I. Salzmann, S. Duhm, and N. Koch, *Chemistry of Materials* **23**, 359 (2011).
- [173] J.-L. Brédas, X. Chen, T. Körzdörfer, H. Li, C. Risko, S. M. Ryno, and T. Wang, *Conjugated Polymers: Perspective, Theory, and New Materials* p. 37 (2019).
- [174] M. Cossi, V. Barone, R. Cammi, and J. Tomasi, *Chemical Physics Letters* **255**, 327 (1996).
- [175] T. Le Bahers, C. Adamo, and I. Ciofini, *Journal of chemical theory and computation* **7**, 2498 (2011).
- [176] J. Hoja, H.-Y. Ko, M. A. Neumann, R. Car, R. A. DiStasio, and A. Tkatchenko, *Science advances* **5**, eaau3338 (2019).
- [177] D. Jacquemin, V. Wathelet, E. A. Perpète, and C. Adamo, *Journal of Chemical Theory and Computation* **5**, 2420 (2009).
- [178] B. Kippelen and J.-L. Brédas, *Energy & Environmental Science* **2**, 251 (2009).
- [179] P. Peumans, A. Yakimov, and S. R. Forrest, *Journal of Applied Physics* **93**, 3693 (2003).
- [180] M. Hiramoto, H. Fujiwara, and M. Yokoyama, *Journal of applied physics* **72**, 3781 (1992).
- [181] J. Halls, C. Walsh, N. C. Greenham, E. Marseglia, R. H. Friend, S. Moratti, and A. Holmes, *Nature* **376**, 498 (1995).
- [182] F. C. Krebs, *Stability and degradation of organic and polymer solar cells* (John Wiley & Sons, 2012).

- [183] A. P. Diac, L. Szolga, C. Cabanetos, A. Bogdan, A. Terec, I. Grosu, and J. Roncali, *Dyes and Pigments* **171**, 107748 (2019).
- [184] S. Lucas, J. Kammerer, M. Pfannmöller, R. R. Schröder, Y. He, N. Li, C. J. Brabec, T. Leydecker, P. Samorì, T. Marszalek, et al., *Solar RRL* (2020).
- [185] V. Coropceanu, X.-K. Chen, T. Wang, Z. Zheng, and J.-L. Brédas, *Nature Reviews Materials* pp. 1–19 (2019).
- [186] J. Roncali, *Chemical Society Reviews* **34**, 483 (2005).
- [187] K. Narayanaswamy, A. Venkateswararao, V. Gupta, S. Chand, and S. P. Singh, *Chemical Communications* **52**, 210 (2016).
- [188] I. Meager, R. S. Ashraf, S. Mollinger, B. C. Schroeder, H. Bronstein, D. Beatrup, M. S. Vezie, T. Kirchartz, A. Salleo, J. Nelson, et al., *Journal of the American Chemical Society* **135**, 11537 (2013).
- [189] M. Tantiwivat, A. Tamayo, N. Luu, X.-D. Dang, and T.-Q. Nguyen, *The Journal of Physical Chemistry C* **112**, 17402 (2008).
- [190] S. Qu and H. Tian, *Chemical Communications* **48**, 3039 (2012).
- [191] J. Cornil, J.-L. Brédas, J. Zaumseil, and H. Sirringhaus, *Advanced Materials* **19**, 1791 (2007).
- [192] M. Frisch, G. Trucks, H. Schlegel, G. Scuseria, M. Robb, J. Cheeseman, G. Scalmani, V. Barone, B. Men-  
nucci, and G. Petersson (2009).
- [193] BIOVIA, *Materials studio* (2020), v. 2018, San Diego, Dassault Systèmes.
- [194] J. C. Phillips, R. Braun, W. Wang, J. Gumbart, E. Tajkhorshid, E. Villa, C. Chipot, R. D. Skeel, L. Kale, and  
K. Schulten, *Journal of computational chemistry* **26**, 1781 (2005).
- [195] R. A. Marcus, *Reviews of Modern Physics* **65**, 599 (1993).
- [196] J.-L. Brédas, J. P. Calbert, D. da Silva Filho, and J. Cornil, *Proceedings of the National Academy of  
Sciences* **99**, 5804 (2002).
- [197] S. F. Nelsen, S. C. Blackstock, and Y. Kim, *Journal of the American Chemical Society* **109**, 677 (1987).
- [198] V. Stehr, R. Fink, M. Tafipolski, C. Deibel, and B. Engels, *Wiley Interdisciplinary Reviews: Computational  
Molecular Science* **6**, 694 (2016).
- [199] J. Kirkpatrick, *International Journal of Quantum Chemistry* **108**, 51 (2008).
- [200] G. J. Beran, *Chemical reviews* **116**, 5567 (2016).
- [201] J. G. Brandenburg and S. Grimme, *Acta Crystallographica Section B: Structural Science, Crystal Engi-  
neering and Materials* **72**, 502 (2016).
- [202] S. L. Price and J. G. Brandenburg, in *Non-covalent Interactions in Quantum Chemistry and Physics:  
Theory and Applications*, edited by A. O. de la Roza and G. A. DiLabio (Elsevier, 2017), pp. 333–336.
- [203] R. L. Akkermans, N. A. Spensley, and S. H. Robertson, *Molecular Simulation* **39**, 1153 (2013).
- [204] F. Günther, S. Gemming, and G. Seifert, *The Journal of Physical Chemistry C* **120**, 9581 (2016).
- [205] M. V. Makarova, S. G. Semenov, and O. A. Guskova, *International Journal of Quantum Chemistry* **116**,  
1459 (2016).
- [206] F. Gajdos, H. Oberhofer, M. Dupuis, and J. Blumberger, *The journal of physical chemistry letters* **4**, 1012  
(2013).

- [207] M. Baldo, Z. Soos, and S. Forrest, *Chemical physics letters* **347**, 297 (2001).
- [208] A. R. Oganov, O. Isayev, A. Shapeev, P. Sushko, C. Gatti, A. Walsh, R. Akashi, X.-Q. Chen, R. Ramprasad, V. Stevanovich, et al., *Computational materials discovery* (Royal Society of Chemistry, 2018).
- [209] A. Pulido, L. Chen, T. Kaczorowski, D. Holden, M. A. Little, S. Y. Chong, B. J. Slater, D. P. McMahon, B. Bonillo, C. J. Stackhouse, et al., *Nature* **543**, 657 (2017).
- [210] R. Olivares-Amaya, C. Amador-Bedolla, J. Hachmann, S. Atahan-Evrenk, R. S. Sanchez-Carrera, L. Vogt, and A. Aspuru-Guzik, *Energy & Environmental Science* **4**, 4849 (2011).
- [211] B. A. Nogueira, C. Castiglioni, and R. Fausto, *Communications Chemistry* **3**, 1 (2020).
- [212] R. Po, A. Bernardi, A. Calabrese, C. Carbonera, G. Corso, and A. Pellegrino, *Energy & Environmental Science* **7**, 925 (2014).
- [213] M. C. Scharber, D. Mühlbacher, M. Koppe, P. Denk, C. Waldauf, A. J. Heeger, and C. J. Brabec, *Advanced materials* **18**, 789 (2006).



## RÉSUMÉ

---

Il y a plusieurs façons de présenter le sujet du photovoltaïque organique. La plus courante est de le présenter dans le contexte de la crise énergétique actuelle et de le proposer comme une des solutions parmi les plus prometteuses pour fournir des sources d'énergie alternatives propres et bonne marché pour faciliter la transition écologique

Dans un même temps, la recherche sur les matériaux semi-conducteurs organiques pourrait bien être inscrit dans un plus large effort scientifique qui vise à accroître nos connaissances et à affiner notre maîtrise des matériaux encore faiblement exploités.

Dans ce contexte, le développement des méthodes théoriques fiables pour l'étude de la structure électronique des matériaux, permet aujourd'hui la description et la prédiction de plus en plus précise des propriétés moléculaires à petit échelle qui jouent un rôle très important sur les propriétés macroscopiques des matériaux organiques, d'intérêt pour pouvoir les améliorer et les exploiter.

La recherche au sujet des matériaux performants est alors en train de basculer vers un paradigme qui voit la possibilité concrète d'intervenir sur la structure des molécules de synthèse pour obtenir des matériaux innovants dont la fonction a été choisie en avance. Cet objectif est possible grâce à l'information microscopique que les données théoriques et les nouvelles techniques expérimentales d'investigation, sont à l'heure actuelle, en mesure de fournir.

Toutefois, un obstacle très important surgit, qui touche en particulière les matériaux organiques: l'ampleur de l'espace chimique que ces molécules occupent est tel que des stratégies pour l'explorer efficacement deviennent absolument nécessaires.

La capacité de surmonter cet obstacle pourrait se traduire, dans l'avenir, dans la possibilité de rendre nos applications technologiques adaptées aux conditions et environnements les plus variés. D'innombrables domaines technologiques, de l'électronique à la médecine, pourraient bénéficier de ce niveau de contrôle.

Dans le cas spécifique du photovoltaïque organique, la promesse est de délivrer des matériaux capables d'absorber la lumière dans des conditions et sur des surfaces assez différentes et de pouvoir la transformer en électricité avec haut rendement.

Pour accomplir cela, il est essentiel de déployer des protocoles numériques qui combinent des techniques connues pour simuler et prédire le plus précisément possible le comportement d'un matériau aux échelles les plus influentes. Ce travail de thèse se situe dans ce contexte. Un protocole spécifique a été conçu pour l'étude des matériaux photovoltaïques à l'aide de la théorie de la fonctionnelle de la densité, de la dynamique moléculaire et des méthodes Monte-Carlo.

Pour simuler le rendement photovoltaïque d'un matériau plusieurs propriétés sont étudiées, notamment celles concernant l'interaction avec la lumière, comme l'absorption ou le transport de charge. Afin de pouvoir produire des simulations suffisamment proche de la réalité, beaucoup d'efforts sont réalisés pour modéliser l'organisation moléculaire à ces échelles de taille qui peuvent influencer plus lourdement les propriétés macroscopiques.

Ici, deux systèmes sont étudiés. Dans le chapitre trois, un matériau donneur pour lequel il a été observé un comportement en absorption assez particulier et puis, dans le chapitre quatre, un assemblage moléculaire, dit dyade, qui combine une molécule de donneur et une d'accepteur dans une architecture moléculaire adaptée pour la construction des cellules photovoltaïques dites à composant unique.

Ces études nous ont fourni une description microscopique précise, essentielle à la compréhension des mécanismes en jeu et à l'optimisation successive de matériaux photo-actifs. Le protocole de calcul mis au point s'est donc révélé comme un outil très efficace pour aider à l'exploration de cet espace chimique qui recèle de nombreux matériaux aux propriétés inédites et innovantes.

## MOTS CLÉS

---

photovoltaïque organique, chimie théorique, chimie physique, théorie de la fonctionnelle de la densité

## ABSTRACT

---

In much of the literature about organic photovoltaics, the topic is framed within the current landscape of energy production and the research on these materials is cited as a possible solution to the energy crisis looming ahead.

Despite being the most frequent, this is by no means the only perspective that can be offered. Indeed, the same research may also be set within the larger perspective offered by the field of functional materials. These materials are usually exploited for their particular responses to electrical, magnetic and chemical stimuli and are at the basis of many technologies fundamental to our society.

The prominent position of functional materials in modern science is due to the emergence of novel technological needs that such materials have been able to satisfy thanks to their peculiar properties. These properties have been rationalised and mastered by expanding the theoretical description of the underlying physical mechanisms.

This theoretical body, combined with the growth and diffusion of computational capabilities has fostered a change in the scientific paradigm underpinning the research effort. More and more, the predictive power of numerical approaches is exploited to lead the way in the exploration of the immense chemical space. The ultimate promise is to achieve the purpose-driven design of compounds thanks to which the molecular structure can be engineered before the actual synthesis to meet the demands dictated by a specific application.

To fulfil this role, computational approaches need to be able to simulate the solid state properties at the most relevant time and length scales. If this can be accomplished then a reliable prediction of the performance can be achieved.

The current work deals with the development and application of one such protocol, for the particular case of organic photovoltaic semi-conductors. Given the specific application, the properties targeted are light absorption and charge transport. Particular effort is put in the simulation of local morphologies at scales above the molecular one to describe supramolecular organisation with sufficient resolution.

In this thesis, the protocol is applied to two molecular systems employed in solar devices. Both systems have been selected on the basis of data suggesting that a detailed microscopic description of their behaviour could be highly informative about the aspects responsible for their photovoltaic performance. In particular, chapter 3 details the investigation of a small-molecule donor that has been shown in the literature to have a remarkable behaviour in absorption. While chapter 4 reports the study of a donor-acceptor dyad used as active layer in single-component solar devices with relatively high conversion efficiency.

In both cases, the computational protocol has proven capable of providing a detailed microscopic description of the systems. The picture drawn has allowed to clarify the plausible mechanisms behind the observations and to rationalise these behaviours in a broader and more general theoretical framework.

## KEYWORDS

---

theoretical chemistry, density functional theory, molecular dynamics, physical chemistry, organic photovoltaics, organic solar cells